Magneto Cosmic-Ray Instability in Weakly Magnetized Galactic Disk

January 2017

Chiba University

Graduate School of Science

Division of Fundamental Science

Department of Physics

Yuki Kudoh

（千葉大学審査学位論文）

Magneto Cosmic-Ray Instability in Weakly Magnetized Galactic Disk

January 2017

Chiba University

Graduate School of Science

Division of Fundamental Science

Department of Physics

Yuki Kudoh

Abstract

In galactic gas disks, magnetic fields play essential roles in the angular momentum transport, generation of turbulence and formation of hot halos with outflows. The all sky distribution of radio continuum emission indicates that magnetic fields emerging from the galactic disk form synchrotron emitting halo. In this thesis, we study the effects of cosmic rays (non-thermal particles) on the growth of the undular mode of the magnetic buoyancy instability in galactic gas disks.

The cosmic rays are treated as the fluid by integrating the distribution function of particles over the momentum space. The derived cosmic ray magnetohydrodynamic (CR MHD) equations are solved by linearizing the equations and by carrying out nonlinear simulations. From linear stability analysis, we confirmed that CR diffusion along magnetic field lines increases the growth rate. We also found that when the ratio of CR pressure $P_{\rm cr}$ to gas pressure $P_{\rm g}$ ($\beta = P_{\rm cr}/P_{\rm g}$) is larger than 0.2, the growth rate increases as the ratio of the magnetic pressure $P_{\rm B}$ to gas pressure ($\alpha = P_{\rm B}/P_{\rm g}$) decreases, and the most unstable wavenumber increases. This "Magneto Cosmic-ray Instability" (MCI) is driven by the CR diffusion along the magnetic field lines, and distinct from the Parker instability without CR diffusion driven by buoyancy created by sliding the gas along the magnetic field lines.

To study the non-linear growth of MCI by numerical simulations, we improved the Roe-type approximate Riemann solver of which the solutions satisfy the Rankine-Hugoniot relation at any shock and can achieve high order accuracy. We solve fully conservation form of CR MHD equation. In this approach, CR energy equation containing a source term is transformed to the conservation equation of CR "number" density $\rho_{\rm cr}$ defineded as $\rho_{\rm cr} \equiv P_{\rm cr}^{1/\gamma_{\rm cr}}$ where $\gamma_{\rm cr}$ is the specific heat ratio of the CR gas. We found by shock tube simulations that numerical solutions solved by using CR non-conservation form does not

converge to the Riemann solution, but the conservation form does.

MCI drives the buoyant escape of magnetic flux from the disk. In weakly magnetized disks, the growth rate of MCI is larger than that of the Parker instability and the most unstable wavelength is shorter. By carrying out CR MHD simulations, we found that the disk gas is uplifted by MCI in weakly magnetized disks and form magnetized corona. The buoyant escape of the magnetic flux from the disk to the disk halo may limit the magnetic flux amplified by the disk dynamo and retained in the disk.

Acknowledgement

I am deeply grateful to Prof. R. Matsumoto and Prof. T. Hanawa who brought me wonderful knowledge and experience for my academic life. I have learned their philosophy of study and the way of what academically valuable papers are and how the presentations of scientific results stimulate a person, and so on.

I would like to thank Prof. S. Yoshida, Prof. T. Terasawa, Prof. H. Nakada, and Prof. Y. Matsumoto for their constructive comments. I could not finalize up this thesis better without their help. I also thank to Prof. T. Kudoh, Prof. M. Machida, Prof T. Yokoyama, Prof. M. Hattori, Dr. H. Hotta, and C.-H. Peng for the lively and useful discussion. I would like to express my thanks to all the student members of the Astrophysical Lab. at Chiba university and to Prof. S. Miyaji.

The numerical computations in this thesis have been carried out on Cray XT4 and XC30 at Center for Computational Astrophysics, National Astronomical Observatory of Japan, and the Fujitsu PRIMEHPC FX10 System (Oakleaf-FX,Oakbridge-FX) in the Information Technology Center, The University of Tokyo and Kyusyu.

Finally, I wish to thank my family and my grandparents for their kind supports and great encouragement.

Contents

Chapter 1

General Introduction

1.1 Observations of Galactic Magnetic Fields

Galactic magnetic fields can be measured by synchrotron radiation emitted by high energy electrons gyrating in magnetic fields or by the influence of magnetic fields on the propagation of electromagnetic waves. The synchrotron radiation enables observers to measure the direction and strength of magnetic field $B_\perp$ perpendicular to the line of sight. Since the direction of acceleration of the relativistic electrons is orthogonal to the magnetic field, the radiation is linearly polarized perpendicular to the magnetic field. We assume that the energy spectrum of relativistic CR electrons have the power law distribution,

$$N(\gamma)d\gamma = N_0\gamma^{-p}d\gamma, \qquad \gamma_1 < \gamma < \gamma_2, \tag{1.1}$$

where, γ, N_0 and p denote the Lorentz factor, density per energy interval, and the spectral index, respectively. We assume N_0 and p are uniform in the emitting region. The synchrotron radiation with frequency ν has the intensity (e.g. Rybicki & Lightman 1985)

$$I_\nu \propto N_0\nu^{(1-p)/2}B_\perp^{(1+p)/2}L, \tag{1.2}$$

where L is the source size. We assume the equipartition between magnetic energy density and the CR energy density $W_{\rm cr}$ defined as,

$$W_{\rm cr} \propto \int_{\gamma_1}^{\gamma_2} \gamma N(\gamma) d\gamma \propto \frac{N_0}{p-2}. \tag{1.3}$$

Hence, by determining the power law index p from the dependence of I_ν on ν, the magnetic field strength $B_\perp$ can be estimated as,

$$B_\perp \propto \left(\frac{I_\nu}{L\,(p-2)}\right)^{2/(p+5)} \nu^{(p-1)/(p+5)}. \tag{1.4}$$

The second method to measure cosmic magnetic fields is Faraday rotation. The linearly polarized radio wave propagating along magnetic field lines rotates polarization plane by the Faraday effect during its propagation through the thermal plasma. The rotation angle $\Delta\phi$ can be written as,

$$\Delta\phi = \mathrm{RM}\left(\frac{c}{\nu}\right)^2 \qquad \mathrm{rad}, \tag{1.5}$$

where c is light speed, and RM is the Rotation Measure defined by,

$$\mathrm{RM} = 8.1\times10^{-5}\int_0^{\rm L} n_e B_\parallel dl \sim 8.1\times10^{-5} n_e B_\parallel L \qquad \mathrm{rad\ cm^{-2}}, \tag{1.6}$$

where n_e and L are the number density of the thermal electron and the line of sight length of the interstellar ionized gas, respectively. Faraday rotation angle depends on the magnetic field direction along the line of sight. The number density n_e needs to be determined by other observation.

Next we overview the all sky survey of magnetic fields of the Milky Way. Fig. 1.1 shows the total intensity (left) and the polarized intensity (right). Galactic equatorial plane is bright in synchrotron radiation. There are notable diffuse filamentary or loop like emissions in high latitude. The diffuse emission indicates that galactic magnetic field and CR electrons emerge from the disk. Synchrotron emission is dominant in frequencies between 300 MHz and 10 GHz (see, e.g. Draine 2011). Lower frequency is limited by the thermal gas absorption, and the upper limit is due to the dominance of the Cosmic

Microwave Background (CMB) radiation.

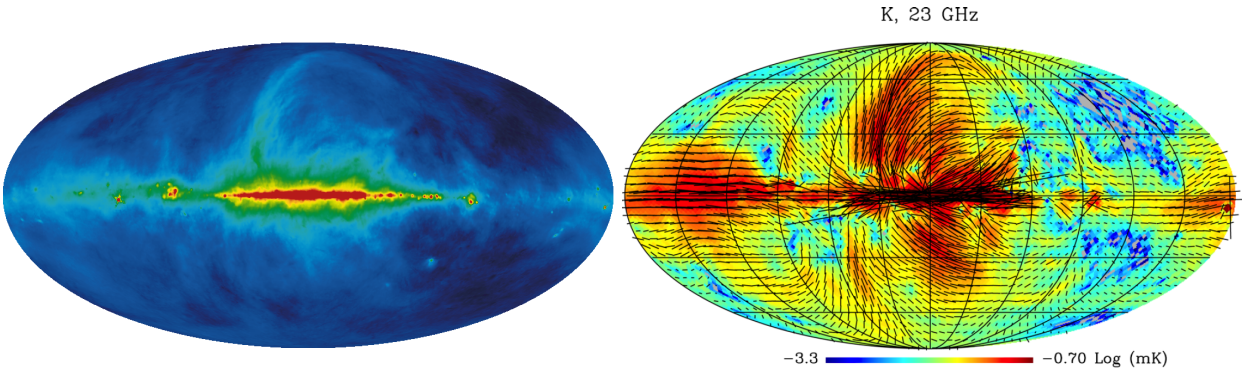

Fig.1.1 All sky surveys of radio continuum emission. Left panel shows the total intensity map reported by Haslam et al. (1982) at 408 MHz reprocessed by Remazeilles et al. (2015). Right panel shows the polarized intensity map by WMAP K-bant 23GHz (Vidal et al. 2015). Black lines show the magnetic field direction and their length is proportional to the polarization intensity.

The spectrum of intensity I_ν is parameterized by the power law photon index q as $I_\nu \propto \nu^{-q}$. The photon index q is related to the index of CR energy spectrum index p as $2q = p - 1$. Observed averaged photon index is $q = 0.95 \pm 0.15$ between 408 MHz and 1.42 GHz for galactic latitude$|b| > 5°$ (La Porta et al. 2008), $q = 0.73$ between 45 and 408 MHz (Guzmán et al. 2011), and $q = 0.86$ between 408 MHz and 2.3 GHz (Giardino et al. 2002; Platania et al. 2003). Vidal et al. (2015) concluded that photon index determined by WMAP polarized intensity at 23 and 33 GHz is $0.84 < q < 1.06$. The WMAP satellite covered the frequency from 23 GHz to 94 GHz. Observation of the synchrotron polarized emission are reported by, e.g. Wolleben et al. (2006); Testori, Reich & Reich (2008); Rudnick & Brown (2009) at 1.4 GHz, and Planck Collaboration (2016) at 30 GHz Let us estimate the galactic magnetic field using the synchrotron intensity in optically thin plasma,

$$I_\nu = a(p)\frac{e^3}{m_e c^2}\left(\frac{3e}{4\pi m_e^3 c^5}\right)^{(p-1)/2} N B_\perp^{(p+1)/2} \nu^{-(p-1)/2} \tag{1.7}$$

where $a(p)$ is the order of unity quantity weakly dependent on the CR spectrum index p (for detail, see e.g. Rybicki & Lightman 1985). By adopting the mean intensity of the sky, $I_\nu \sim 3 \times 10^{-26}$ at ν =140 MHz, CR spectral index $p \sim 3$, and the size of our galaxy

$L \sim 18$ kpc, galactic magnetic field in equation (1.4) can be estimated by

$$B_{\perp,\mathrm{av}} \sim \left(\frac{e^3}{m_e c^2}\right)^{-\frac{2}{p+1}} \left(\frac{3e}{4\pi m_e^3 c^5}\right)^{\frac{1-p}{p+1}} \left(\frac{I_\nu}{L}\right)^{\frac{2}{p+5}} \nu^{(p-1)/(p+5)} \sim 0.8 \ \ \mu\mathrm{G}. \tag{1.8}$$

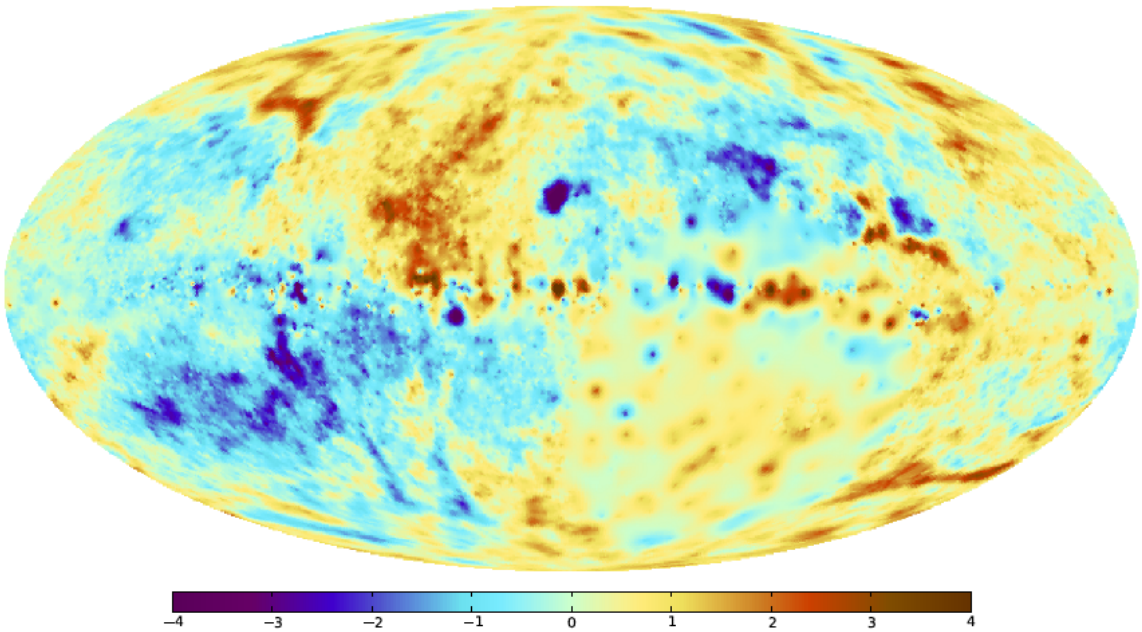

Fig.1.2 All-sky map of rotation measures (Oppermann et al. 2012). Red denotes the positive RM corresponding to the magnetic filed toward the observer, and blue denotes the magnetic field in opposite direction.

Line of sight galactic halo magnetic field $B_{\|}$ can be estimated by RM using the extra galactic radio sources. Oppermann et al. (2012) improved the all sky map of RM by Taylor, Stil & Sunstrum (2009) by statistically analyzing angular power spectrum reconstructed from the largest catalog of extra galactic sources. All sky distribution of RM are shown in Fig. 1.2. In the galactic plane, bright spots are mainly point sources. The sign of the RM is opposite above and below the galactic equatorial plane, indicating bipolar structure illustrated in the left panel of Fig. 1.3. However, RM has the same sign in the outer region. In other words, magnetic field around the solar neighbourhood has the quadrupole feature illustrated in the right panel of 1.3. Number of sources in RM catalog published earlier work is e.g. several sources in Simard-Normandin & Kronberg (1980), 37,543 sources in Taylor, Stil & Sunstrum (2009). The proposed Square Kilometre Array (SKA) designed as multi radio telescope located in one square kilometer is expected to measure 100 low luminosity sources of polarized radiation per square degree per hour (Rudnick & Owen

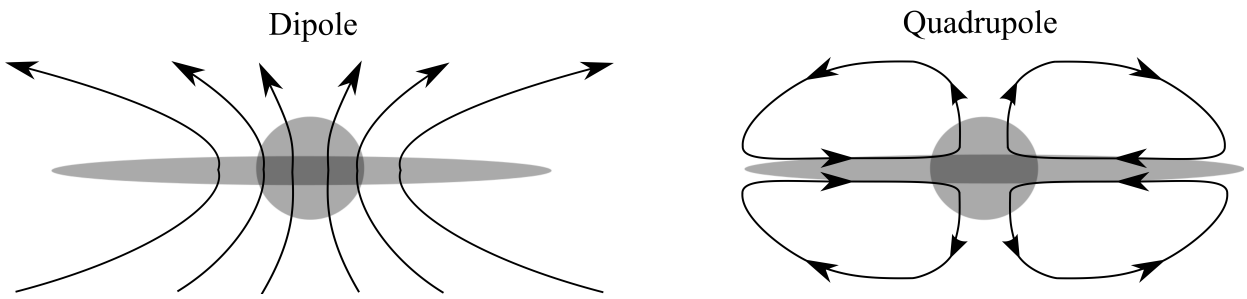

Fig.1.3 Illustration of symmetries in Halo fields.

2014).

1.2 Galactic dynamo

Galactic diffuse magnetic fields are produced by the emergence of magnetic fields from the galactic disk. The galactic magnetic fields are thought to be amplified and maintained by the galactic dynamo. For activating the disk dynamo, we assume weak ($< 10^{-3}\mu$G) seed field.

The seed field can be amplified by the differential rotation. However, it is well known as Cowling's anti dynamo theorem (Cowling 1934) that axisymmetric magnetic fields cannot be maintained. We need some processes to generate non-axisymmetric perturbation and the feedback from azimuthal field to the radial field. In the $\alpha - \Omega$ dynamo theory, the feedback from the toroidal field to the poloidal field is parameterized by the dynamo parameter α. In this theory, the induction equation is solved by assuming the velocity field (e.g. rotation and turbulence). This kinematic approach should be consistentwith the dynamics of the magnetized fluid. Balbus & Hawley (1991) pointed out the importance of the Magneto-Rotational Instability (MRI) in differentially rotating magnetized disks. They showed that the angular momentum transport by perturbed magnetic fields drives magnetohydrodynamic instability through which azimuthal magnetic fields and radial magnetic fields are amplified. This instability grows in the disk rotation time scale.

Nishikori, Machida & Matsumoto (2006) and Machida et al. (2013) carried out three-dimensional simulation assuming galactic gravitational potential and studied the time evolution of disk magnetic fields, and proposed the MRI-Parker dynamo model. Fig. 1.4 (a) shows the generation of radial field by MRI. This mechanism corresponds to the α

effect. Additionally, the radial field produces the azimuthal field by differential rotation (Ω effect). The radial field produces the toroidal field, which escapes from disk to halo due to the Parker instability. When the azimuthal field is amplified, the global three-dimensional MHD simulations revealed that mean toroidal magnetic field reverses quasi-periodically. Machida et al. (2013) included the disk above and below the equatorial plane into the simulation region and showed that the disk magnetic fields show transitions between the dipole and the quadrupole field (see, Fig. 1.3).

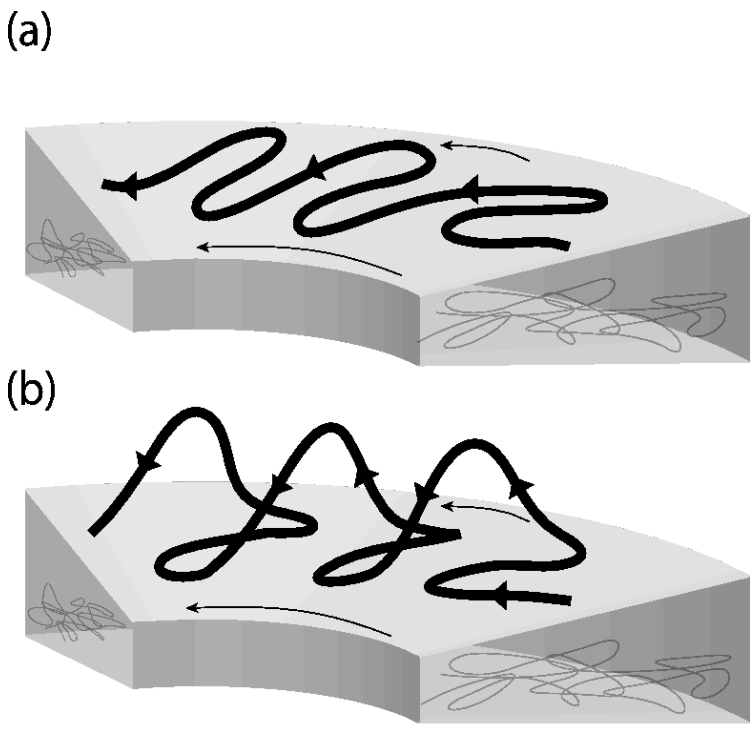

Fig.1.4 Illustration of the disk dynamo driven by the Magneto-Rotational Instability (MRI).

Another possible driving mechanism of the disk dynamo is the SuperNova (SN) explosion. The SN model has uncertainties on what kind of energy is injected (e.g. kinetic energy: Gissinger, Fromang & Dormy 2009; Gressel, Elstner & Ziegler 2013, thermal with magnetic: Butsky et al. 2016, cosmic ray: Hanasz, Wóltański & Kowalik 2009). In order to maintain the disk field, the energy of the single SN is not sufficient. Highly efficient injection of CR particles is necessary to drive dynamo by SN explosions.

1.3 Parker instability

Parker (1966, 1967) pointed out the mechanism of the formation of dense interstellar

cloud by undular mode of magnetic buoyancy instability (referred to as Parker instability). Parker instability, shown in Fig. 1.5, is driven by undular perturbation of galactic magnetic field. As the gas slides down, the density at the loop top decreases. When the buoyancy exceeds the restoring magnetic tension, the magnetic field escapes buoyantly from the galactic disk.

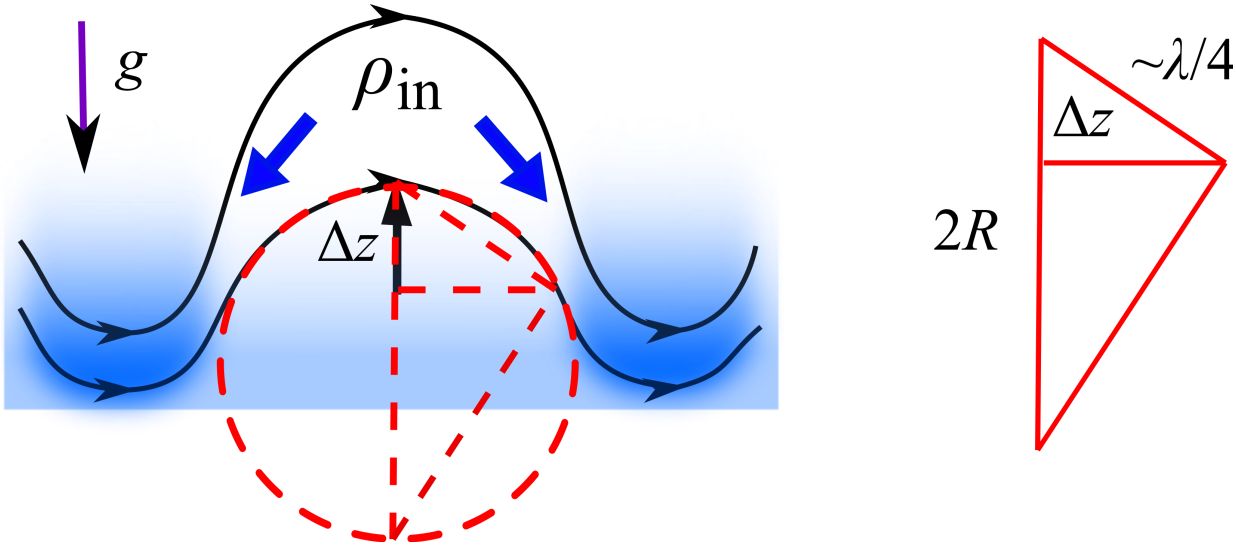

Fig.1.5 A schematic diagram of the Parker instability.

Here we estimate the unstable condition of Parker instability. For simplicity, we neglect CRs in this section. First, we assume plane parallel stratified atmosphere in magneto hydrostatic equilibrium under vertical gravity g and horizontal magnetic field,

$$\frac{d}{dz}\left(P_{\rm g}+\frac{B^2}{2}\right)=-\rho g, \tag{1.9}$$

where P_g, B, ρ are gas pressure, magnetic field parallel to galactic equatorial plane, and density, respectively. We assume that g is constant, and the ratio of magnetic pressure to gas pressure,

$$\alpha=\frac{|\boldsymbol{B}|^2/2}{P_{\rm g}}, \tag{1.10}$$

is spatially constant. By assuming isothermal gas, we obtain the equilibrium density

profile,

$$\rho(z) = \rho_{\rm eq} \exp\left(-\frac{z}{H_B}\right), \quad H_B \equiv \frac{(1+\alpha)a^2}{\gamma_{\rm g} g} = (1+\alpha)H_{\rm g}, \tag{1.11}$$

where $\rho_{\rm eq}$ denotes the density at the equatorial plane $z = 0$, $\gamma_{\rm g}$ is the specific gas heat ratio, a is sound speed defined as $a^2 = \gamma_{\rm g} P_{\rm g}/\rho$, $H_{\rm g}$ is the scale height for no magnetic field. When undular perturbation Δz is imposed the density inside the undulating magnetic field $\rho_{\rm in}$ can be approximated by the density distribution with no magnetic field as,

$$\rho_{\rm in}(z+\Delta z) \sim \rho_{\rm eq} \exp\left(-\frac{z+\Delta z}{H_{\rm g}}\right). \tag{1.12}$$

The buoyancy force $F_{\rm buoyancy}$ is proportional to the density difference between that in the perturbed fluid element and unperturbed fluid element,

$$F_{\rm buoyancy} = -\Big(\rho_{\rm in}(z+\Delta z) - \rho(z+\Delta z)\Big) g \tag{1.13}$$

$$\sim -\left(\frac{\Delta z}{H_B} - \frac{\Delta z}{H_{\rm g}}\right)\rho(z) g = \alpha \frac{\Delta z}{H_B}\rho(z) g. \tag{1.14}$$

Here, we used the first order Taylor series approximation assuming $\Delta z \ll z$.

The restoring force is the magnetic tension force $F_{\rm tension}$,

$$F_{\rm tension} = \frac{B^2}{R} \sim \frac{32}{\lambda^2} B^2 \Delta z \tag{1.15}$$

Here R is the curvature radius, which can be estimated by using the circle in Fig. 1.5. By using the wavelength λ and the similarity of triangle, we obtain $2R : \lambda/4 = \lambda/4 : \Delta z$.

By using equations (1.14) and (1.15), the unstable condition of Parker instability $F_{\rm buoyancy} > F_{\rm tension}$ gives the critical wavelength $\lambda_{\rm crit}$ for Parker instability,

$$\lambda > \lambda_{\rm crit} \equiv 8 H_{\rm g} \sqrt{1+\alpha}. \tag{1.16}$$

In the galactic disks, the typical critical wave length is $\lambda_{\rm crit} \sim 570$ pc for $\alpha = 1$ when scale hight $H_{\rm g} = 100$ pc. Parker (1979) showed that the typical timescale of the instability is

the order of Alfvén crossing time $\tau_A \sim H_g/v_A \sim 10^7$ yr for $a = 10$ km/s and $H_g = 100$ pc, where v_A is the Alfvén speed.

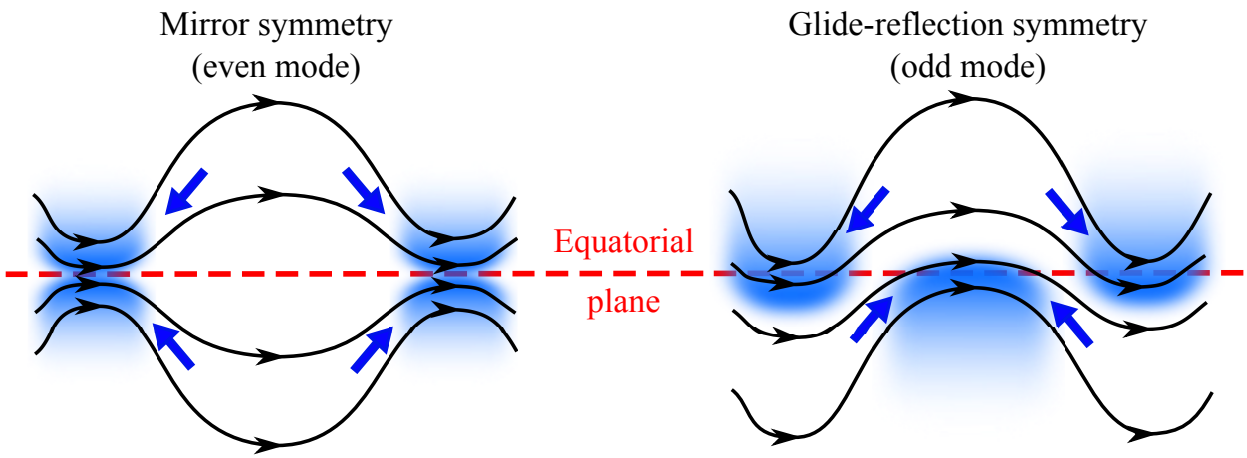

Fig.1.6 Illustration of the magnetic field symmetry in the Parker instability. Left panel shows the mirror symmetry with even parity, and right panel shows the glide-reflection symmetry with odd parity.

Horiuchi et al. (1988) carried out the linear stability analysis of the Parker instability under non-uniform gravity and solved the linearized equations as eigenvalue problem. They showed that the most unstable fundamental mode is the glide-reflection symmetric mode shown in the right hand side of Fig. 1.6, and the first harmonics is the mirror symmetric mode shown in the left hand side of Fig. 1.6. These are slow magnetoacoustic modes modulated by the gravity. The eigen functions have the largest amplitude around the region of maximum gravity and low temperature. Giz & Shu (1993) pointed out that linearized differential equation is identical to the Shrödinger equation. Solutions of the linearized equation can be classified into continuum modes and discrete modes. Dependence on parameters and gravity distribution is studied by Kim, Hong & Ryu (1997) and Kim & Hong (1998). Kamaya et al. (1997) studied the dependence of the solutions on temperature and specific heat ratio.

Two-dimensional MHD numerical simulations of Parker instability were performed by Matsumoto et al. (1988, 1990). They showed that in the non-linear stage, when the magnetic field energy satisfies $|\boldsymbol{B}|^2/2 > 0.3P_g$ and the perturbation wavelength is long enough, shock waves are formed in the region where the supersonic down flow along the magnetic loop hits the gas disk. When the magnetic energy is small (i.e. gas pressure is dominant) and the perturbation length is short enough, the disk nonlinearly oscillates.

The nonlinear acoustic gravity waves modulate the magnetic field. Santillán et al. (2000) reported similar results with different numerical MHD codes and initial perturbations.

1.4 Dynamical Equation of Cosmic Rays

CR energy density is supposed to be in equipartition with the magnetic and thermal energy density. CR's dynamical effect is treated by the CR pressure. In this section, we estimate the energy density of CRs. Next, we focus on the interaction of a CR particle with plasma wave to introduce the CR dynamical equation.

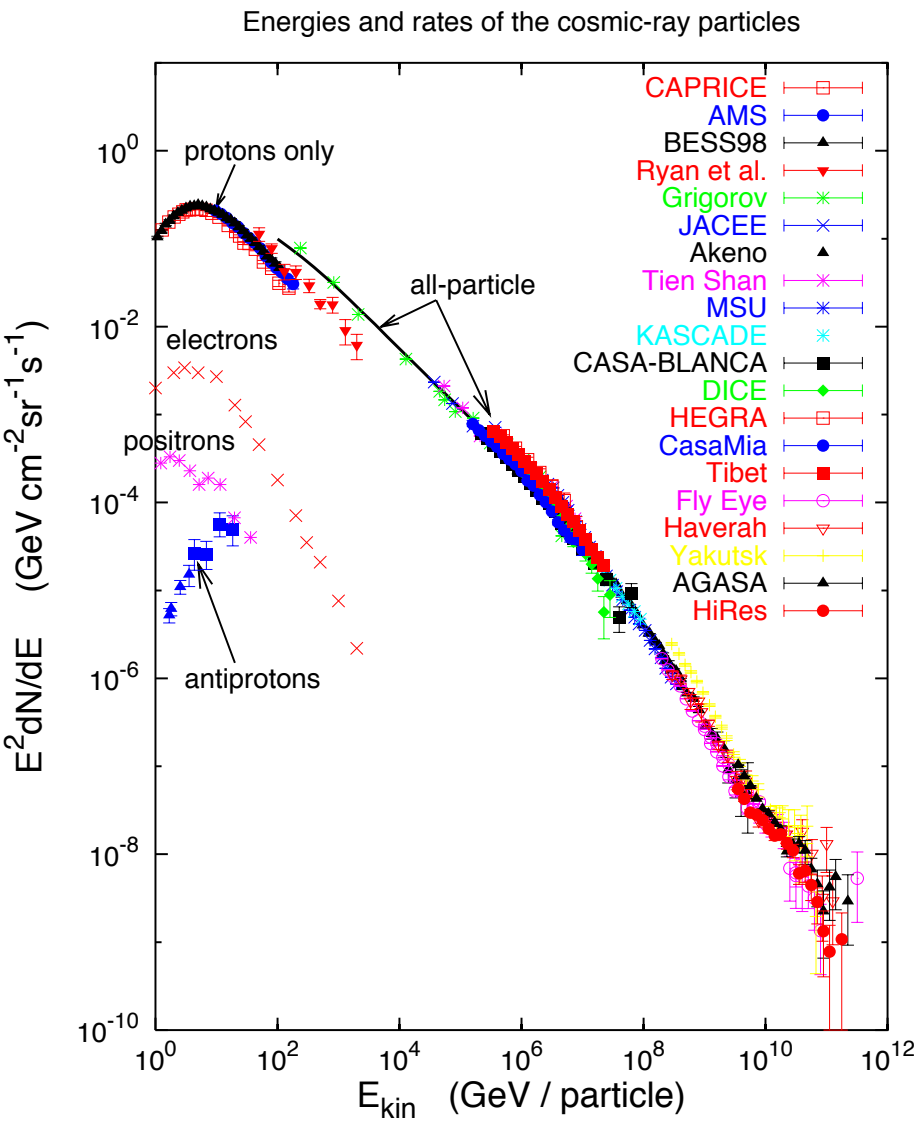

Fig.1.7 Energy spectrum of charged cosmic ray flux over the range of 1 to 10^{12} GeV (Hillas 2006)

Among the energy of various species of CR particles shown in Fig. 1.7, the contribution

of proton is the largest. Hence, CRs energy density $E_{\rm cr}$ is roughly estimated by the order of magnitude estimation using $E^2 dN/dE = 0.1$ and $\Delta E = 1$ GeV,

$$E_{\rm cr} = \frac{4\pi}{c} \int E^2 \frac{dN}{dE} d\,(lnE) \sim 1.4 \times 10^{-12} \ \ {\rm erg\ cm^{-3}}. \tag{1.17}$$

Galactic CR energy spectrum in the range $E_{\rm kin} < 100$ GeV is modulated by 5 μG magnetic field of the heliosphere, since the gyroradius of a CR proton is less than the orbital radius of the earth, 10^{13} cm. If it forms the power-law slope in the low energy range, equation (1.17) underestimates the CR energy density. Energy density of magnetic filed E_B and thermal gas $E_{\rm g}$ have typical value in the interstellar medium,

$$E_B = 1.0 \times 10^{-12} \left[\frac{B}{5\ [\mu{\rm G}]} \right]^2 \ \ {\rm erg\ cm^{-3}}, \tag{1.18}$$

$$E_{\rm g} \sim 0.5 \times 10^{-12} \left[\frac{n}{0.3\ [{\rm cm^{-3}}]} \right] \left[\frac{T}{8000\ [{\rm K}]} \right] \ \ {\rm erg\ cm^{-3}}, \tag{1.19}$$

respectively. Thus, energy density equipartition is approximately satisfied in the interstellar medium.

Next, we discuss a single CR particle motion. When the magnetic field $\boldsymbol{B}_0$ is uniform, a CR proton moves along it with gyrofrequency Ω and gyroradius r_L,

$$\Omega = \frac{e|\boldsymbol{B}_0|}{\gamma m_p c} \sim 0.05 \left[\frac{B_0}{5\ [\mu{\rm G}]} \right] {\rm Hz}, \tag{1.20}$$

$$r_L = \frac{p_{\rm cr} c}{e|\boldsymbol{B}_0|} \sin\theta \sim 2.0 \times 10^{-7} \left[\frac{B_0}{5\ [\mu{\rm G}]} \right]^{-1} \left[\frac{p_{\rm cr} c}{1\ [{\rm GeV}]} \right] \ \ {\rm pc}, \tag{1.21}$$

where $p_{\rm cr}$ and e denote the momentum and charge of protons. The angle between the CR's momentum vector and magnetic field is given by θ which is called the pitch angle.

We consider motion of particles in ordered field $\boldsymbol{B}_0$ superposed with the fluctuation $\delta\boldsymbol{B}$ with wave length $\lambda_B \equiv 2\pi/k$. We illustrate the dependence on the gyroradius in Fig. 1.8. When $r_L \ll \lambda_B$, the magnetic field is uniform for the CR protons, and they gyrate around the magnetic field. In the opposite limit $r_L \gg \lambda_B$, they can not follow the change of magnetic field during the gryration. The most important case is $r_L \sim \lambda_B$. CR protons are reflected by the fluctuation δB. This relation can be considered as scattering

(or collision) process. Remarkably, if turbulent waves and particles propagate from left to right, a CR proton velocity nearly equals to the light speed, but averaged CR protons velocity is zero and they comove with the background fluid.

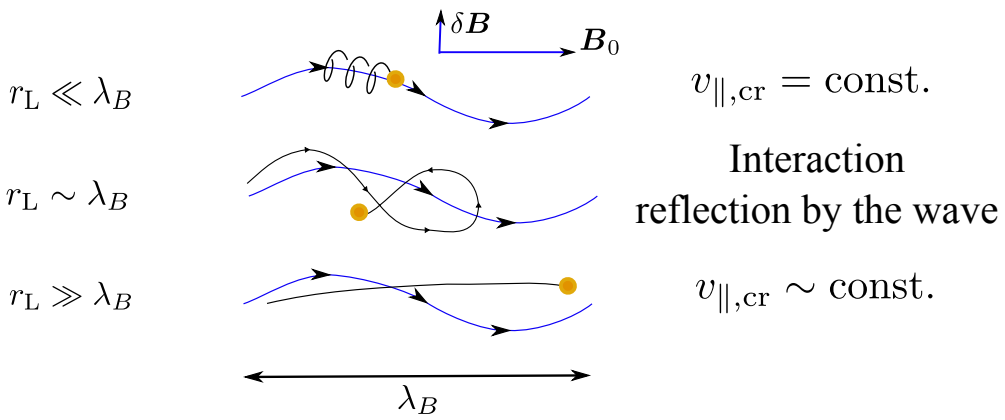

Fig.1.8 A schematic diagram of the interaction between a CR particle and magnetic fluctuation with wave length λ_B. Blue lines denote magnetic filed lines. Black lines denote the trajectory of a CR particle motion.

Let us derive the mean free path and the diffusion coefficient in collision interaction (for detail of this discussion, see Chapter 12 of Kulsrud (2005)). We consider a CR particle approaching the fluctuation field $\delta \boldsymbol{B}$ which is single sinusoidal field traveling the direction of positive z,

$$\boldsymbol{B}_0 = B_0 \boldsymbol{e}_z, \quad \delta \boldsymbol{B} = \delta B \boldsymbol{e}_x \sin\left(kz - \omega t\right), \tag{1.22}$$

where $\boldsymbol{e}_x$ and $\boldsymbol{e}_z$ are unit vector of x- and z-direction. The gyration of CR proton around B_0 can be written as,

$$\boldsymbol{p} = p_{\rm cr} \sin\theta \left\{\boldsymbol{e}_x \sin\left(\Omega t + \phi\right) + \boldsymbol{e}_y \cos\left(\Omega t + \phi\right)\right\} + p_{\rm cr} \cos\theta \boldsymbol{e}_z, \tag{1.23}$$

where ϕ is a phase difference between the CR gyromotion and the fluctuation field. For $\cos\theta > 0$, the momentum change δp_z of single scattering with collision time τ is,

$$\delta p_z = \int \frac{e}{\gamma mc} \left(\boldsymbol{p} \times \boldsymbol{B}\right)_z dt \tag{1.24}$$

$$= p_{\rm cr} \sin\theta \frac{e\delta B}{2\gamma mc} \left[\int \cos\phi dt - \int \cos\left\{\left(k v_{z,\rm cr} - \omega + \Omega\right) t + \phi\right\} dt\right] \tag{1.25}$$

$$\sim p_{\rm cr} \sin\theta \frac{\delta B}{B_0} \frac{\Omega\tau}{2} \cos\phi, \tag{1.26}$$

where we use the resonance condition ($\Omega \gg \omega$),

$$kv_{z,\mathrm{cr}} - \omega - \Omega \sim 0, \tag{1.27}$$

and neglect the integration term with high frequency $kv_{z,\mathrm{cr}} - \omega + \Omega$ compared to τ^{-1}. Since the single collision time is approximately $\tau = 2\pi/(kv_{z,\mathrm{cr}} - \omega) \sim 2\pi/\Omega$, the momentum variation $\delta p_z = \delta(p_{\mathrm{cr}} \cos\theta)$ can be related to the pitch angle variation $\delta\theta$,

$$\delta\theta = -\pi \frac{\delta B}{B_0} \cos\phi \tag{1.28}$$

On the other hand, for $\cos\theta < 0$ when CR particles move in the direction of negative z, the pitch angle variation is $\delta\theta = +\pi \cos\phi \delta B/B_0$ with the resonance condition, $kv_{z,\mathrm{cr}} - \omega + \Omega \sim 0$. CR particles on the same trajectories are scattered by circularly polarized fluctuating field. When we assume that electric field is zero, the energy of the fluctuation field and a CR particle do not change. If a CR particle excites the electric fluctuation field, some instability should exist in CR's gyroradius scale.

Suppose that in a time t, the square of the total change is the sum of $N(= t/\tau)$ collisions, the square of the pitch angle variation averaged over pitch angle can be treated in the same way as the random walk,

$$\left\langle (\Delta\theta)^2 \right\rangle = \sum_{i=1}^{N} \left\langle (\delta\theta_i)^2 \right\rangle = N \left\langle (\delta\theta)^2 \right\rangle \tag{1.29}$$

Hence the scattering rate ν_{cr} can be determined by,

$$\nu_{\mathrm{cr}} = \frac{\left\langle (\Delta\theta)^2 \right\rangle}{t} = \frac{\pi}{4}\Omega \left\langle \left(\frac{\delta B}{B_0} \right)^2 \right\rangle, \tag{1.30}$$

where $< \cos^2\phi >= 1/2$ is taken into account.

Scattering process indicates that dynamical equation can be simplified by using the diffusion approximation. Thus, we estimate the mean free path and diffusion coefficient by this scattering. The mean free path λ_{mfp} and the diffusion coefficient $\kappa_{\parallel}$ depend on

the gyroradius r_L and magnitude $\delta B/B_0$ as,

$$\lambda_{\rm mfp} = \nu_{\rm cr} v_{z,\rm cr} = r_L \frac{4}{\pi} \left(\frac{B_0}{\delta B}\right)^2, \tag{1.31}$$

$$\kappa_{\parallel} = \frac{1}{3}\nu_{\rm cr} v_{z,\rm cr}^2 = r_L v_{z,\rm cr} \frac{4}{3\pi} \left(\frac{B_0}{\delta B}\right)^2 \tag{1.32}$$

According to the quasi-linear theory (see, e.g. Berezinskii et al. 1990; Schlickeiser 2002), the mean free path $\lambda_{\rm mfp}$ taken into account for the turbulence depends additionaly on the power law index of the turbulence spectrum q, magnitude of fluctuation $\delta B/B_0$, and maximum size of turbulence $l_{\rm max}$ as,

$$\begin{aligned}\lambda_{\rm mfp} &\sim r_L \left(\frac{2\pi r_L}{l_{\rm max}}\right)^{1-q} \left(\frac{B_0}{\delta B}\right)^2 \\ &\sim 0.13 \text{ pc} \left[\frac{B_0}{5\ [\mu\text{G}]}\right]^{-\frac{1}{3}} \left[\frac{l_{\rm max}}{100\ [\text{pc}]}\right]^{\frac{2}{3}} \left[\frac{p_{\rm cr} c}{1\ [\text{GeV}]}\right]^{\frac{1}{3}},\end{aligned} \tag{1.33}$$

where we assumed $\delta B/B_0 = O(1)$ and the power law spectral distribution of fluctuation of thermal electron density obeys the Kolmogorov spectrum $q = 5/3$ shown in Fig. 1.9. The energy density of turbulence is comparable with that of the magnetic field. We can also evaluate the diffusion coefficient parallel to the magnetic field (see, e.g. Berezinskii et al. 1990; Schlickeiser 2002),

$$\kappa_{\parallel} = \frac{c\lambda_{\rm mfp}}{3} \sim 1.26 \times 10^{27}\ \text{cm}^2\text{s}^{-1} \left[\frac{B_0}{5\ [\mu\text{G}]}\right]^{-\frac{1}{3}} \left[\frac{l_{\rm max}}{100\ [\text{pc}]}\right]^{\frac{2}{3}} \left[\frac{p_{\rm cr} c}{1\ [\text{GeV}]}\right]^{\frac{1}{3}}. \tag{1.34}$$

And hence, diffusion time scale is,

$$\tau_{\parallel} \sim 2.3 \left[\frac{L}{100\ [\text{pc}]}\right]^2 \text{ Myr}. \tag{1.35}$$

The thermal gas and CR are tightly coupled with the magnetic field.

Let us consider the CR distribution function defined as the number density of particles in phase space of position and momentum. Time evolution of the distribution function f of CR particles can be expressed by the advection-diffusion equation (e.g. Skilling 1975;

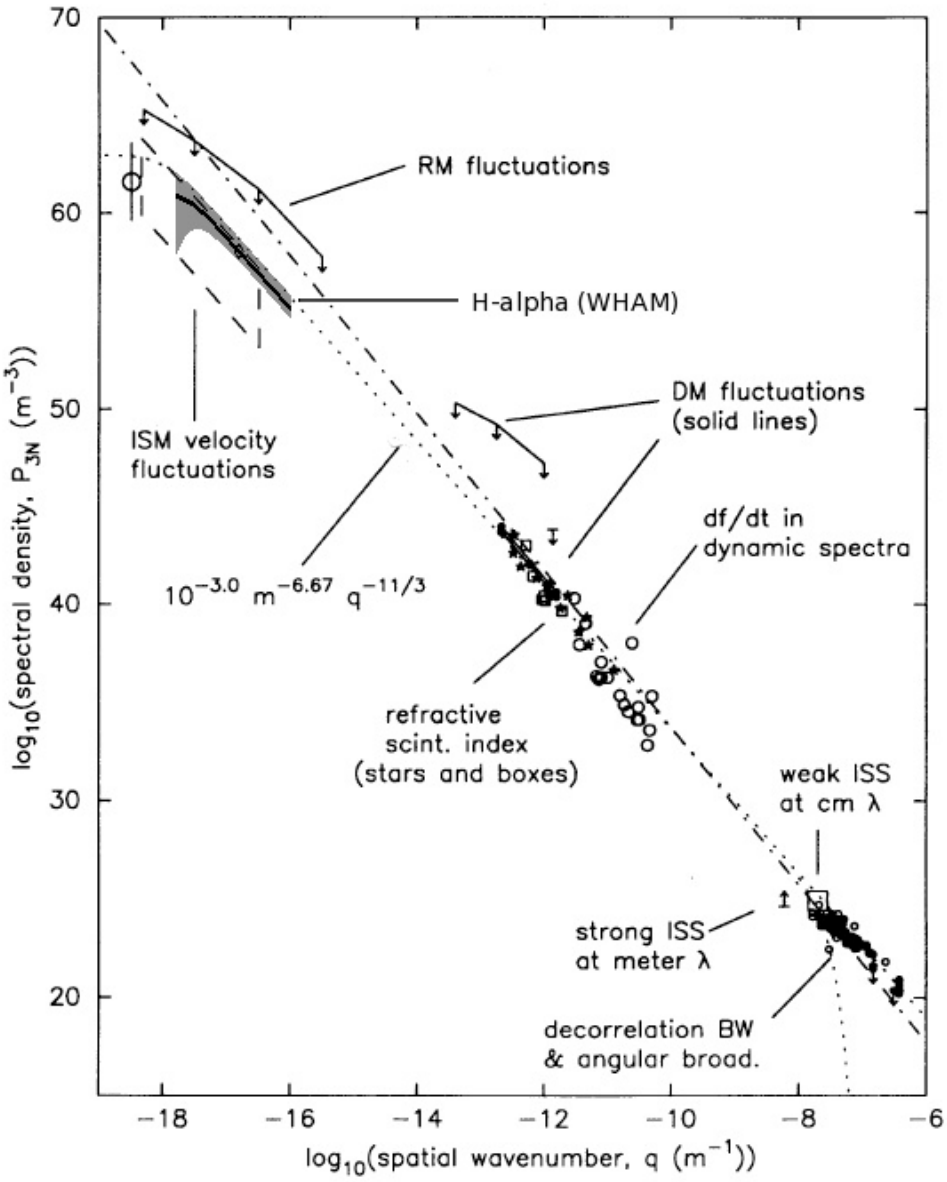

Fig.1.9 Power spectrum of fluctuation of thermal electron number density (Chepurnov & Lazarian 2010 and Armstrong, Rickett & Spangler 1995

Schlickeiser & Lerche 1985)

$$\frac{\partial f}{\partial t} + \boldsymbol{v} \cdot \boldsymbol{\nabla} f - \boldsymbol{\nabla} \cdot \boldsymbol{F}_{4\ \mathrm{diff}} = (\boldsymbol{\nabla} \cdot \boldsymbol{v}) \frac{p}{3} \frac{\partial f}{\partial p} + \frac{1}{p^2} \frac{\partial}{\partial p} \left(D_p \frac{\partial f}{\partial p} \right), \tag{1.36}$$

where $\boldsymbol{F}_{4\ \mathrm{diff}}$ and D_p denote the spatial diffusion flux and momentum diffusion coefficient, and $\boldsymbol{v}$ denotes the background thermal gas flow, respectively. The second and third terms in the left hand side are the advection and diffusion in real space, and the first and the

second terms in the right hand side denote those in momentum space. In this formula the distribution function is assumed to be isotropic in momentum space, $f(\boldsymbol{x}, \boldsymbol{p}, t) = 4\pi f(\boldsymbol{x}, p, t)$, and the energy loss process is ignored. The averaged CR velocity is assumed to be the thermal gas speed $\boldsymbol{v}$ in advection term. Here, we define the CR energy density and pressure as,

$$E_{\rm cr}(x,t) \equiv \int_{p_1}^{p_2} \epsilon f 4\pi p_{\rm cr}^2 dp_{\rm cr}, \tag{1.37}$$

$$P_{\rm cr}(x,t) \equiv \frac{1}{3}\int_{p_1}^{p_2} \boldsymbol{p}_{\rm cr}\cdot\boldsymbol{v}_{\rm cr} f 4\pi p_{\rm cr}^2 dp_{\rm cr}, \tag{1.38}$$

where ϵ is the kinetic energy of the CR particle with velocity $u_{\rm cr}$, momentum $p_{\rm cr}$, and Lorentz factor γ,

$$\epsilon = (\gamma - 1)mc^2, \quad v_{\rm cr} = \frac{p_{\rm cr}}{\gamma m}, \quad \gamma = \sqrt{\frac{p_{\rm cr}^2}{m^2c^2} + 1}. \tag{1.39}$$

To derive the CR energy equation, we multiply equation (1.36) by the CR kinetic energy ϵ and integrate over the momentum space,

$$\frac{\partial E_{\rm cr}}{\partial t} + \boldsymbol{v}\cdot\boldsymbol{\nabla} E_{\rm cr} + (E_{\rm cr} - P_{\rm cr})\boldsymbol{\nabla}\cdot\boldsymbol{v} = \nabla\cdot\boldsymbol{F}_{\rm diff} + \frac{4\pi}{3}(\nabla\cdot\boldsymbol{v})\left[f p_{\rm cr}^3 \epsilon\right]_{p_1}^{p_2}, \tag{1.40}$$

where the spatial diffusion flux is,

$$\boldsymbol{F}_{\rm diff} = \int_{p_1}^{p_2} \epsilon \boldsymbol{F}_{4\ \rm diff}\ 4\pi p_{\rm cr}^2 dp_{\rm cr}. \tag{1.41}$$

The second term in the right-hand of this equation (1.40) vanishes because $p_1 \to 0$ and $p_2 \to \infty$ apploximately. Here, we ignore the momentum diffusion. Since equation (1.40) is not closed, we need additional ad hoc relation for the CR energy and pressure. For this purpose, we introduce the quantity corresponding to the specific heat ratio in the thermo dynamics,

$$\gamma_{\rm cr} = 1 + \frac{P_{\rm cr}}{E_{\rm cr}} = \frac{4}{3} + \frac{1}{3}\frac{\displaystyle\int_{p_1}^{p_2} \epsilon f \gamma^{-1} 4\pi p_{\rm cr}^2 dp_{\rm cr}}{\displaystyle\int_{p_1}^{p_2} \epsilon f 4\pi p_{\rm cr}^2 dp_{\rm cr}} \tag{1.42}$$

In the ultra-relativistic limit $\gamma \to \infty$, $\gamma_{\rm cr} \to 4/3$, while in the non-relativistic limit $\gamma \to 1$, $\gamma_{\rm cr} \to 5/3$. Thus, the specific heat ratio is $4/3 < \gamma_{\rm cr} < 5/3$ and we obtain the CR advection diffusion equation,

$$\frac{\partial}{\partial t}\left(E_{\rm cr}\right) + \boldsymbol{\nabla} \cdot \left[\left(E_{\rm cr} + P_{\rm cr}\right)\boldsymbol{v}\right] = \boldsymbol{v} \cdot \boldsymbol{\nabla} P_{\rm cr} + \boldsymbol{\nabla} \cdot \boldsymbol{F}_{\rm diff} \tag{1.43}$$

Chapter 2

Approximate Riemann Solvers for the Cosmic Ray Magnetohydrodynamical Equations

The dynamics of CRs are often taken into account by the CR magnetohydrodynamical (MHD) equations. This fluid approximation is justified because CRs are confined by the magnetic field and well scattered by small scale magnetic fluctuations (see e.g. Zweibel 2013). CRs are assumed to be an ultrarelativistic gas and hence the pressure is assumed to be one third of the energy density in the CR MHD equations. The CR MHD or CR hydrodynamical (HD) equations have been used for numerical simulations of the interstellar and galactic scales (see e.g. Fahr, Kausch & Scherer 2000; Kuwabara, Nakamura & Ko 2004; Rasera & Chandran 2008; Yang et al. 2012; Hanasz et al. 2013; Salem & Bryan 2014; Vazza et al. 2015).

The CR MHD equations are similar to the ordinary MHD equations and expressed in the conservation form except for the energy equation for CRs. The energy of CRs is enhanced by compression and consumed by work to the thermal gas. Thus the CR energy equation contains a source term proportional to spatial derivative of either pressure or velocity. This source term has been evaluated separately from the flux in the numerical simulations hitherto. However, this treatment does not guarantee that the numerical solutions satisfy

the Rankine-Hugoniot relation for a shock. Although the Rankine-Hugniot relation and Riemann solutions have been obtained by Pfrommer et al. (2006) for the CR HD equations, the approximate Riemann solvers have not been given in the literature. In other words, the effects of CRs on shocks might not be taken into the simulations properly. Remember that modern HD and MHD simulations rely on the appropriate approximate Riemann solvers to reproduce strong shock waves (see e.g. Toro 2009). Good approximate Riemann solvers capture strong shocks sharply without artificial oscillations of numerical origin.

In this chapter, we rewrite the CR MHD equations into the fully conservation form. One of them describes the conservation of CR *particle number*. Here the CR number density is defined to be the $1/\gamma_{\rm cr}$-th power of $P_{\rm cr}$, where $P_{\rm cr}$ and $\gamma_{\rm cr}$ denote the pressure and specific heat ratio of CRs, respectively. The Rankine-Hugoniot relation is easily reconstructed from the fully conservation form. We derive the wave properties of the CR MHD equations such as the characteristics, the corresponding right eigenvectors and wave amplitudes. They are used to construct the Roe-type approximate Riemann solver (see e.g. Toro 2009 for the classification of the approximate Riemann solvers). We show that the approximate Riemann solver works well for 1D shock problems and 2D expansion. The former is used for comparison with the exact solution and those obtained with conventional scheme. When the CR pressure is dominant in the post-shocked gas, the solutions obtained with the conventional schemes do not satisfy the Rankine-Hugoniot relation. On the other hand, the Roe-type approximate Riemann solver reproduces the pressure balance mode, a kind of contact discontinuity appearing in the CR MHD equation, as well as the shock.

This chapter is organized as follows. We derive the fully conservation form of the CR MHD equations in Section 2.2. The Rankine-Hugoniot relation is derived in Section 2.2.1. The approximate Riemann solution is given in Section 2.2.2. Numerical tests are shown in Section 2.3. Section 2.3.1 is devoted to the 1D CR HD shock tube problem. Section 2.3.2 is devoted to the linear wave test, while Section 2.3.3 to the advection of the pressure balance mode. Section 2.3.4 is devoted to the 1D CR MHD shock tube problem, while Section 2.3.5 is to 2D CR MHD problem. We discuss the shock tube problems solved by Pfrommer et al. (2006) and Dubois & Commerçon (2016) in Appendix B. We also discuss possible extension of the CR MHD equations to evaluate the average CR particle energy before conclusion. This paper is based on our earlier work, Kudoh & Hanawa (2016a),

but improved to achieve the second-order accuracy.

2.1 System of CR MHD equations

2.1.1 Cosmic Ray Magnetohydrodynamic Equations

First we introduce the CR MHD equations according to Berezinskii et al. (1990) in which the fluid approximation is applied to CRs. The equation of continuity,

$$\frac{\partial \rho}{\partial t} + \boldsymbol{\nabla} \cdot (\rho \boldsymbol{v}) = 0, \tag{2.1}$$

and the induction equation,

$$\frac{\partial \boldsymbol{B}}{\partial t} - \boldsymbol{\nabla} \times (\boldsymbol{v} \times \boldsymbol{B}) = 0, \tag{2.2}$$

are the same as those of the ordinary MHD equations. Here the symbols, ρ, $\boldsymbol{v}$, and $\boldsymbol{B}$ denote the density, velocity, and magnetic field, respectively. The CR pressure, P_{cr}, is taken into account in the equation of motion,

$$\frac{\partial}{\partial t}(\rho \boldsymbol{v}) + \boldsymbol{\nabla} \cdot \left[\rho \boldsymbol{v}\boldsymbol{v} + \left(P_{\mathrm{g}} + P_{\mathrm{cr}} + \frac{|\boldsymbol{B}|^2}{2} \right) \mathbf{I} - \boldsymbol{B}\boldsymbol{B} \right] = 0, \tag{2.3}$$

where P_{g} and $\mathbf{I}$ denote the gas pressure and the unit tensor, respectively. Accordingly the equation of energy conservation is altered into

$$\frac{\partial}{\partial t}(E) + \boldsymbol{\nabla} \cdot [(E + P_{\mathrm{g}})\, \boldsymbol{v} - (\boldsymbol{v} \cdot \boldsymbol{B})\, \boldsymbol{B}] = -\boldsymbol{v} \cdot \boldsymbol{\nabla} P_{\mathrm{cr}}, \tag{2.4}$$

$$E = \frac{\rho}{2}|\boldsymbol{v}|^2 + \frac{P_{\mathrm{g}}}{\gamma_{\mathrm{g}} - 1} + \frac{|\boldsymbol{B}|^2}{2}, \tag{2.5}$$

where γ_{g}, denotes the specific heat ratio of the gas. The gas is assumed to be an ideal gas with $\gamma_{\mathrm{g}} = 5/3$ throughout this paper except when otherwise noted.

CRs are approximated to be an ideal gas having the constant specific heat ratio, $\gamma_{\mathrm{cr}} =$

4/3. Then the CR energy density, $E_{\rm cr}$, is evaluated to be

$$E_{\rm cr} = \frac{P_{\rm cr}}{\gamma_{\rm cr} - 1}. \tag{2.6}$$

The CR energy equation is expressed as

$$\frac{\partial}{\partial t}\left(E_{\rm cr}\right) + \boldsymbol{\nabla}\cdot\left[\left(E_{\rm cr} + P_{\rm cr}\right)\boldsymbol{v}\right] = \boldsymbol{v}\cdot\boldsymbol{\nabla}P_{\rm cr} - \boldsymbol{\nabla}\cdot\boldsymbol{F}_{\rm diff}, \tag{2.7}$$

$$\boldsymbol{F}_{\rm diff} = -\kappa_{\perp}\boldsymbol{\nabla}E_{\rm cr} - \left(\kappa_{\parallel} - \kappa_{\perp}\right)\frac{\left(\boldsymbol{B}\cdot\boldsymbol{\nabla}E_{\rm cr}\right)\boldsymbol{B}}{|\boldsymbol{B}|^2}, \tag{2.8}$$

where advection, the work to accelerate the gas, and diffusion are taken into account. The symbols, $\kappa_{\parallel}$ and $\kappa_{\perp}$, denote the diffusion coefficients in the directions parallel and perpendicular to the magnetic field, respectively.

In the following we analyze the case of no diffusion ($\kappa_{\parallel} = \kappa_{\perp} = 0$). As shown later, the CR MHD equations are hyperbolic and the characteristic speeds are independent of the wavelength in this case. Remember that the diffusion is often taken account separately in numerical simulations by means of the operator splitting. In other words, the diffusion is not taken into account in the construction of approximate Riemann solutions. Thus our approach to the CR MHD equation is orthodox.

2.2 Fully Conservation Form

Next we rewrite the CR MHD equations in the fully conservation form. While equations (2.1), (2.2) and (2.3) are written in the conservation form, equations (2.4) and (2.7) are not. The sum of equations (2.4) and (2.7) gives us the equation of the total energy conservation,

$$\frac{\partial}{\partial t}\left(E + E_{\rm cr}\right) + \boldsymbol{\nabla}\cdot\left[\left(E + E_{\rm cr} + P_{\rm g} + P_{\rm cr} + \frac{|\boldsymbol{B}|^2}{2}\right)\boldsymbol{v} - \left(\boldsymbol{v}\cdot\boldsymbol{B}\right)\boldsymbol{B}\right] = 0. \tag{2.9}$$

Thus the CR MHD equations are expressed in the fully conservation form if equation (2.7) is converted into the conservation form.

For later convenience we introduce the CR number density defined as

$$\rho_{\rm cr} \equiv P_{\rm cr}^{1/\gamma_{\rm cr}}, \tag{2.10}$$

which is equivalent to equation (3.6) in Pfrommer et al. (2006). Equation (2.10) implies that CRs is approximated by a polytrope gas. Then equation (2.7) is rewritten in the conservation form,

$$\frac{\partial}{\partial t}\rho_{\rm cr} + \boldsymbol{\nabla}\cdot(\rho_{\rm cr}\boldsymbol{v}) = 0, \tag{2.11}$$

when $\kappa_{\parallel} = \kappa_{\perp} = 0$.

Note the similarity between equations (2.1) and (2.11). From these equations we can derive

$$\frac{d}{dt}\left(\frac{\rho_{\rm cr}}{\rho}\right) = 0. \tag{2.12}$$

For later convenience we introduce the concentration of CRs defined as

$$\chi = \frac{\rho_{\rm cr}}{\rho}. \tag{2.13}$$

When all the variables depend only on t and x (1D), the CR MHD equations are expressed in the vector form,

$$\frac{\partial \boldsymbol{U}}{\partial t} + \frac{\partial \boldsymbol{F}}{\partial x} = 0, \tag{2.14}$$

$$\boldsymbol{U} = \begin{bmatrix} \rho \\ \rho v_x \\ \rho v_y \\ \rho v_z \\ B_x \\ B_y \\ B_z \\ \rho H - P_{\rm T} + \dfrac{|\boldsymbol{B}|^2}{2} \\ \rho\chi \end{bmatrix}, \tag{2.15}$$

$$\boldsymbol{F} = \begin{bmatrix} \rho v_x \\ \rho v_x^2 + P_{\mathrm{T}} + \dfrac{|\boldsymbol{B}|^2}{2} - B_x^2 \\ \rho v_x v_y - B_x B_y \\ \rho v_x v_z - B_x B_z \\ 0 \\ v_x B_y - v_y B_x \\ v_x B_z - v_z B_x \\ \rho H v_x + |\boldsymbol{B}|^2 v_x - (\boldsymbol{v} \cdot \boldsymbol{B}) B_x \\ \rho \chi v_x \end{bmatrix}, \tag{2.16}$$

$$H = \frac{\boldsymbol{v}^2}{2} + \frac{\gamma_{\mathrm{g}}}{\gamma_{\mathrm{g}} - 1} \frac{P_{\mathrm{g}}}{\rho} + \frac{\gamma_{\mathrm{cr}}}{\gamma_{\mathrm{cr}} - 1} \frac{P_{\mathrm{cr}}}{\rho}, \tag{2.17}$$

$$P_{\mathrm{T}} = P_{\mathrm{g}} + P_{\mathrm{cr}}. \tag{2.18}$$

where $\boldsymbol{U}$ and $\boldsymbol{F}$ denote the state and flux vectors, respectively. We use this vector form to derive the Rankine-Hugniot relation and Riemann solution.

2.2.1 Rankine-Ugoniot Relation

In this subsection we derive the Rankine-Hugoniot relation, i.e, the jump condition at a shock front, using the CR MHD equations in the conservation form, equations (2.14), (2.15) and (2.16). For simplicity we restrict ourselves to a stationary plane shock. In other words, we observe a small area around a shock wave in the comoving frame. Furthermore, the wave front is assumed to be normal to the x-direction in the Cartesian coordinates. Since the temporal change vanishes, then the flux, $\boldsymbol{F}$, should be continuous across the

shock front,

$$[\rho v_x] = 0, \tag{2.19}$$

$$\left[\rho v_x^2 + P_{\mathrm{T}} + \frac{B_y^2 + B_z^2 - B_x^2}{2}\right] = 0, \tag{2.20}$$

$$[\rho v_x v_y - B_x B_y] = 0, \tag{2.21}$$

$$[\rho v_x v_z - B_x B_z] = 0, \tag{2.22}$$

$$[v_x B_y - v_y B_x] = 0, \tag{2.23}$$

$$[v_x B_z - v_z B_x] = 0, \tag{2.24}$$

$$\left[\rho H v_x + \left(B_y^2 + B_z^2\right) v_x - \left(v_y B_y + v_z B_z\right) B_x\right] = 0, \tag{2.25}$$

$$[\rho \chi v_x] = 0, \tag{2.26}$$

where the symbol $[\cdot]$ denotes the jump across the discontinuity. Here, the subscripts, x, y, and z denote the x-, y-, and z-components, respectively. These conditions are the same as those obtained by Pfrommer et al. (2006) and almost the same as those for the MHD equations except for equation (2.26): equations (2.20) and (2.25) are modified to include P_{cr} and E_{cr}. Equation (2.26) denotes the continuity of the CR number flux. Combining equations (2.19) through (2.26) we obtain

$$\frac{\rho_{\mathrm{cr}}}{\rho} = \chi = \text{const.}, \tag{2.27}$$

across the shock. This means that the CR pressure changes only through the gas compression or expansion.

2.2.2 Elementary Wave Solutions of the Riemann Problem

First we examine the CR HD equations, since inclusion of CRs changes the equation of state but does not alter the induction equation. Furthermore we consider a 1D flow in

which the y- and z-components vanish. Then the state and flux vectors are expressed as

$$\boldsymbol{U} = \begin{bmatrix} \rho \\ \rho v_x \\ \rho H - P_{\mathrm{T}} \\ \rho\chi \end{bmatrix}, \tag{2.28}$$

$$\boldsymbol{F} = \begin{bmatrix} \rho v_x \\ \rho v_x^2 + P_{\mathrm{T}} \\ \rho H v_x \\ \rho\chi v_x \end{bmatrix}. \tag{2.29}$$

As shown later, inclusion of the tangential velocity and magnetic field are straight forward.

CRs increase the total pressure and hence the sound speed. The total pressure is expressed as

$$P_{\mathrm{T}} = P_{\mathrm{g}} + (\chi\rho)^{\gamma_{\mathrm{cr}}}, \tag{2.30}$$

as shown in the previous subsection. Then the adiabatic sound speed is evaluated to be

$$a = \left[\left(\frac{\partial P_{\mathrm{g}}}{\partial \rho}\right)_s + \left(\frac{\partial P_{\mathrm{cr}}}{\partial \rho}\right)_\chi\right]^{1/2} = \left(\frac{\gamma_{\mathrm{g}} P_{\mathrm{g}} + \gamma_{\mathrm{cr}} P_{\mathrm{cr}}}{\rho}\right)^{1/2}, \tag{2.31}$$

$$s = \ln P_{\mathrm{g}} - \gamma_{\mathrm{g}} \ln \rho, \tag{2.32}$$

where s denotes the entropy, since $d\chi/dt = 0$ (equation (2.12)). Note that the entropy is constant

$$\frac{ds}{dt} = 0, \tag{2.33}$$

for a given gas element except for increase at a shock.

The characteristics of the CR HD equations are the eigenvalues of the Jacobian matrix,

$$\boldsymbol{A} \equiv \partial \boldsymbol{F} / \partial \boldsymbol{U}. \tag{2.34}$$

We obtain four characteristics,

$$\lambda_{1,4} = v_x \pm a, \tag{2.35}$$

$$\lambda_{2,3} = v_x. \tag{2.36}$$

after some algebra. The former denotes the sound wave while the latter does advection. The additional advection mode corresponds to conservation of the CR concentration (equation (2.27)) and hence to the pressure balance mode. The others are the same as those in the ordinary HD equations except for the change in the sound speed.

The spatial derivative of $\boldsymbol{U}$ and $\boldsymbol{F}$ are decomposed into waves. They are expressed as

$$\frac{\partial \boldsymbol{U}}{\partial x} = \sum_{i=1}^{4} w_i \boldsymbol{r}_i, \tag{2.37}$$

$$\frac{\partial \boldsymbol{F}}{\partial x} = \sum_{i=1}^{4} \lambda_i w_i \boldsymbol{r}_i, \tag{2.38}$$

where

$$w_{1,4} = \frac{1}{2a^2}\left(\frac{\partial P_{\mathrm{T}}}{\partial x} \pm \rho a \frac{\partial v_x}{\partial x}\right), \tag{2.39}$$

$$w_2 = \frac{\partial \rho}{\partial x} - \frac{1}{a^2}\frac{\partial P_{\mathrm{T}}}{\partial x} = -\frac{P_{\mathrm{g}}}{a^2}\frac{\partial s}{\partial x} - \frac{\rho \chi^{-1}}{a^2}\left(\frac{\partial P_{\mathrm{cr}}}{\partial \rho}\right)_{\chi}\frac{\partial \chi}{\partial x}, \tag{2.40}$$

$$w_3 = \frac{\partial \rho_{\mathrm{cr}}}{\partial x} - \chi \frac{\partial \rho}{\partial x} = \rho \frac{\partial \chi}{\partial x}, \tag{2.41}$$

$$\boldsymbol{r_{1,4}} = \begin{bmatrix} 1 \\ v_x \pm a \\ H \pm a v_x \\ \chi \end{bmatrix}, \quad \boldsymbol{r_2} = \begin{bmatrix} 1 \\ v_x \\ \frac{v_x^2}{2} + \chi\zeta \\ \chi \end{bmatrix}, \quad \boldsymbol{r_3} = \begin{bmatrix} 0 \\ 0 \\ \zeta \\ 1 \end{bmatrix}, \tag{2.42}$$

$$\zeta = \frac{\gamma_{\mathrm{g}} - \gamma_{\mathrm{cr}}}{(\gamma_{\mathrm{g}} - 1)(\gamma_{\mathrm{cr}} - 1)}\frac{dP_{\mathrm{cr}}}{d\rho_{\mathrm{cr}}}. \tag{2.43}$$

Here the symbol, w_i, denotes the amplitude of the i-th wave. Inclusion of CRs introduces

a new Riemann invariant, χ, and change the other Riemann invariants only slightly. The symbol, ζ, denotes the change in the energy density due to the pressure balance mode (Webb et al. (1995)). The energy density depends on the proportion of $P_{\rm cr}$ for a given $P_{\rm T}$.

Equaions (2.37) through (2.42) are used to construct the Roe (1981) type approximate Riemann solvers for numerical simulations.

Also the exact Riemann solutions are derived from equations (2.37) through (2.42). Here the Riemann solution means that the solution of equation (2.14), when the initial condition is expressed as

$$\boldsymbol{U} = \begin{cases} \boldsymbol{U}_{\rm L} & x < 0 \\ \boldsymbol{U}_{\rm R} & x \geq 0 \end{cases}, \tag{2.44}$$

at $t = 0$. The Riemann solution is obtained from the conditions,

$$w_i = 0, \tag{2.45}$$

except at discontinuities. However, the algorithm to obtain the complete solution is lengthy even for the ordinary HD equations, as shown in Toro (2009). Pfrommer et al. (2006) showed the Riemann solution for the case in which a shock propagates rightward and a rarefaction wave propagates leftward.

Figure 2.1 illustrates an example of the Riemann solution. In this solution a shock wave travels at the speed, λ_1, while the contact discontinuity and the pressure balance mode at $\lambda_2 (= \lambda_3)$. The rarefaction wave has the head and tail. The state vector is uniform in each region separated by the characteristics except between the head and tail of the rarefaction wave. We refer to regions 1 through 5 from right to left in the figure. The Rankine-Hugoniot relation is applied to the jump between regions 1 and 2. The total pressure and velocity are continuous at the boundary between regions 2 and 3, while the entropy and CR concentration are not. The velocity gradient in region 4 is obtained from

$$\frac{dv_x}{dx} = \frac{1}{\rho a}\frac{dP_{\rm T}}{dx}, \tag{2.46}$$

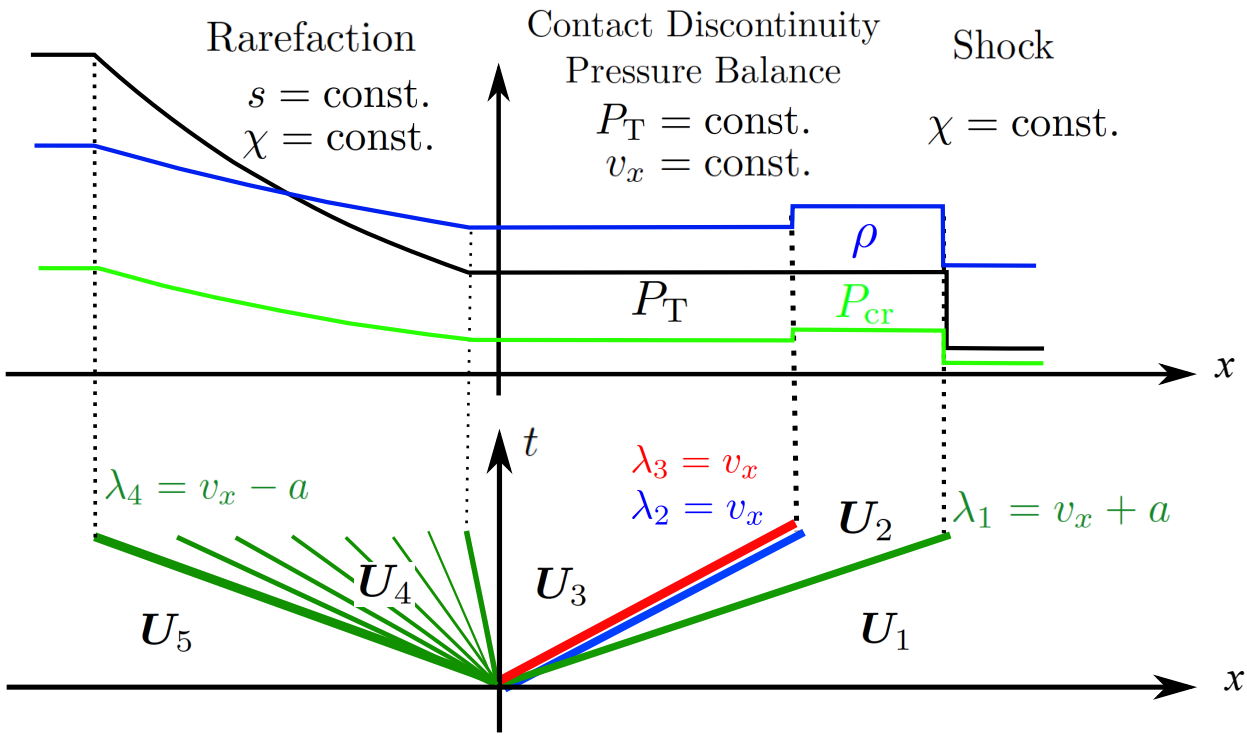

Fig.2.1 Illustration of the Riemann solution for a CR HD shock tube problem. The density, total pressure and CR pressure are shown as a function of x in the upper half. The lower half denotes the characteristics.

$s = \text{const.}$, $\chi = \text{const.}$, and $\lambda_4 = v_x - a$. The state vector remains at the initial value, $\boldsymbol{U}_1 = \boldsymbol{U}_\mathrm{R}$ and $\boldsymbol{U}_5 = \boldsymbol{U}_\mathrm{L}$, in regions 1 and 5. In short the Riemann solution changes only quantitatively by inclusion of CRs.

Next we consider the Riemann solution of the CR MHD equations. The ordinary MHD equations have 7 characteristics: three pairs of the fast, slow, and Alfvén waves in addition to the entropy wave. CRs add the pressure balance mode and modify the phase speeds of the fast and slow waves through the change in the sound speed. After some algebra, we have found the following formulae for λ_i, w_i, and $\boldsymbol{r}_i$ for the CR MHD equations using the formulation given by Ryu & Jones (1995) for the ordinary MHD equations.

$$\lambda_{1,8} = v_x \pm c_f, \tag{2.47}$$

$$\lambda_{3,6} = v_x \pm c_s, \tag{2.48}$$

$$\lambda_{4,5} = v_x, \quad \lambda_{2,7} = v_x \pm v_{\mathrm{A}x}, \tag{2.49}$$

$$
\begin{aligned}
w_1 + w_8 = {} & \frac{\alpha_f}{c_f^2}\left(\frac{\partial P_{\mathrm{T}}}{\partial x} + B_y\frac{\partial B_y}{\partial x} + B_z\frac{\partial B_z}{\partial x}\right) \\
& + \left[\frac{\alpha_s\sqrt{\rho}}{a^2 c_f}\left\{(\gamma_{\mathrm{g}}-1)\,c_s^2 - (\gamma_{\mathrm{g}}-2)\,a^2\right\}\right. \\
& \left. + \frac{\alpha_f}{c_f^2}(\gamma_{\mathrm{g}}-2)\sqrt{B_y^2+B_z^2}\right]\left(\beta_y\frac{\partial B_y}{\partial x} + \beta_z\frac{\partial B_z}{\partial x}\right),
\end{aligned}
\tag{2.50}
$$

$$
w_1 - w_8 = \frac{\alpha_f}{c_f}\rho\frac{\partial v_x}{\partial x} - \frac{\alpha_s c_s}{c_f a}\rho\,\mathrm{sgn}\,(B_x)\left(\beta_y\frac{\partial B_y}{\partial x} + \beta_z\frac{\partial B_z}{\partial x}\right),
\tag{2.51}
$$

$$
\begin{aligned}
w_3 + w_6 = {} & \frac{\alpha_s}{a^2}\left(\frac{\partial P_{\mathrm{T}}}{\partial x} + B_y\frac{\partial B_y}{\partial x} + B_z\frac{\partial B_z}{\partial x}\right) \\
& + \left[\frac{\alpha_f\sqrt{\rho}}{a^2 c_f}\left\{(\gamma_{\mathrm{g}}-2)\,a^2 - (\gamma_{\mathrm{g}}-1)\,c_f^2\right\}\right. \\
& \left. + \frac{\alpha_s}{a^2}(\gamma_{\mathrm{g}}-2)\sqrt{B_y^2+B_z^2}\right]\left(\beta_y\frac{\partial B_y}{\partial x} + \beta_z\frac{\partial B_z}{\partial x}\right),
\end{aligned}
\tag{2.52}
$$

$$
w_3 - w_6 = \frac{\alpha_s v_{\mathrm{A}x}}{c_f a}\rho\frac{\partial v_x}{\partial x} + \frac{\alpha_f}{a}\rho\,\mathrm{sgn}\,(B_x)\left(\beta_y\frac{\partial B_y}{\partial x} + \beta_z\frac{\partial B_z}{\partial x}\right),
\tag{2.53}
$$

$$
w_4 = \frac{\partial\rho}{\partial x} - \alpha_f(w_1 + w_8) - \alpha_s(w_3 + w_6),
\tag{2.54}
$$

$$
w_5 = \rho\frac{\partial\chi}{\partial x},
\tag{2.55}
$$

$$
\begin{aligned}
w_{2,7} = \frac{1}{2}\Bigg[& \mp\rho\left(\beta_z\frac{\partial v_y}{\partial x} - \beta_y\frac{\partial v_z}{\partial x}\right)\mathrm{sgn}\,(B_x) \\
& + \sqrt{\rho}\left(\beta_z\frac{\partial B_y}{\partial x} - \beta_y\frac{\partial B_z}{\partial x}\right)\Bigg],
\end{aligned}
\tag{2.56}
$$

$$\boldsymbol{r}_{1,8} = \begin{bmatrix} \alpha_f \\ \alpha_f(v_x \pm c_f) \\ \alpha_f v_y \mp \alpha_s \beta_y v_{Ax} \mathrm{sgn}(B_x) \\ \alpha_f v_z \mp \alpha_s \beta_z v_{Ax} \mathrm{sgn}(B_x) \\ \dfrac{\alpha_s \beta_y c_f}{\sqrt{\rho}} \\ \dfrac{\alpha_s \beta_z c_f}{\sqrt{\rho}} \\ R_{1,8} \\ \alpha_f \chi \end{bmatrix}, \tag{2.57}$$

$$\boldsymbol{r}_{3,6} = \begin{bmatrix} \alpha_s \\ \alpha_s(v_x \pm c_s) \\ \alpha_s v_y \pm \alpha_f \beta_y a \mathrm{sgn}(B_x) \\ \alpha_s v_z \mp \alpha_f \beta_z a \mathrm{sgn}(B_x) \\ -\dfrac{\alpha_f \beta_y a^2}{c_f \sqrt{\rho}} \\ -\dfrac{\alpha_f \beta_z a^2}{c_f \sqrt{\rho}} \\ R_{3,6} \\ \alpha_s \chi \end{bmatrix}, \tag{2.58}$$

$$\boldsymbol{r}_{2,7} = \begin{bmatrix} 0 \\ 0 \\ \mp \beta_z \mathrm{sgn}(B_x) \\ \pm \beta_y \mathrm{sgn}(B_x) \\ \beta_z / \sqrt{\rho} \\ -\beta_y / \sqrt{\rho} \\ R_{2,7} \\ 0 \end{bmatrix}, \quad \boldsymbol{r}_4 = \begin{bmatrix} 1 \\ v_x \\ v_y \\ v_z \\ 0 \\ 0 \\ R_4 \\ \chi \end{bmatrix}, \quad \boldsymbol{r}_5 = \begin{bmatrix} 0 \\ 0 \\ 0 \\ 0 \\ 0 \\ 0 \\ \zeta \\ 1 \end{bmatrix}, \tag{2.59}$$

where,

$$R_4 = \frac{|\boldsymbol{v}|^2}{2} + \chi\zeta, \quad R_{2,7} = \mp (\beta_z v_y - \beta_y v_z) \, \mathrm{sgn}(B_x), \tag{2.60}$$

$$R_{1,8} = \alpha_f \left\{ R_4 \pm c_f v_x + \frac{c_f^2}{\gamma_{\rm g} - 1} + \frac{\gamma_{\rm g} - 2}{\gamma_{\rm g} - 1} \left(c_f^2 - a^2 \right) \right\} \mp \alpha_s v_{Ax} \ \mathrm{sgn}(B_x) \left(\beta_y v_y + \beta_z v_z \right), \tag{2.61}$$

$$R_{3,6} = \alpha_s \left\{ R_4 \pm c_s v_x + \frac{c_s^2}{\gamma_{\rm g} - 1} \pm \frac{\gamma_{\rm g} - 2}{\gamma_{\rm g} - 1} \left(c_s^2 - a^2 \right) \right\} \pm \alpha_f a \ \mathrm{sgn}(B_x) \left(\beta_y v_y + \beta_z v_z \right), \tag{2.62}$$

$$v_{Ax}^2 = \frac{B_x^2}{\rho}, \quad a_*^2 = a^2 + \frac{B_x^2 + B_y^2 + B_z^2}{\rho}, \tag{2.63}$$

$$c_{f,s}^2 = \frac{1}{2} \left(a_*^2 \pm \sqrt{a_*^4 - 4a^2 v_{Ax}^2} \right), \tag{2.64}$$

$$\alpha_f = \frac{\sqrt{c_f^2 - v_{Ax}^2}}{\sqrt{c_f^2 - c_s^2}}, \quad \alpha_s = \frac{\sqrt{c_f^2 - a^2}}{\sqrt{c_f^2 - c_s^2}}, \quad \alpha_f^2 + \frac{v_{Ax}^2}{c_f^2} \alpha_s^2 = 1, \tag{2.65}$$

$$\beta_y = \frac{B_y}{\sqrt{B_y^2 + B_z^2}}, \quad \beta_z = \frac{B_z}{\sqrt{B_y^2 + B_z^2}}, \quad \beta_y^2 + \beta_z^2 = 1. \tag{2.66}$$

The above formulae are also used to construct the Roe type approximate Riemann solutions. It is difficult to obtain the exact CR MHD Riemann solution although it may not be impossible.

2.3 Numerical Tests

We derive the Roe-type approximate Riemann solver for the CR MHD equations from equations (2.47) through (2.66). They show that the spatial difference is decomposed into eight waves. When the wave speeds (λ_i) and eigenvectors ($\boldsymbol{r}_i$) are evaluated by the Roe-average defined as

$$
\begin{aligned}
\bar{\rho} &= \sqrt{\rho_{j+1}\rho_j}, \quad \bar{v}_x = \frac{\sqrt{\rho_{j+1}}v_{x,j+1} + \sqrt{\rho_j}v_{x,j}}{\sqrt{\rho_{j+1}} + \sqrt{\rho_j}}, \\
\bar{H} &= \frac{\sqrt{\rho_{j+1}}H_{j+1} + \sqrt{\rho_j}H_j}{\sqrt{\rho_{j+1}} + \sqrt{\rho_j}}, \\
\bar{P}_{\mathrm{T}} &= \frac{\sqrt{\rho_{j+1}}P_{\mathrm{T},j} + \sqrt{\rho_j}P_{\mathrm{T},j+1}}{\sqrt{\rho_{j+1}} + \sqrt{\rho_j}}, \\
\bar{B}_y &= \frac{\sqrt{\rho_j}B_{y,j+1} + \sqrt{\rho_{j+1}}B_{y,j}}{\sqrt{\rho_{j+1}} + \sqrt{\rho_j}}, \bar{B}_z = \frac{\sqrt{\rho_j}B_{z,j+1} + \sqrt{\rho_{j+1}}B_{z,j}}{\sqrt{\rho_{j+1}} + \sqrt{\rho_j}}, \\
\bar{\rho}_{\mathrm{cr}} &= \frac{\sqrt{\rho_{j+1}}\rho_{\mathrm{cr},j} + \sqrt{\rho_j}\rho_{\mathrm{cr},j+1}}{\sqrt{\rho_{j+1}} + \sqrt{\rho_j}}.
\end{aligned}
\tag{2.67}
$$

the spatial difference is decomposed into the linear combination at the waves completely (see e.g. Toro (2009)). Here the subscripts, j and $j+1$, specify the cells at the centre of which the variables are evaluated. As a results of $\Delta U = A\Delta F$, we determine the sound wave,

$$
\bar{a}^2 = (\gamma_{\mathrm{g}} - 1)\left(\bar{H} - \frac{\bar{v}_x^2 + \bar{v}_y^2 + \bar{v}_z^2}{2} + \frac{\bar{B}_x^2 + \bar{B}_y^2 + \bar{B}_z^2}{\bar{\rho}} - \delta b^2 - \frac{\bar{\rho}_{\mathrm{cr}}}{\bar{\rho}}\zeta\right), \tag{2.68}
$$

where,

$$
\delta b^2 = \frac{\gamma_{\mathrm{g}} - 2}{\gamma_{\mathrm{g}} - 1}\frac{\left(B_{y,j+1} - B_{y,j}\right)^2 + \left(B_{z,j+1} - B_{z,j}\right)^2}{2\left(\sqrt{\rho_{j+1} + \sqrt{\rho_j}}\right)}, \tag{2.69}
$$

$$
\zeta = \frac{\gamma_{\mathrm{g}} - \gamma_{\mathrm{cr}}}{(\gamma_{\mathrm{g}} - 1)(\gamma_{\mathrm{cr}} - 1)}\frac{P_{\mathrm{cr},j+1} - P_{\mathrm{cr},j}}{\rho_{\mathrm{cr},j+1} - \rho_{\mathrm{cr},j}}. \tag{2.70}
$$

The Roe-type numerical flux is given by

$$
\boldsymbol{F}_{j+1/2}^{\mathrm{Roe}} = \frac{1}{2}\left(\boldsymbol{F}_{j+1} + \boldsymbol{F}_j - \sum_i w_i|\lambda_i|\boldsymbol{r}_i\right), \tag{2.71}
$$

where the subscript $j+1/2$ denotes the value on the surface between the j-th and $j+1$-th cells.

We use the explicit scheme of the second order accuracy in space and time except when otherwise noted. The second order accuracy in space is achieved by the Monotone Upstream-Centered Schemes for Conservation Laws (MUSCL) with characteristics (van

Table. 2.1 The initial state in the CR HD shock tube problem.

	ρ	v_x	$P_{\rm g}$	$P_{\rm cr}$
left ($x < 0$)	1.0	0.0	2.0	1.0
right ($x \geq 0$)	0.2	0.0	0.02	0.1

Leer 1979; and see e.g. Toro 2009). When we solve equation (2.7), we interpolate the primitive variables, ρ, $P_{\rm g}$, $P_{\rm cr}$, v_x, v_y, v_z, B_x, B_y, and B_z. When we solve the fully conservative form of the CR MHD equations, we interpolate the wave amplitudes, w_i, instead of the primitive variables. The interpolated variables are chosen to achieve the second order accuracy in solving the pressure balance mode. The second order accuracy in time is achieved by the two stage Runge-Kutta method. All the test problems are solved on a uniform cell width and with a constant time step.

2.3.1 CR HD Shock Tube Problem

In this subsection, we solve a CR HD shock tube problem with four different schemes. Two of them solve equation (2.11) while the others two not. The initial state is summarized in Table 2.1. The left side has a higher pressure and hence the shock wave runs rightward with the speed, 2.369. The head of the rarefaction wave runs leftward with the speed, -2.160. The spatial resolution is $\Delta x = 1/128$ and the time step is fixed at $\Delta t = 2.0\times10^{-3}$. Accordingly the Courant- Friedrich-Lewy (CFL) number is 0.780 in the simulations shown below.

First we solve the CR HD equations in the fully conservation form, in which the state and flux vectors are given by equations (2.28) and (2.29), with the Roe-type approximate Riemann solver. The solution at $t = 0.1$ is shown in Figure 2.2. The top panels show the density, velocity, and entropy from left to right, respectively. The bottom left panel shows $P_{\rm g}$ by the red curve and $P_{\rm T}$ by the black curve. The bottom central panel denotes $P_{\rm cr}$ by the yellow green while the bottom right panel does CR concentration (χ) by the green. The plus symbols denote the data points. The black curves without symbols denote the Riemann solution, while the dashed lines do the initial state.

The shock front and rarefaction wave are reproduced well in Figure 2.2. The contact discontinuity ($x = 0.156$) is also reproduced well. Note that CR concentration, χ, is

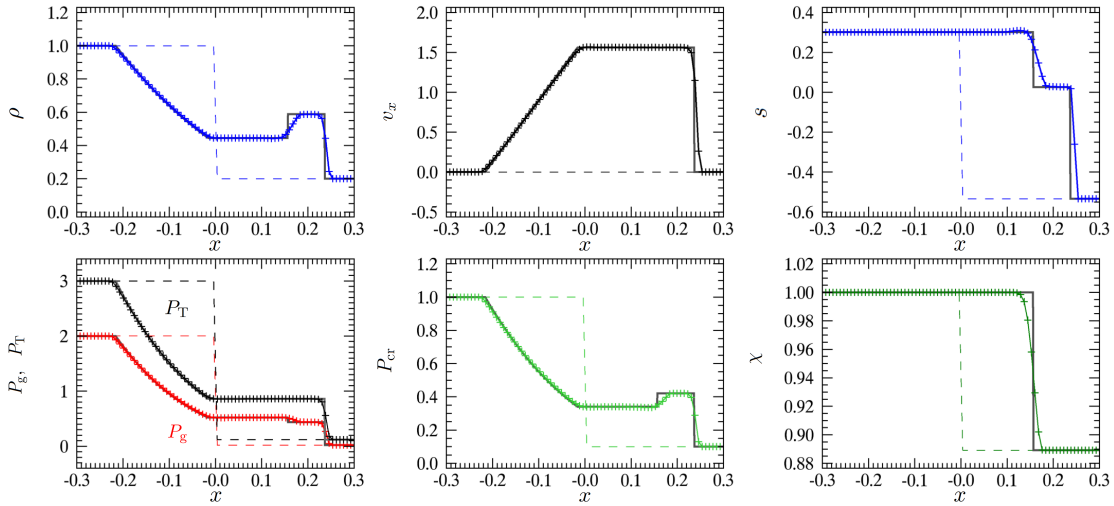

Fig.2.2 The numerical solution of the CR HD shock tube problem compared with the analytic Riemann solution (thin black solid) and the initial state (dashed). The numerical solution (symbols) is of the second order accuracy and obtained with the Roe-type Riemann solver. Top: ρ, v_x and s from left to right. Bottom: $P_{\rm g}$, $P_{\rm T}$, $P_{\rm cr}$ and χ from left to right.

constant across the shock and changes at the contact discontinuity.

Figure 2.3 compares this solution with three other solutions obtained with different schemes. Each panel shows the enlargement around the interval between the shock front and contact discontinuity where the differences are large. The top left and right panels denote $P_{\rm g}$ and s at $t = 0.1$, respectively, while the bottom left and right ones $P_{\rm cr}$ and χ, respectively. The red curves denote the solution shown in Figure 2.2.

The green curves denote the solution obtained with the HLL scheme (see, e.g., Toro (2009)) applied to the fully conservation form of the CR HD equations. The maximum and minimum characteristics are evaluated to be $v_x \pm a$ in the HLL scheme. It provides a good approximation around the shock while the deviation from the Riemann solution is large around the contact discontinuity.

The blue curves denote the solution of equation (2.7). The source term, the right hand side, is evaluated by the central difference. The other equations are solved with the HLL scheme. This scheme is named vdP scheme after the source term. Similar schemes are employed in Kuwabara, Nakamura & Ko (2004). This solution is different from the Riemann solution between the shock front and contact discontinuity. The gas pressure is lower and cosmic ray pressure is higher.

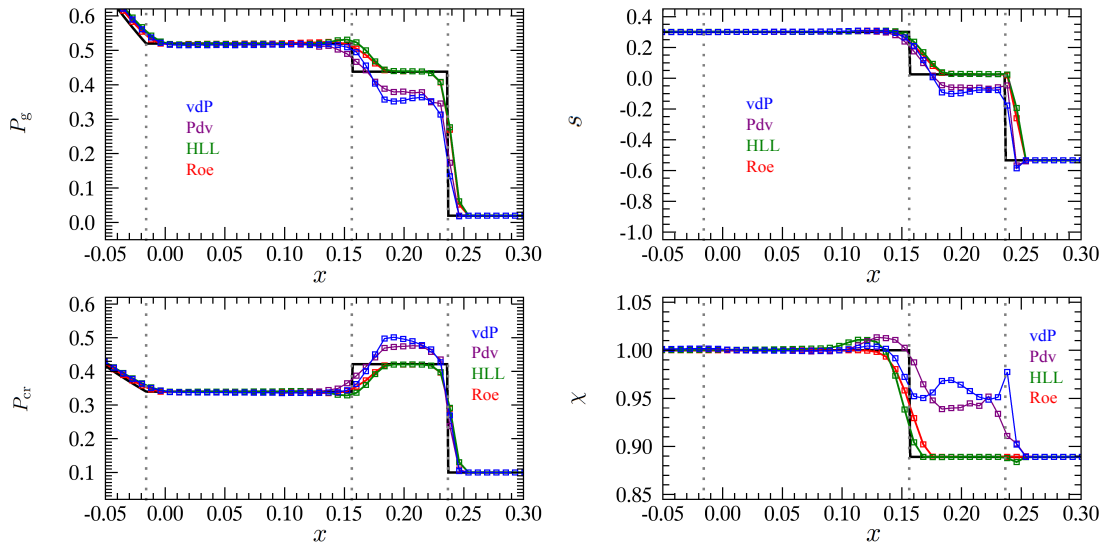

Fig.2.3 Comparison of the numerical solutions with the 2nd order accuracy in the CR HD shock tube problem. The green and red curves denote the solutions obtained with the CR HD equations in the conservation form while the blue and purple curves do those obtained with the equations with source terms. Top: the gas pressure (left) and the entropy (right). Bottom: the CR pressure (left) and the CR concentration (right). See the main text for further details.

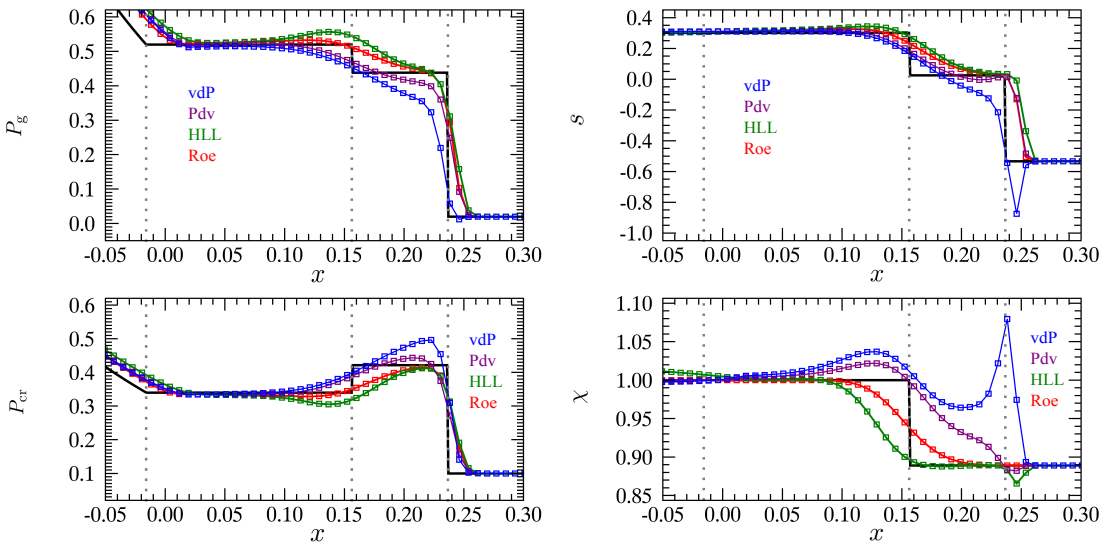

Fig.2.4 The same as Figure 2.3 but for the numerical solution of the 1st order accuracy.

The purple curves denote solution obtained by solving

$$\frac{\partial}{\partial t}\left(E_{\mathrm{cr}}\right)+\boldsymbol{\nabla}\cdot\left(E_{\mathrm{cr}}\boldsymbol{v}\right)=-P_{\mathrm{cr}}\boldsymbol{\nabla}\cdot\boldsymbol{v}, \tag{2.72}$$

which is derived from equation (2.7). The right hand side is evaluated by the central difference and the other equations are solved with the HLL scheme, which we call Pdv scheme in the following. Similar schemes are employed in Hanasz & Lesch (2003), Yang et al. (2012), and Dubois & Commerçon (2016). This solution is also quite different from the Riemann solution between the shock front and contact discontinuity.

When we solve equation (2.7) instead of equation (2.11), we cannot reproduce the Riemann solution. The difference comes in part from the MUSCL approach. Figure 2.3 is the same as Figure 2.4 excepts that the solution is of the first order accuracy in space and time. All the solutions of the first order accuracy are very diffusive around the contact discontinuity as expected.

The Roe-type approximate Riemann solver is, however, still close to the Riemann solution. The HLL scheme produces a hump in P_{g} and a dump in P_{cr} around the contact discontinuity in the first order solution. The hump and dump are much smaller in the second order solution. This implies that they are due to numerical diffusion. We will discuss the origin of the hump and bump in section 3.3. The numerical solutions are still acceptable in the first order accuracy when we solve the fully conservation form.

The solution obtained with the vdP scheme shows serious enhancement in χ at the shock front. The entropy has a dip at the shock front and the shock propagation speed is underestimated. The CR pressure is overestimated while the gas pressure is underestimated. The vdP scheme diffuses the pressure balance mode seriously. This is because the source term diverges at the pressure balance mode in the vdP scheme.

Also the Pdv scheme overestimates the CR pressure and underestimates the gas pressure. However the difference from the Riemann solution is smaller in the solution of the first order accuracy than in that of the second order accuracy. The solution of the second order accuracy depends a little on the choice of variables to be interpolated. However, we could not find any good solution of the second order accuracy when we solve equation (2.11). The source term is extremely large and formally diverges at the shock front in the

Table. 2.2 The initial states in the linear wave propagation tests

	sound	entropy	pressure balance
ρ_0	1.0	1.0	1.0
$P_{\mathrm{g},0}$	1/3	1/3	1/3
$P_{\mathrm{cr},0}$	1/3	1/3	1/3
$v_{x,0}$	0.0	0.5	0.5
ε_ρ (10^{-6})	1.0	1.0	0.0
ε_{g} (10^{-6})	$\gamma_{\mathrm{g}}/3$	0.0	-1.0
$\varepsilon_{\mathrm{cr}}$ (10^{-6})	$\gamma_{\mathrm{cr}}/3$	0.0	1.0
ε_v (10^{-6})	1.0	0.0	0.0

Pdv scheme. Accordingly the Rankine-Hugoniot relation is not satisfied. The numerical solution around the shock is not improved by the MUSCL approach.

2.3.2 Linear Wave Test

We examine the propagation of 1D plane waves of a small amplitude in order to confirm the accuracy of our scheme. In the following we follow a sound wave, entropy wave, and the pressure balance mode. The initial state at $t = 0$ is taken to be

$$\rho = \rho_0 + \varepsilon_\rho \cos\left(\frac{2\pi x}{\lambda}\right), \tag{2.73}$$

$$P_{\mathrm{g}} = P_{\mathrm{g},0} + \varepsilon_{\mathrm{g}} \cos\left(\frac{2\pi x}{\lambda}\right), \tag{2.74}$$

$$P_{\mathrm{cr}} = P_{\mathrm{cr},0} + \varepsilon_{\mathrm{cr}} \cos\left(\frac{2\pi x}{\lambda}\right), \tag{2.75}$$

$$v_x = v_{x,0} + \varepsilon_v \cos\left(\frac{2\pi x}{\lambda}\right), \tag{2.76}$$

where λ denotes the wavelength. The other parameters are summarized in Table 2.2. Note that the sound speed is set to be $a = 1.0$ in all the models. The time step is taken to be $\Delta t = 0.5\Delta x/a$. The size of the computation box is the same as the wavelength and the periodic boundary condition is applied.

We measure the numerical error at the epoch at which the wave propagates by a wave-

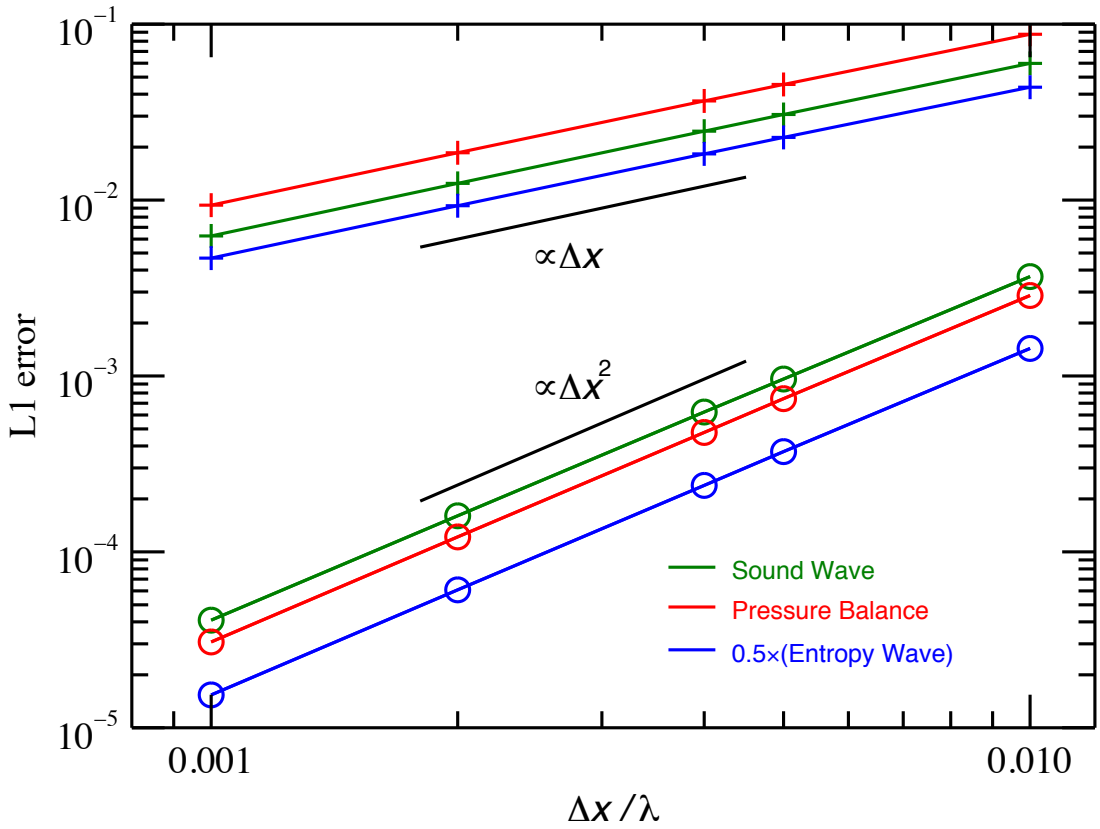

Fig.2.5 The L1 norm of the numerical error is shown as a function of the cell width in unit of the wavelength. The crosses denote the errors in the solution of the first order accuracy, while the circles denote those of the second order accuracy. The green, blue and red symbols are for the sound wave, pressure balance mode, and the entropy wave, respectively.

length, i.e., $t = \lambda/a$ for the sound wave and $t = \lambda/v_0$ for the other waves. We use the L1 norm defined as

$$\delta q(t) = \frac{1}{N\varepsilon_q} \sum_j \left| q_{\rm numerical}(x_j, t) - q_{\rm exact}(x_j, t) \right| , \tag{2.77}$$

where the symbol, q, denotes a physical quantity. The numerical and exact solutions are denoted by $q_{\rm numerical}(x_j, t)$ and $q_{\rm exact}(x_j, t)$, respectively. The symbols, N and ε_q, denote the number of cell in a wavelength and the wave amplitude in the variable, q.

Figure 2.5 denote $\delta\rho(\lambda/a)$ in the sound wave as a function of $\Delta/x\lambda \equiv 1/N$ by the green crosses and circles, the former and latter of which are obtained with the first and second order schemes, respectively. The red crosses and circles are the same as the green ones but

for $\delta P_{\rm cr}\,(\lambda/v_{x,0})$ in the pressure balance mode. We denote the error in the entropy mode, $\delta\rho\,(\lambda/v_{x,0})\,/2$, by the blue crosses and circles. The factor, 1/2, is introduced to avoid the overlap with the red symbols. Our second order schemes solve all these hydrodynamical waves with the second order accuracy in space.

Also the Pdv and vdP scheme provide the solutions of the second order accuracy for the test problems examined in this subsection. As far as the wave amplitude is small, all the schemes provide nearly the same results as expected.

2.3.3 Advection of the Pressure Balance Mode

The pressure balance mode produces some unphysical features such as spurious enhancement in the gas pressure and dent in the CR pressure as shown in Figure 2.4. It also emit spurious sound waves as shown later in this subsection. We identify the origin and provide a remedy. The initial state of the test problem is summarized in Table 2.3. The velocity should remain constant in this problem since the total pressure has the same value in the both sides. The cell width and time step are taken to be $\Delta x = 0.1$ and $\Delta t = 0.025$, respectively. Accordingly the CFL number is 0.585 in the simulations shown below.

The spurious sound wave appears from the beginning irrespectively of the numerical scheme applied. Figure 2.6 shows the solutions at the first three time steps, i.e., at $t = 0.000$, 0.025, and 0.050 from top to bottom. The left and central panels show $P_{\rm g}$ and $P_{\rm T}$, respectively, while the right panels show v_x. The green and red curves with the symbols denote the solutions obtained with the HLL scheme and the Roe-type Riemann solver, respectively, while the black lines denote the exact solution. The accuracy of these solutions are the first order in space and in time. The total pressure is enhanced at the second time step ($t = 0.025$) and the velocity perturbation appears at the the third time step ($t = 0.050$).

Figure 2.7 is the same as Figure 2.6 but for the solutions of the second order accuracy. The velocity perturbation appears from the first step, $t = 0.025$. The amplitude of the perturbation is nearly the same as that in the solutions of the first order accuracy. As shown later, the perturbation can suppressed if the initial state is slightly modified.

Figure 2.8 shows the later stages of the solutions obtained with the first order Roe

Table. 2.3 The initial state in the test problem of the advection of pressure balance mode.

	ρ	v_x	$P_{\rm g}$	$P_{\rm cr}$
left ($x < 0$)	1.0	1.0	0.1	1.0
right ($x \geq 0$)	1.0	1.0	1.0	0.1

scheme. The top, middle and bottom panels show the density, the total pressure and the velocity, respectively. The color denotes the epoch. The velocity perturbation observed in Figure 2.6 evolves into sound waves propagating rightward and leftward of which phase velocity are $v_x + a = 2.342$ and $v_x - a = -0.225$ for the former and latter, respectively. In addition to the sound waves, the density profile has a dent around the contact discontinuity. The dent grows in depth and in width. We need to suppress the sound waves of the numerical origin and growth of the dent.

This artificial wave excitation is due to the numerical diffusion of CR numbers. If we take account of numerical diffusion, equation (2.11) is rewritten as

$$\frac{\partial}{\partial t}\rho_{\rm cr} + \boldsymbol{\nabla}\cdot(\rho_{\rm cr}\boldsymbol{v}) = \boldsymbol{\nabla}\cdot(\eta\boldsymbol{\nabla}\rho_{\rm cr}), \tag{2.78}$$

where η denotes the effective diffusion coefficient. Hence equation (2.7) is rewritten as

$$\begin{aligned}\frac{\partial}{\partial t}(E_{\rm cr}) + \boldsymbol{\nabla}\cdot[(E_{\rm cr}+P_{\rm cr})\,\boldsymbol{v} - \eta\boldsymbol{\nabla}(E_{\rm cr})] \\ = \boldsymbol{v}\cdot\boldsymbol{\nabla}P_{\rm cr} - \frac{\eta}{\gamma_{\rm cr}P_{\rm cr}}\left|\boldsymbol{\nabla}P_{\rm cr}\right|^2,\end{aligned} \tag{2.79}$$

where the second term in the right hand side denotes the net loss in the CR energy. Figure 2.9 illustrates this mechanism of the loss in the CR energy

The loss in the CR energy is compensated by the gain in the gas energy, since the total energy is conserved. We can evaluate the change in the total pressure as follows. Given the CR pressure decrease by $\Delta P_{\rm cr}$, the CR energy decreases by

$$\Delta E_{\rm cr} = \frac{\Delta P_{\rm cr}}{\gamma_{\rm cr}-1}, \tag{2.80}$$

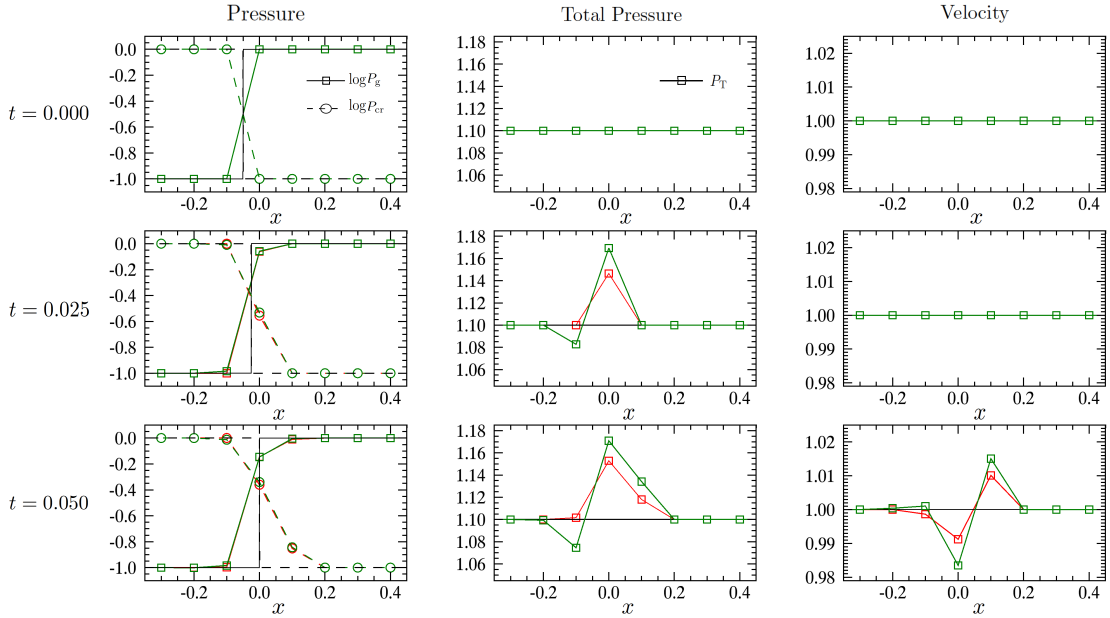

Fig.2.6 Test for the advection of the pressure balance mode. The top panels denote the gas pressure, the CR pressure, the total pressure and the velocity in the initial state from left to right. The middle and bottom panels denote those at the first time step, $t = \Delta t$ and at the second time step, $t = 2\Delta t$, respectively. The green and red curves denote the solutions obtained with HLL and Roe-type numerical fluxes, respectively. The black line denotes the exact solution.

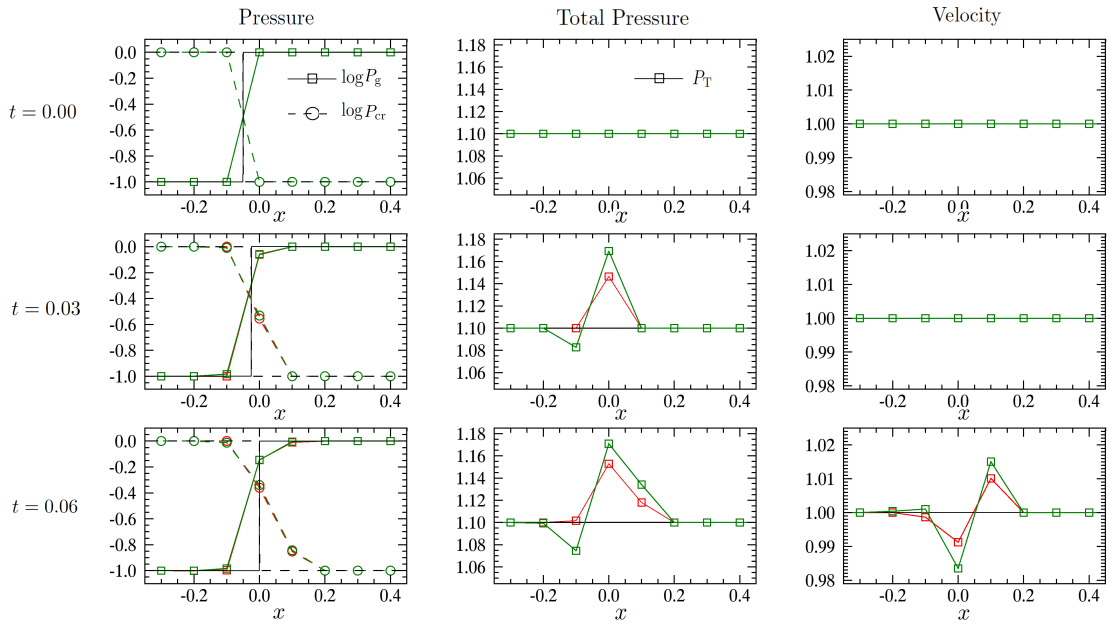

Fig.2.7 The same as Figure 2.6 but for the 2nd order accuracy.

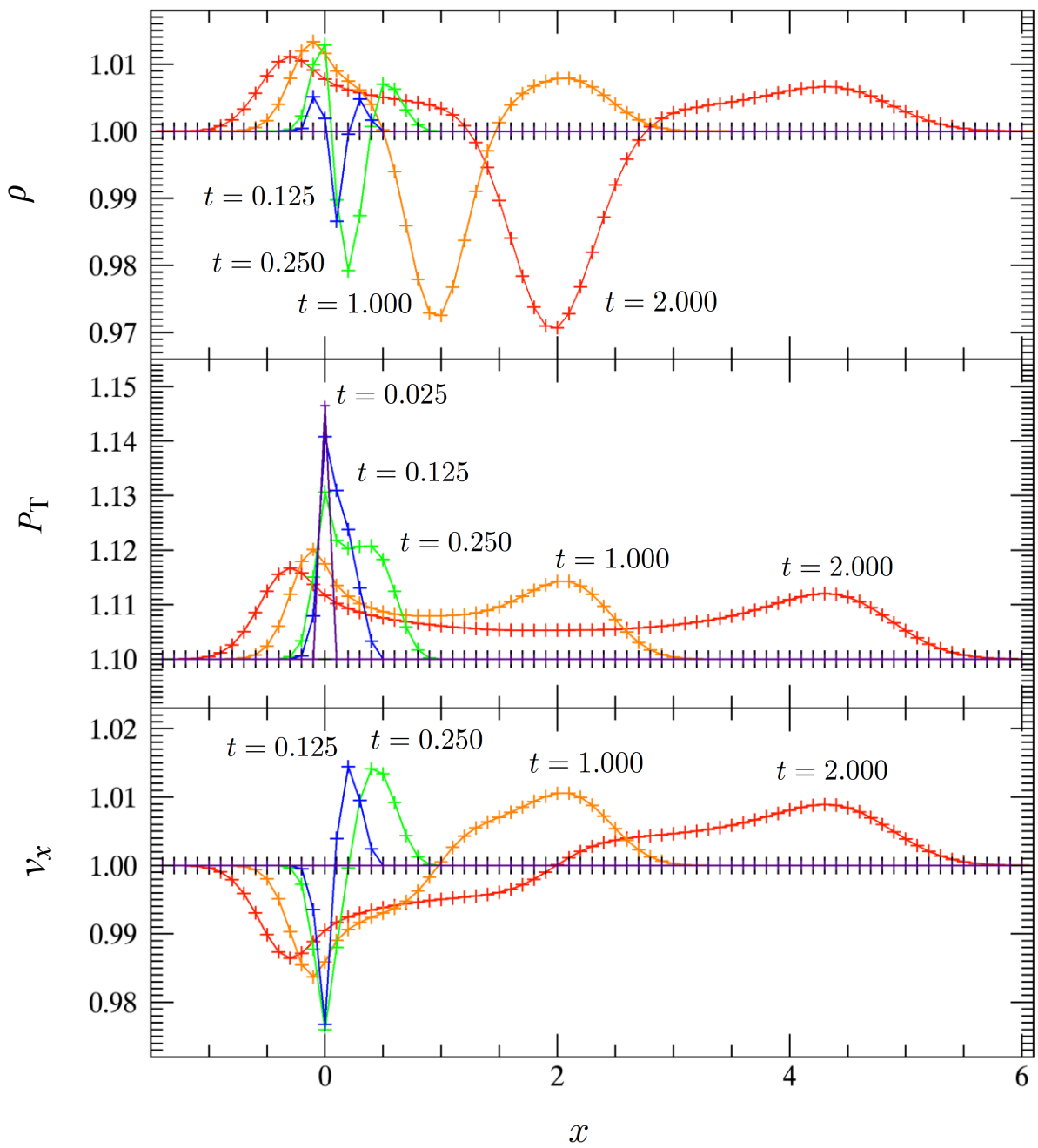

Fig.2.8 Late stages of the test problem shown in Fig. 6 The panels denote ρ, P_{T}, and v_x fro the top to the bottom. The symbols and curves denote the the solution at $t = 0.025$, 0.125, 0.250, 1.0, and 2.0.

and the gas energy increases by the same amount. Hence the gas pressure increases by

$$\Delta P_{\mathrm{g}} = -\left(\gamma_{\mathrm{g}} - 1\right) \Delta E_{\mathrm{cr}} = -\frac{\gamma_{\mathrm{g}} - 1}{\gamma_{\mathrm{cr}} - 1} \Delta P_{\mathrm{cr}}. \tag{2.81}$$

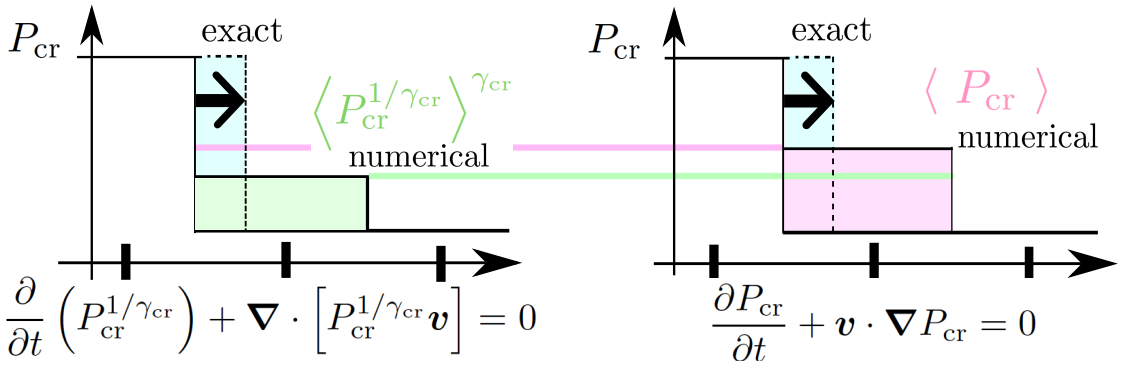

Fig.2.9 Illustration of the mechanism for the decrease in $P_{\rm cr}$ due to numerical diffusion by advection of the pressure balance mode. The left panel denotes the numerical solution of the CR number conservation, while the right does that of the advection equation.

Then the total pressure increases by

$$\Delta P_{\rm T} = \frac{\gamma_{\rm cr} - \gamma_{\rm g}}{\gamma_{\rm cr} - 1} \Delta P_{\rm cr}, \tag{2.82}$$

since $\gamma_{\rm cr} < \gamma_{\rm g}$ and $\Delta P_{\rm cr} < 0$.

The emission of the sound waves result in the decrease in the density. Thus, also the dent is due to the numerical diffusion of the CR pressure.

Although the numerical diffusion is inevitable, the effects can be alleviated by modifying the initial transition less sharp. If the initial profile is modified to be

$$q(x) = \frac{q_{\rm R} + q_{\rm L}}{2} + \frac{q_{\rm R} - q_{\rm L}}{2} \tanh\left(\frac{x}{h}\right), \tag{2.83}$$

where q and h denote a physical variable and the thickness of the transition layer, respectively. The subscripts, R and L, denote the values at the right and left states, respectively. Figure 2.10 shows the effects of the modified initial profile. All the curves denote the solutions of the advection test at $t = 2.000$. The red and orange curves denote the solutions of which initial profile is given by equation (2.83) with $h = \Delta x = 0.1$. The red solution is obtained with the second order Roe scheme, while the orange is with the first order Roe scheme. The black and grey curves denote the solutions of which initial state is denoted by a step function ($h = 0$). The black and grey solutions are obtained with the second and first order Roe schemes, respectively. Adoption of a second order scheme alone cannot

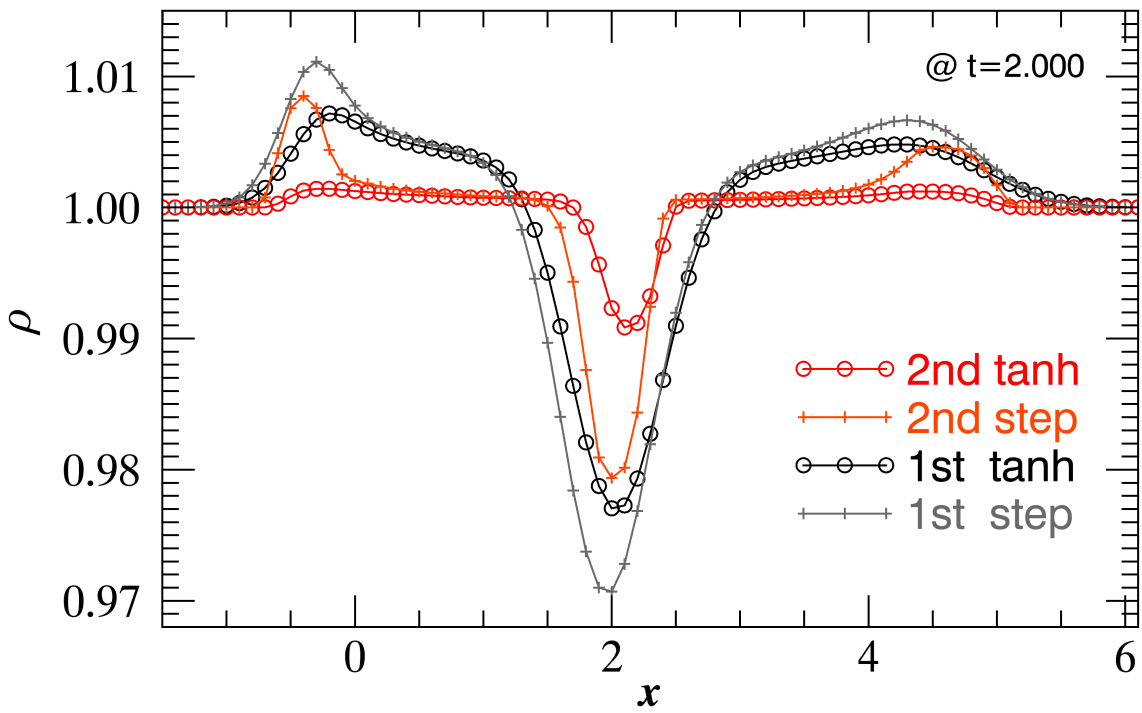

Fig.2.10 Compared are the numerical solutions of the advection test problem at $t = 2.0$. The initial state is expressed by equation (78) in the solutions denoted by red and black, while it is by the step function in the solutions denoted by orange and grey. The red and orange curves denote the solutions of the second order accuracy, while the black and grey do those of the first order accuracy. All the solutions are obtained with the Roe-type Riemann solver.

suppress the numerical diffusion effectively. Only when $h \gtrsim \Delta x$, the numerical diffusion is suppressed sufficiently.

The Pdv scheme does not produce the spurious wave, since the source term vanishes in this test problem. The vdP scheme suffers from the spurious wave since the source term diverge at the front of the pressure balance mode. We have not tried to improve the vdP scheme to suppress the spurious wave excitation, since the vdP scheme can not solve a shock wave properly.

We encounter a similar problem when solving the advection of the tangential shear. The shear velocity is smeared by numerical diffusion and hence a part of the kinetic energy is lost. The loss is compensated by the increase in the internal energy and hence the gas pressure increases spuriously around the shear. This problem is also alleviated by the same recipe.

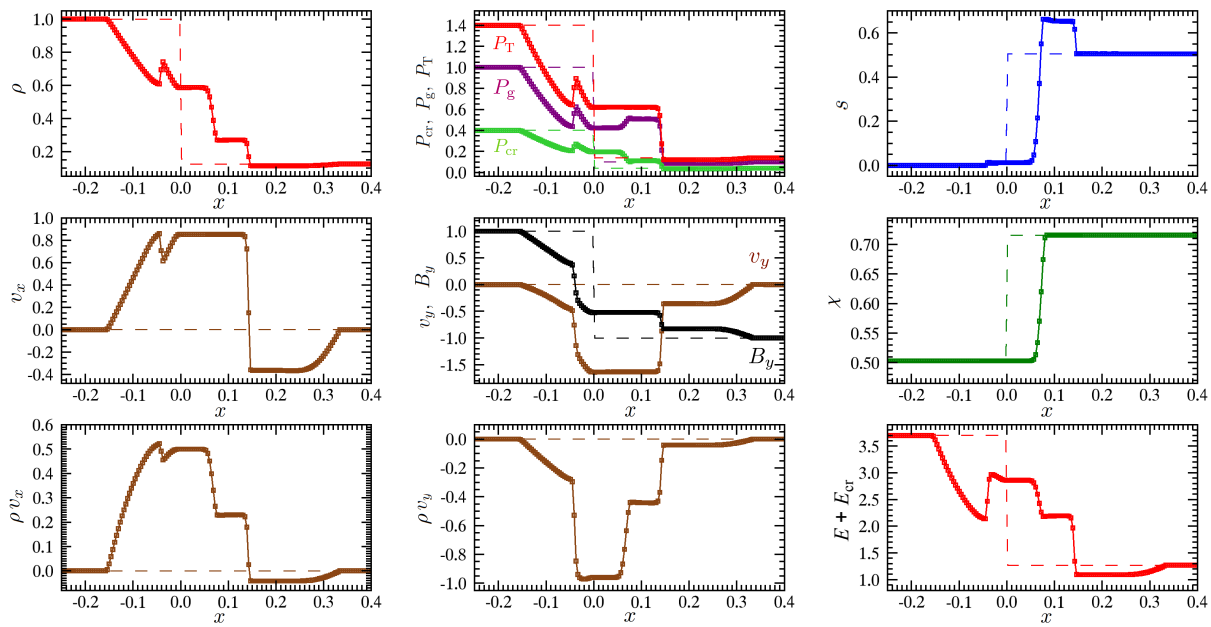

Fig.2.11 An example of CR MHD shock tube problem. Top: the density, CR pressure, gas pressure, total pressure, and entropy from left to right. Middle: the velocity, magnetic field, and CR concentration from left to right. Bottom: the x- and y-components of the momentum density, and the total energy density from left to right.

2.3.4 1D MHD Shock Tube Test

In this subsection we demonstrate that the 1D MHD shock tube problem can be solved with the Roe-type approximate Riemann solver. The initial state of the problem is summarized in Table 2.4. This problem is similar to the well-known one tested by Brio & Wu (1988). The resolution, the time step, and CFL number are taken to be $\Delta x = 1/256$, $\Delta t = 8 \times 10^{-4}$, and 0.843, respectively.

Figure 2.11 shows the numerical solution at $t = 0.08$. The left panels denote ρ, v_x, and ρv_x, respectively. The solid curves with the open squares denote the numerical solution while the dashed ones do the initial state. The top central panel denote $P_{\rm T}$ (red), $P_{\rm g}$ (purple), and $P_{\rm cr}$ (yellow green), while the middle central one does v_y (brown) and B_y (black) and the bottom central one dose ρv_y. The right panels denote s, χ, and $E + E_{\rm cr}$, respectively.

The solution shows the fast rarefaction wave, the slow shock, the contact discontinuity (the pressure balance mode), the slow compound, and the fast rarefaction, from right

Table. 2.4 Initial left- and right-state in the shock tube problem of modified Brio & Wu (1988).

	ρ	B_x	B_y	B_z	$P_{\rm g}$	$P_{\rm cr}$
Left ($x < 0$)	1.0	1.0	1.0	0.0	1.0	0.4
Right ($x \geq 0$)	0.125	1.0	-1.0	0.0	0.1	0.04

Table. 2.5 Initial inside- and outside-state in the 2D MHD expansion.

	ρ	B_r	B_φ	B_z	$P_{\rm g}$	$P_{\rm cr}$
Inside	1.0	0.0	0.0	0.4472	2.0	1.0
Outside	0.2	0.0	0.0	0.4472	0.02	0.1

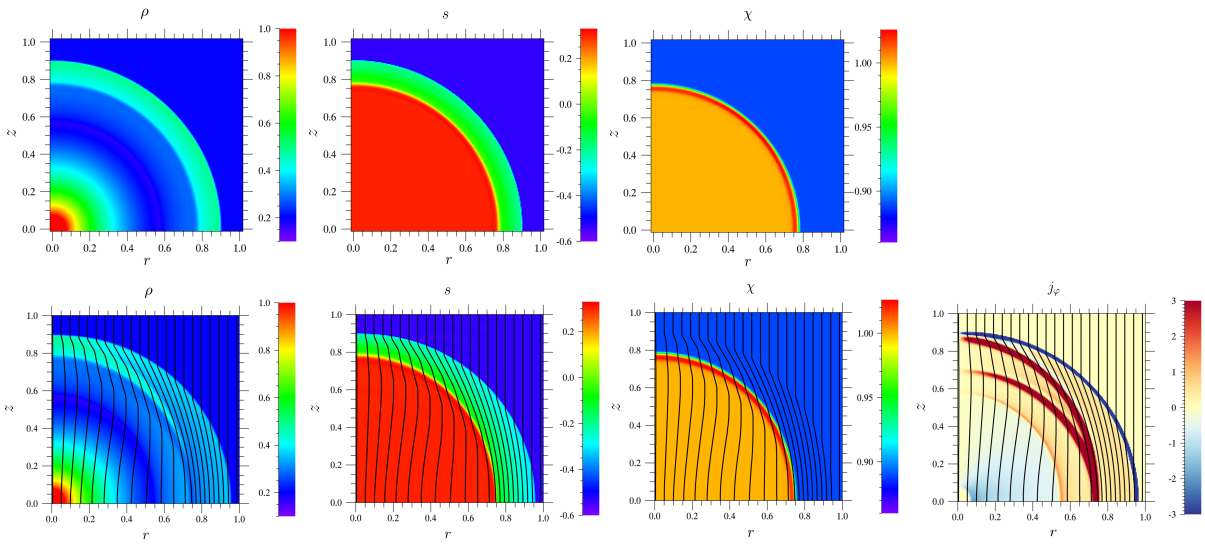

Fig.2.12 Expansion of a high pressure sphere. Top: the density, entropy, and CR concentration in HD expansion problem from left to right. Bottom: the density, entropy, CR concentration, and electric current density in MHD problem. The initial states are the same except for the initial magnetic field. The black curves denote the magnetic field in the bottom panels.

to left. Note that the contact discontinuity and the pressure balance mode are solved sharply. The CR concentration, χ, changes only at the contact discontinuity.

2.3.5 2D MHD Expansion

In this subsection we consider an expansion of a hot sphere. We use the cylindrical coordinates, (r, φ, z), and assume the symmetry around the z-axis. The gas pressure is higher inside the sphere of $\sqrt{r^2 + z^2} = 0.5$ in the initial state. It is assumed to have the

profile,

$$P_{\rm g}(r,z) = P_{\rm g,in} + \frac{(P_{\rm g,out} - P_{\rm g,in})}{2} \times \left[\tanh\left(\frac{\sqrt{r^2+z^2}-0.5}{0.01}\right)+1\right], \tag{2.84}$$

where the subscripts, in and out, denote the values inside and outside the sphere, $\sqrt{r^2+z^2} = 0.5$. Also the CR pressure and density are assumed to have similar profiles. The parameters are summarized in Table 2.5. The velocity is assumed to vanish in the initial state. The spatial resolution, time step, and CFL number are taken to be $\Delta x = \Delta z = 1/200$, $\Delta t = 5 \times 10^{-4}$, and 0.340 respectively.

We construct two models having the same initial ρ, $P_{\rm g}$, and $P_{\rm cr}$. The magnetic field vanishes in the first model while it is uniform and has only the z-component in the second model. The plasma beta is $\beta = 20$ inside and 2 outside the sphere in the second model. We solved this model with the Roe-type approximate Riemann solver.

Figure 2.12 denotes the stage at $t = 0.19$. The top panels denote ρ, s, and χ in the first model from left to right. The values are shown by color and the color bars are shown in the right of each panel. They show spherical shock wave propagating outward and rarefaction propagating inward. The contact discontinuity and pressure balance mode are clearly resolved.

The bottom panels denote ρ, s, χ, and the electric current density, j_φ. The color denote the values while the black contours do the magnetic field lines. The expansion is aspherical due to the magnetic field. The model shows three shock waves: a fast shock wave and two slow shock waves. The magnetic field is bent sharply at the shock fronts. Note that the electric current density is confined at the shock fronts and in the rarefaction wave. This example demonstrates that the multi-dimensional CR MHD equations can be solved successfully if we employ the fully conservation form.

Chapter 3

Magneto Cosmic Ray Instability

3.1 Introduction of Magnetic Buoyancy Instability

Parker (1966) pointed out that the growth rate of Parker instability is enhanced by CRs when the cosmic ray pressure becomes uniform along magnetic field lines. He showed that when the gravity is uniform and $\alpha = P_{\rm B}/P_{\rm g}$, $\beta = P_{\rm cr}/P_{\rm g}$ and sound speed $a = (\gamma_{\rm g} P_{\rm g}/\rho)^{1/2}$ are constant, the instability grows for long wavelength perturbations along the magnetic field line when

$$(Hk_x)^2 < \frac{(1+\alpha+\beta)\,(1+\alpha+\beta-\gamma_{\rm g})}{2\alpha\gamma_{\rm g}} - \frac{1}{4} \tag{3.1}$$

where $H = (1+\alpha+\beta)a^2/(\gamma_{\rm g} g)$ is the pressure scale height and g is gravity. Parker instability with CRs under the non-uniform gravity was investigated by Kim, Hong & Ryu (1997). Kim & Hong (1998) studied the dependence of the growth rate on α, β and $\gamma_{\rm g}$ assuming $\boldsymbol{B} \cdot \nabla P_{\rm cr} = 0$, which means that CR pressure is uniform along the magnetic filed lines.

Ryu et al. (2003) studied the CR diffusion effects by linear stability analysis using the CR equation (1.43) assuming uniform gravity. They showed that the maximum wave number for the instability changes between models with CR diffusion along magnetic field

lines and those without CR diffusion (i.e., $\kappa_{\parallel} = 0$) as

$$H^2 k_x^2 < \begin{cases} \dfrac{(1+\alpha+\beta)(1+\alpha+\beta-\gamma_{\rm g})}{2\alpha\gamma_{\rm g}} - \dfrac{1}{4} & \text{for } \kappa_{\parallel} > 0 \\ \dfrac{(1+\alpha+\beta)(1+\alpha+\beta-\gamma_{\rm g}-\gamma_{\rm cr}\beta)}{2\alpha(\gamma_{\rm g}+\gamma_{\rm cr}\beta)} - \dfrac{1}{4} & \text{for } \kappa_{\parallel} = 0. \end{cases} \tag{3.2}$$

Note that the criterion for $\kappa_{\parallel} > 0$ coincides with that for $\kappa_{\parallel} \to \infty$ in equation (3.1). Equation (3.2) indicates that the CR pressure without CR diffusion has stabilizing effect on the Parker instability. When $\gamma_{\rm g} = 1$, $\gamma_{\rm cr} = 4/3$, $\beta = 1$, and $\kappa_{\parallel} = 0$, the instability disappears when $\alpha \lesssim 0.6$. Ryu et al. (2003) also showed that the perpendicular diffusion $\kappa_{\perp} = 0.02\kappa_{\parallel}$ does not contribute to the growth of the instability. Linear and Nonlinear studies of the CR Parker instability for non-uniform gravity were performed by Kuwabara, Nakamura & Ko (2004). They showed by linear analysis that CR pressure increases the growth rate when CR diffusion is taken into account. But they did not study models with weak magnetic field.

Numerical studies of magnetic buoyancy instability including CR effects were carried out by Hanasz & Lesch (2000, 2003). They simulated three-dimensional growth of the Parker instability induced by CRs injected by supernova. Kuwabara, Nakamura & Ko (2004) carried out two-dimensional simulations, assuming equatorial symmetry. They showed that the dependence of numerical results on the CR diffusion agree with the results of linear analysis. Rodrigues et al. (2016) studied the dependence on the pressure ratio and magnetic Prandtl number by three-dimensional simulations assuming the same symmetry as Kuwabara, Nakamura & Ko (2004). Their simulations assumed that magnetic pressure dominates the CR pressure ($\alpha > \beta$).

In this chapter, we present the results of linear and non-linear analysis of the CR MHD when the magnetic field is weak ($\alpha \leq 1$ and $\alpha \leq \beta$). We present the equilibrium model and assumptions in Section 3.2. The linear analysis of the magnetic buoyancy instability including CRs are shown in Section 3.3. In section 3.4, we present results of numerical simulations obtained by applying the new scheme described in Chapter 2.

3.2 Models and initial conditions

3.2.1 Gravitational field, cosmic ray diffusion, and normalizations

We adopt the local cylindrical coordinate $(x, y, z) = (\phi, -r, z)$, and assume that radial gravity balances with the centrifugal force.

Vertical gravitational field is modeled by the anti-symmetric function of z,

$$g_z(z) = g \tanh\left(\frac{z}{0.5[\mathrm{kpc}]}\right), \tag{3.3}$$

where the maximum gravity is $g = 5.0 \times 10^{-9}$ cm s^{-2}. For simplicity, the effects of disk rotation and self-gravity from the gas are neglected. The gravitational field given by equation (3.3) is similar to the realistic gravitational field around the solar neighborhood at galactic radius $r \sim 8$kpc and $|z| < 5$ kpc. The magnetic buoyancy instability depends on the magnitude of gravitational field $|g_z|$ and sign of the gradient dg_z/dz (see, Giz & Shu 1993; Kim & Hong 1998).

Galactic CRs are taken into account by CR pressure $P_{\mathrm{cr}}(\boldsymbol{x}, t)$. CR specific heat ratio is assumed to be approximately constant, $\gamma_{\mathrm{cr}} = 4/3$, and CR diffusion coefficient along the magnetic field is assumed to be constant, $\kappa_{\parallel} = 6.172 \times 10^{28}$ cm^2 s^{-1}. Strong & Moskalenko (1998) showed that this value can explain the CRs energy spectrum at solar neighborhood. On the other hand, CR perpendicular diffusion can be ignored (e.g. Ryu et al. 2003), because the typical time scale of Parker instability, $H_0/v_A \sim 30$ [Myr] (Parker 1979, P355) is an order of magnitude smaller than the timescale of perpendicular diffusion evaluated as,

$$\tau_{\perp} = 176.8 \text{ Myr} \left[\frac{\kappa_{\perp}}{6.172 \times 10^{26}[\mathrm{cm^2 s^{-1}}]}\right]^{-1} \left[\frac{L}{100 \text{ [pc]}}\right]^2, \tag{3.4}$$

Here we adopted $\kappa_{\perp} = 0.01\kappa_{\parallel}$ and typical length $L = 100$ pc.

We normalized the physical quantities as summarized in Table 3.1

Table. 3.1 Normalization unit. $k_{\rm B}$ is the Boltzmann constant, and m is the mass of Hydrogen.

Quantity	Unit	Normalization value
Length	H_0	3.086×10^{20} cm
Velocity	v_0	1.000×10^{6} cm s^{-1}
Time	H_0/v_0	3.086×10^{14} s
Density	ρ_0	1.600×10^{-24} g cm^{-3}
Pressure	$\rho_0 v_0^2$	1.600×10^{-12} dyn cm^{-2}
Magnatic Field	$\sqrt{\rho_0 v_0^2}$	1.265 μG
Temperature	$v_0^2/(\gamma_{\rm g} k_{\rm B}/m)$	1.211×10^{4} K
Diffusion Coefficient	$H_0 v_0$	3.086×10^{26} cm^2 s^{-1}

3.2.2 Equilibrium state

The equilibrium state is assumed to be in magnetohydrostatic equilibrium in z-direction,

$$\frac{d}{dz}\left(P_{\rm g0} + P_{\rm cr0} + \frac{B_0^2}{2}\right) = -\rho_0 g_z(z) \ . \tag{3.5}$$

Here, the initial magnetic field is assumed to be parallel to the equatorial plane, $\boldsymbol{B} = (B_0, 0, 0)$, and the subscript 0 denotes the unperturbed state. We assume that the initial pressure ratio α and β are spatially constant.

We adopted the two layer model (Shibata et al. 1989) for the initial temperature,

$$T_z(z) = T_0 + (T_{\rm halo} - T_0)\frac{1}{2}\left[\tanh\left(\frac{|z| - z_{\rm halo}}{w_{\rm tr}}\right)\right] \ , \tag{3.6}$$

where the disk temperature is $T_0 = 1$, $T_{\rm halo} = 25T_0$ is the Coronal temperature, $z_{\rm halo} = 10$ is the height of the disk-halo interface, $w_{\rm tr} = 0.5$ is the width of the transition layer.

3.3 Linear Analysis

We linearize the CR MHD equations (2.1), (2.2), (2.3) and (2.7) by assuming that perturbed quantities are proportioned to $\exp(ik_x x + ik_y y + \sigma t)$. Here, k_x and k_y are the wave numbers in the x- and y-directions, and σ is the growth rate, respectively. The

linearized perturbation equations for adiabatic plasma are given by,

$$\sigma\delta\rho = -\rho_0\left(i\boldsymbol{k}\cdot\delta\boldsymbol{v} + \frac{d}{dz}\delta v_z\right) - \delta v_z\frac{d\rho_0}{dz}, \tag{3.7}$$

$$\sigma\rho_0\delta v_x = -ik_x\delta P_{\mathrm{T}} + ik_xB_0\delta B_x + \delta B_z\frac{dB_0}{dz}, \tag{3.8}$$

$$\sigma\rho_0\delta v_y = -ik_y\delta P_{\mathrm{T}} + ik_xB_0\delta B_y, \tag{3.9}$$

$$\sigma\rho_0\delta v_z = -\frac{d}{dz}\delta P_{\mathrm{T}} + ik_xB_0\delta B_z - \delta\rho g_z \tag{3.10}$$

$$\sigma\delta B_x = ik_xB_0\delta v_x - B_0\left(i\boldsymbol{k}\cdot\delta\boldsymbol{v} + \frac{d}{dz}\delta v_z\right) - \delta v_z\frac{dB_0}{dz}, \tag{3.11}$$

$$\sigma\delta B_y = ik_xB_0\delta v_y, \tag{3.12}$$

$$\sigma\delta B_z = ik_xB_0\delta v_z, \tag{3.13}$$

$$\sigma\delta P_{\mathrm{g}} = -T_z\rho_0\left(i\boldsymbol{k}\cdot\delta\boldsymbol{v} + \frac{d}{dz}\delta v_z\right) - \delta v_z\frac{dP_{g0}}{dz}, \tag{3.14}$$

$$\sigma\delta P_{\mathrm{cr}} = -\gamma_{\mathrm{cr}}P_{\mathrm{cr0}}\left(i\boldsymbol{k}\cdot\delta\boldsymbol{v} + \frac{d}{dz}\delta v_z\right) - \delta v_z\frac{dP_{\mathrm{cr0}}}{dz} + \kappa_{\parallel}\left(ik_x\frac{\delta B_z}{B_0}\frac{dP_{\mathrm{cr0}}}{dz} - k_x^2\delta P_{\mathrm{cr}}\right), \tag{3.15}$$

where $\boldsymbol{k} = (k_x, k_y, 0)$ is the wave number vector, $\delta P_{\mathrm{T}} = \delta P_{\mathrm{g}} + \delta P_{\mathrm{cr}} + B_0\delta B_x$ is the perturbed total pressure, $T_z = \gamma_{\mathrm{g}}P_0/\rho_0$ is the normalized temperature, respectively. After some algebra, linearized equations (3.7)-(3.15) are expressed as the simultaneous differen-

Table. 3.2 Wave number when the growth rate is largest

Parameter	Wave number k_x	Growth rate σ
$\alpha = 1.0,\ \beta = 0$	0.260	0.16812
$\alpha = 0.1,\ \beta = 0$	0.198	0.03307
$\alpha = 1.0,\ \beta = 1$	0.333	0.26300
$\alpha = 0.1,\ \beta = 1$	0.984	0.54175

tial equation,

$$\frac{d}{dz}\begin{bmatrix} y_1 \\ y_2 \end{bmatrix} = \begin{bmatrix} A_{11} & A_{12} \\ A_{21} & A_{22} \end{bmatrix}\begin{bmatrix} y_1 \\ y_2 \end{bmatrix}, \tag{3.16}$$

where

$$y_1 \equiv \rho_0 \delta v_z, \quad y_2 \equiv \sigma \delta P_{\mathrm{T}}, \tag{3.17}$$

$$A_{11} = -\frac{\gamma_g}{1+\alpha+\beta}\frac{g_z}{T_z} - \frac{d\ln T_z}{dz} + \frac{\sigma^2}{\Xi\Sigma^2}\frac{g_z}{T_z}, \tag{3.18}$$

$$A_{12} = -\frac{k_x^2 + k_y^2}{\Sigma^2} - \frac{1}{\Xi T_z}\left(\frac{\sigma^2}{\Sigma^2}\right)^2, \tag{3.19}$$

$$A_{21} = -\Sigma^2 + g_z\left(\frac{g_z}{\Xi T_z} - \frac{\gamma_g}{1+\alpha+\beta}\frac{g_z}{T_z} - \frac{d\ln T_z}{dz}\right), \tag{3.20}$$

$$A_{22} = -\frac{g_z}{\Xi T_z}\frac{\sigma^2}{\Sigma^2}, \tag{3.21}$$

$$\Sigma^2 = \sigma^2 + 2\frac{\alpha}{\gamma_{\mathrm{g}}} T_z {k_x}^2, \quad K_{\parallel} = \kappa_{\parallel}\frac{{k_x}^2}{\sigma}, \quad \Xi = 1 + \frac{\gamma_{\mathrm{cr}}}{\gamma_{\mathrm{g}}}\frac{\beta}{1+K_{\parallel}} + 2\frac{\alpha}{\gamma_{\mathrm{g}}}\frac{\sigma^2}{\Sigma^2}. \tag{3.22}$$

For a given parameter α and β and the boundary condition, we obtain the solutions of equation (3.16) by seeking the eigenmodes which satisfy the boundary conditions at $z = 0$ and $z = z_{\max}$.

3.3.1 Dispersion relation

The growth rates of the fundamental mode in which ρv_z is symmetric to the equatorial plane ($z = 0$) are shown in Fig. 3.1. We founded that when the magnetic field is weak, the

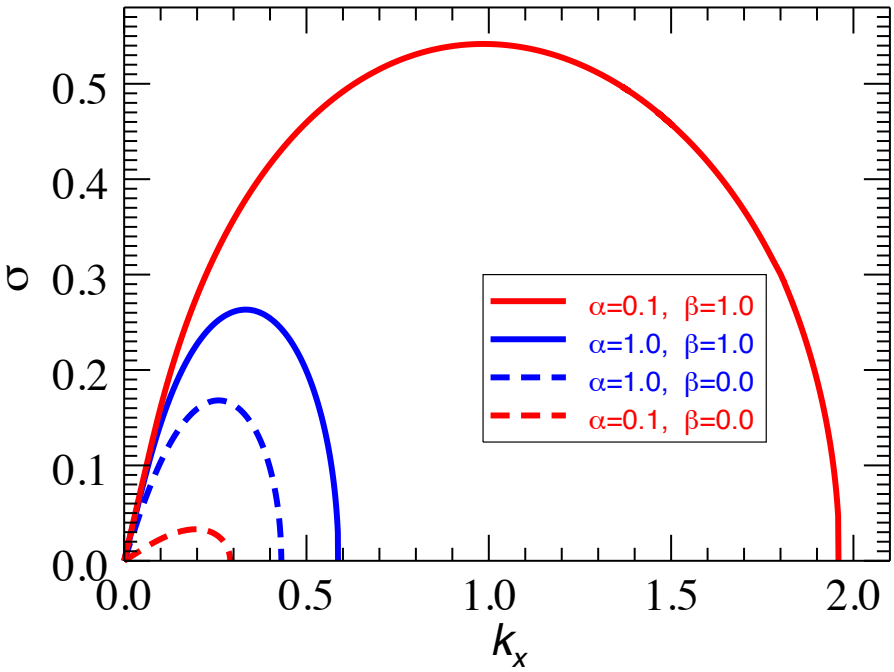

Fig.3.1 Linear growth rate (σ) of the magnetic buoyancy instability for the diffusion coefficient $\kappa_{\parallel} = 200$. Dashed curves show the model for no CR pressure ($\beta = 0$), and solid curves show models including CR pressure ($\beta = 1$)

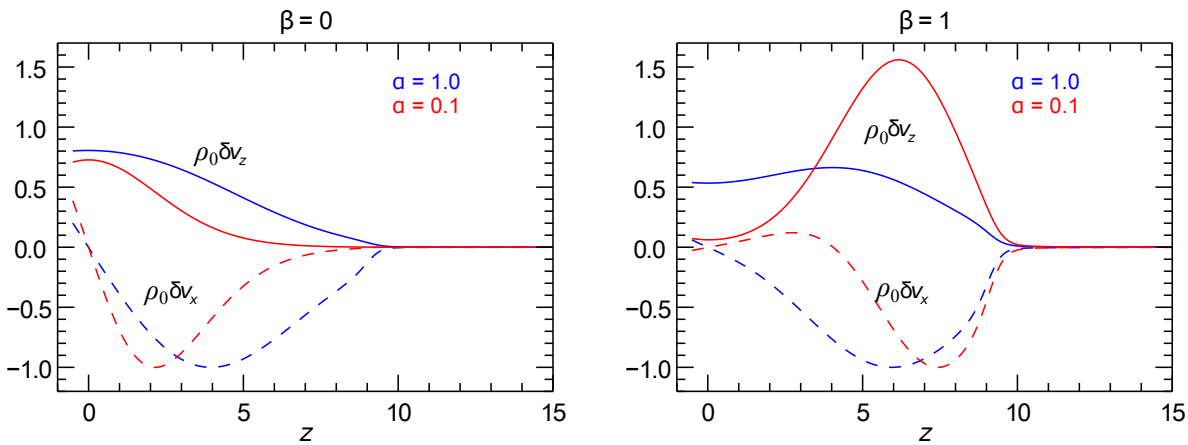

Fig.3.2 Eigenfunctions of fundamental mode of the instability. Left panel shows those without CRs. Right panel shows the case with CR pressure. Solid and dashed curves denote the profiles of $\rho_0\delta v_z$ and $\rho_0\delta v_x$, respectively.

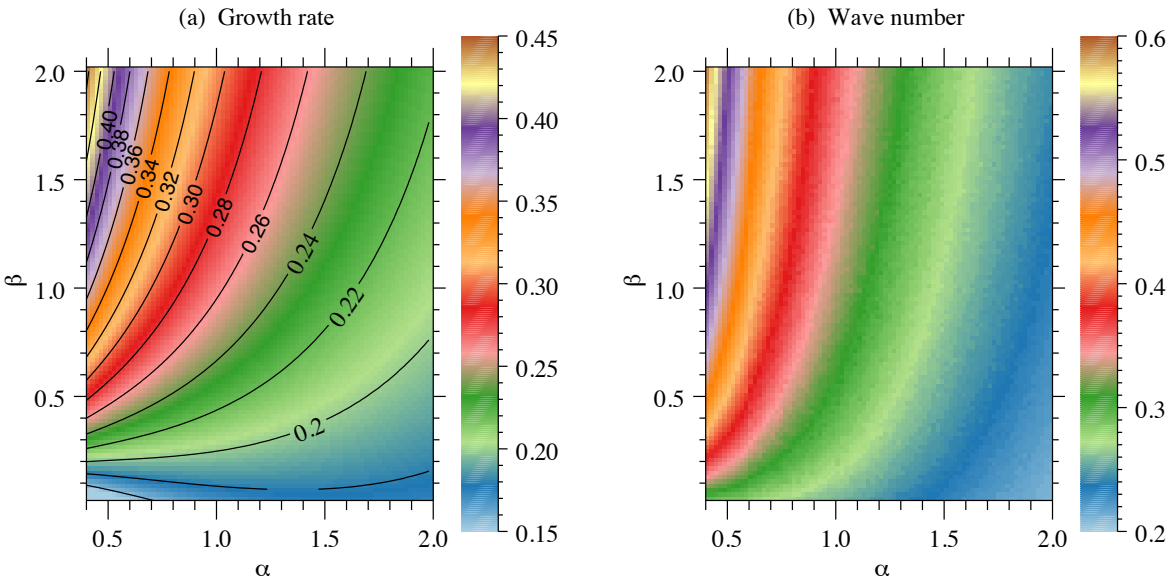

Fig.3.3 (a) Dependence of the growth rate on α and β in fundamental mode of the undulate mode of the magnetic buoyancy instability. Color shows the growth rate. (b) Dependence of the wavenumber on α and β.

maximum growth rate and the critical wave number for the instability strongly depend on the ratio of CR pressure to gas pressure (i.e., β). The growth rate when $\alpha = 0.1$ and $\beta = 1$ (red solid curve) is larger than the model with $\alpha = \beta = 1$. This result is in contrast to the model without CRs (dashed curves) in which the maximum growth rate decreases for weak magnetic field (Horiuchi et al. 1988).

3.3.2 Eigen functions and equatorial plane symmetry

Fig. 3.2 shows the eigenfunctions for the fundamental mode of δv_x and δv_z for the same parameters as those in Fig 3.1. The parity around $z = 0$ is assumed to be odd for δv_x and even for δv_z. When the CR pressure is neglected (left panel of Fig 3.2), the height where δv_x has maximum amplitude approaches to $z = 0$ as magnetic field becomes weak. When the CR pressure is taken into account the height where δv_z has the largest amplitude increases as the magnetic pressure decreases. Table 3.2 summarizes the wavenumber when the growth rate is largest.

Left panel of Fig. 3.3 shows the dependence of the growth rate on the pressure ratio α and β. The maximum growth rate increases as α decreases when $\beta > 0.2$. This result is

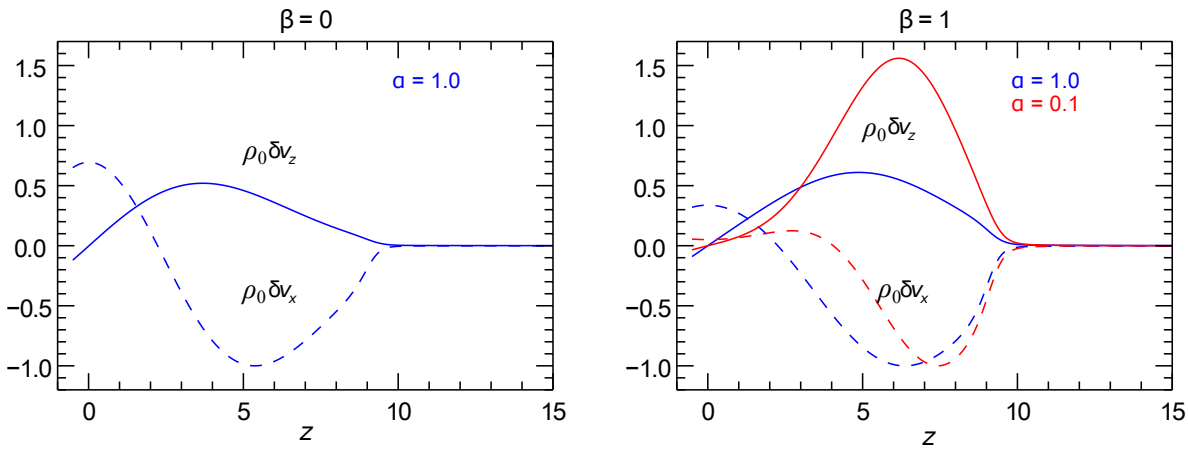

Fig.3.4 The same as Fig. 3.2, but for the 1st harmonic mode.

Table. 3.3 The same as Table 3.2, but for the 1st harmonic mode

Parameter	Wave number k_x	Growth rate σ
$\alpha = 1.0,\ \beta = 0$	0.285	0.13744
$\alpha = 1.0,\ \beta = 1$	0.344	0.25090
$\alpha = 0.1,\ \beta = 1$	0.984	0.54174

in contrast to the model without CRs in which the growth rate increases as α increases.

Fig. 3.4 shows the eigenfunction for the 1st harmonic mode in which v_z is antisymmetric to $z = 0$. When $\beta = 0$, no unstable mode appears in the weak magnetic field models ($\alpha = 0.1$). The eigenfunction for the 1st harmonic mode when $\beta = 1$ and $\alpha = 0.1$ (red curve in the right panel of Fig. 3.4) does not show significant difference from that in the right panel of Fig. 3.2. This degeneracy originates from the small amplitude of the eigenfunction around the equatorial plane. Since the eigenfunctions below and above the equatorial plane do not interfere in weakly magnetized models, the difference between the glide-reflection symmetric mode and the symmetric mode almost disappear. Table 3.3 summarizes the wavenumber for the 1st harmonic mode when the growth rate is largest.

Let us compare the pure Parker instability model $(\alpha, \beta) = (1.0, 0)$ and CR Parker model when $(\alpha, \beta) = (0.1, 1)$, Fig. 3.5 shows the configuration of perturbed quantities. From the velocity field of Fig. 3.2 and Fig. 3.4, the most unstable mode has glide-reflection symmetry (right panels of Fig. 3.5), and the 1st harmonic mode has mirror symmetry.

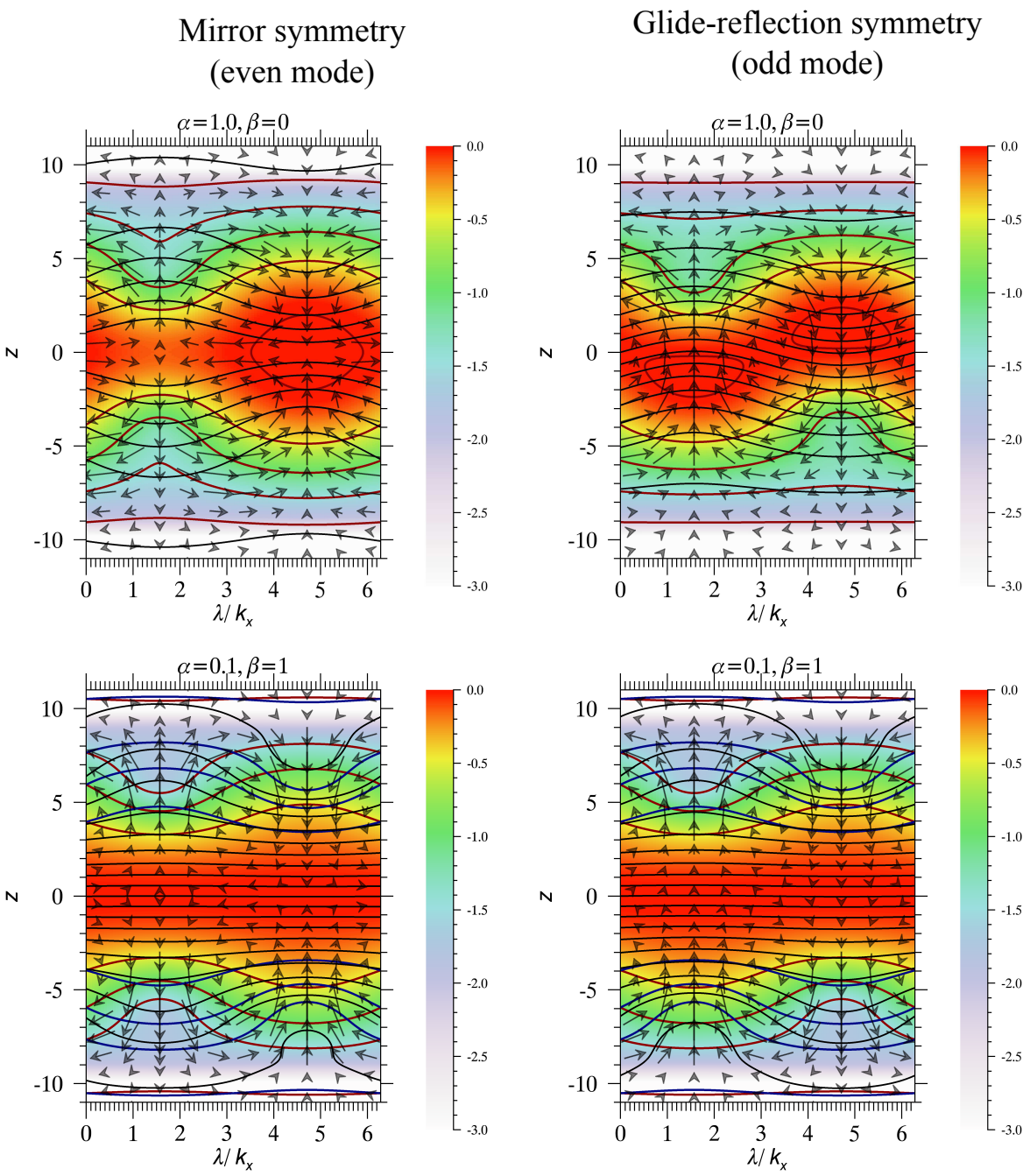

Fig.3.5 Configuration of linear eigenfunctions. Top panels show eigenfunction for Parker instability. Bottom panels are the magnetic buoyancy instability in weakly magnetized disks with CRs. Color shows the density distribution, arrows and black curves are the velocity vectors and magnetic field lines, and red and blue curves show contour of gas and CR pressure, respectively. The amplitude of the perturbation is $\delta\rho/\rho_0 = \delta P_{\rm g}/P_{\rm g,0} = \delta P_{\rm cr}/P_{\rm cr,0} = 0.8$ and $\delta B_x/B_{x,0} = \delta B_z/B_{x,0} = 0.2$.

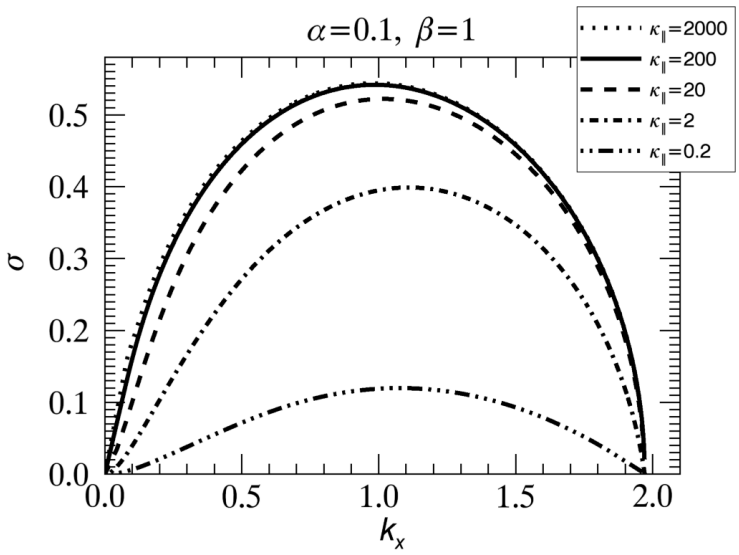

Fig.3.6 Dependence of linear growth rate on CR diffusion coefficient ($\kappa_{\|}$) in weakly magnetic disks, $\alpha = P_{\rm g}/\left(0.5 \times B_x^2\right) = 0.1$. Growth rate for $\kappa_{\|} = 0.2, 2, 20, 200, 2000$ are shown.

3.3.3 CR Diffusion

Let us show the dependence of the growth rate on the CR diffusion coefficient. Fig. 3.6 shows the dispersion relation for a weakly magnetized ($\alpha = 0.1$) disk for various $\kappa_{\|}$. As $\kappa_{\|}$ increases, the maximum growth rate enhanced by the CR diffusion approaches to a constant value $\sigma \sim 0.54$. The maximum wave number for the presence of unstable mode $k_{x,\rm max} \sim 1.97$ is independent of the CR diffusion so long as $\kappa \neq 0$

Fig. 3.7 shows the dependence of the maximum growth rate on $\kappa_{\|}$ for models with $\beta = 1$. When $\alpha \gtrsim 0.5$, the unstable mode exists when $\kappa_{\|} \to 0$. When the magnetic field is weak, the maximum growth rate becomes smaller when $\kappa_{\|}$ is small. It should be noted that in weakly magnetized disks without CR diffusion, Parker instability is stabilized. As we discussed in section 3.1, the critical wavelength for the instability differs for models with $\kappa \neq 0$ from $\kappa_{\|} = 0$.

Figure 1.6 shows that the CR diffusion coefficient $\kappa_{\|}$ does not change the critical wavelength for the instability but significantly affects the growth rate. We note that when $\alpha = 0.1$ and $\kappa_{\|} > 20$, the growth time of the instability is $1/\sigma_{\rm max} \simeq 2 - 5$ which corresponds to $2 - 5 \times 10^7$ yr, which means that the MHD CR instability grows in time scale

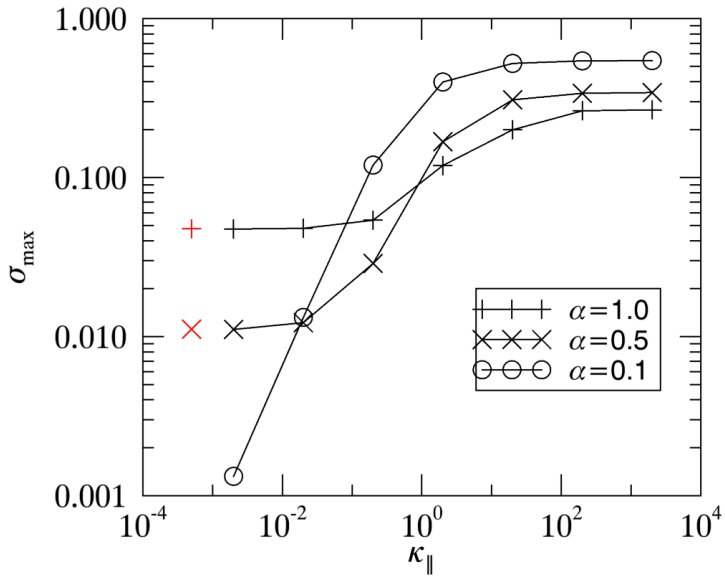

Fig.3.7 Dependence of the maximum growth rate on $\kappa_{\parallel}$. The symbols plus, cross, and circle show the growth rate when $\alpha = 1.0, 0.5$, and 0.1, respectively. Red symbols show the maximum growth rate when CR diffusion is neglected.

shorter than the rotation time of the disk. When $\kappa_{\parallel} < 2$, the CR diffusion time scale becomes longer than the time scale of the Parker instability, so that the growth rate of the instability is reduced.

3.4 Numerical simulations

3.4.1 Numerical set up

We carried out numerical simulations of the magnetic buoyancy instability by solving the CR MHD equation in the two dimensional Cartesian coordinate (x, z) where x is azimuthal direction and z is vertical direction . We set the equatorial plane at $z = 0$, and include the region above and below the equatorial plane in the computational domain. Table 3.4 summarizes the models. We set the boundary conditions in which the left and right boundaries for x-direction are periodic. We imposed wave dumping boundaries in which the physical quantity approach the initial values around the top and bottom in z-direction.

The CR MHD equations are solved by applying the Roe method described in Chapter 2 (Kudoh & Hanawa 2016b). Diffusion terms are discretized by the implicit difference

Table. 3.4 Model parameters.

Model	α	β	Domain (L_x, L_z)	Grid points (N_x, N_z)
P1	1.0	0	(42, 100)	(420, 1000)
P0	0.1	0	(64, 100)	(360, 1000)
C1	1.0	1	(36, 100)	(1440, 4000)
C0	0.1	1	(16, 100)	(640, 4000)

procedure (see, Yokoyama & Shibata 2001), and solved by the BiConjugate Gradients stabilized (BiCGstab) method. The fifth order accuracy in space is achieved by the Monotonicity Preserving interpolation (MP5, see Suresh & Huynh 1997). The third order accuracy in time is achieved by the time integration of the three stage strong stability preserving (SSP) Runge-Kutta scheme (e.g. Suresh & Huynh 1997; Gottlieb & Shu 1998). The CFL number for time integration is fixed to be 0.2.

We made some alternations to the methods described in Chapter 2. First, we adopt the hyperbolic divergence cleaning method (Dedner et al. 2002) in which numerical error induced by $\nabla \cdot \boldsymbol{B} \neq 0$ is dumped. Numerical solutions are controlled by the floor value when the CR pressure or gas pressure become negative. We set the lowest CR pressure to be 10^{-6}. Lower limit for gas pressure is $5 \times 10^{-3}|\boldsymbol{B}|^2$.

In all models, we imposed small velocity perturbation given by the sinusoidal function with even parity in z-direction as,

$$\delta v_x = 0.01 \sin\left(\frac{2\pi x}{\lambda}\right) \times \left[\tanh\left(\frac{z - z_{\rm u}}{0.5}\right) - \tanh\left(\frac{z - z_{\rm d}}{0.5}\right) - \tanh\left(\frac{z + z_{\rm u}}{0.5}\right) + \tanh\left(\frac{z + z_{\rm d}}{0.5}\right)\right] \tag{3.23}$$

where $z_{\rm u} = 3$ and $z_{\rm d} = 1$ are the parameter to restrict the perturbation in region $1 < |z| < 3$, and λ is the perturbation wavelength. We set the horizontal domain size L_x to be twice of the wavelength λ.

3.4.2 Dependence on the magnetic field strength

Fig. 3.8 compares the horizontal velocity v_x obtained from numerical simulation (solid curves) and linear analysis (dashed curves). The growth rate of the instability in the nonlinear solution is consistent with results of the linear analysis. Each model conform

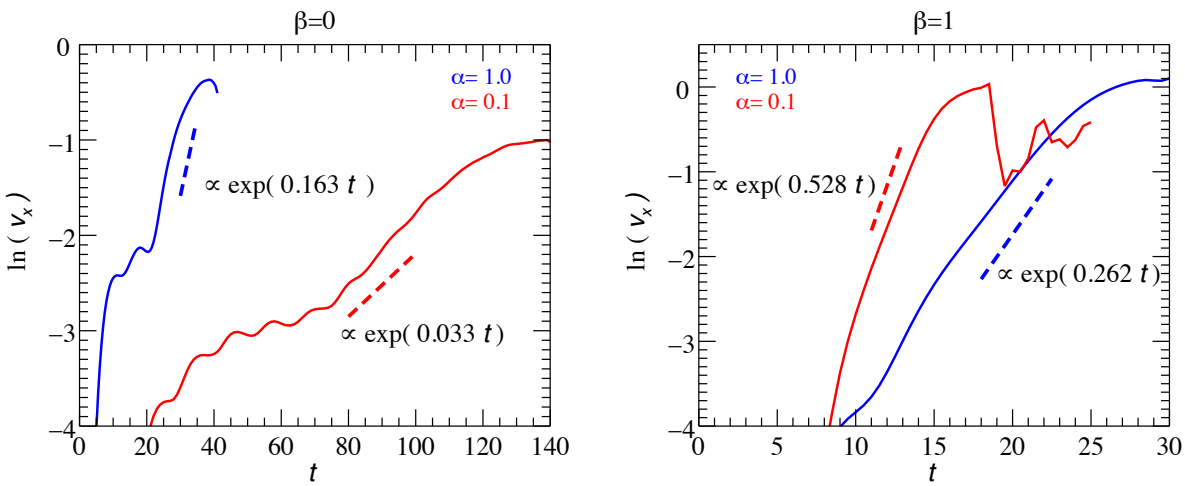

Fig.3.8 The time evolution of v_x in linear regime. Left panel shows the Parker instability without CR pressure $\beta = 0$, right panel shows the magnetic buoyancy instability when $\beta = 1$. Dashed lines denote the linear growth rate. Solid curves show the simulation results at the position of $z = 4$ for the left panel, and of $z = 8$ for the right one.

nearly to the results of the fundamental mode in linear analysis. When CR pressure is neglected, the growth rate decreases as α decreases. When CR pressure is comparable to the gas pressure ($\beta = 1$), growth rate for models with smaller magnetic field ($\alpha = 0.1$) is larger than that for moderate magnetic fields ($\alpha = 1$).

The density distributions in the nonlinear regime are shown in Fig. 3.9. In models C1 and C0, dynamical effects of CR pressure enhance the buoyancy of magnetic loop and uplift the gas frozen to the magnetic field. On the other hand, when CR pressure is negligible (models P1 and P0), the loop top is evacuated. Thus, the density decreases in side the loop. For models C0 and C1, the density only slightly decreases around the loop top.

The vertical distribution of the density and the vertical mass flux are shown in Fig. 3.10. For model P1, low density region is formed around the loop top in the non-linear stage. In model C0, the mass flux is an order of magnitude larger than that for P1.

In the presence of CRs, the buoyancy instability uplifts the disk gas to the disk corona in the nonlinear stage. Black curves in the mass flux in model C0 has peak around $|z| < 4$ and the mass flux becomes small around the equatorial plane.

To determinate the converging and diverging motion, we decompose the velocity field

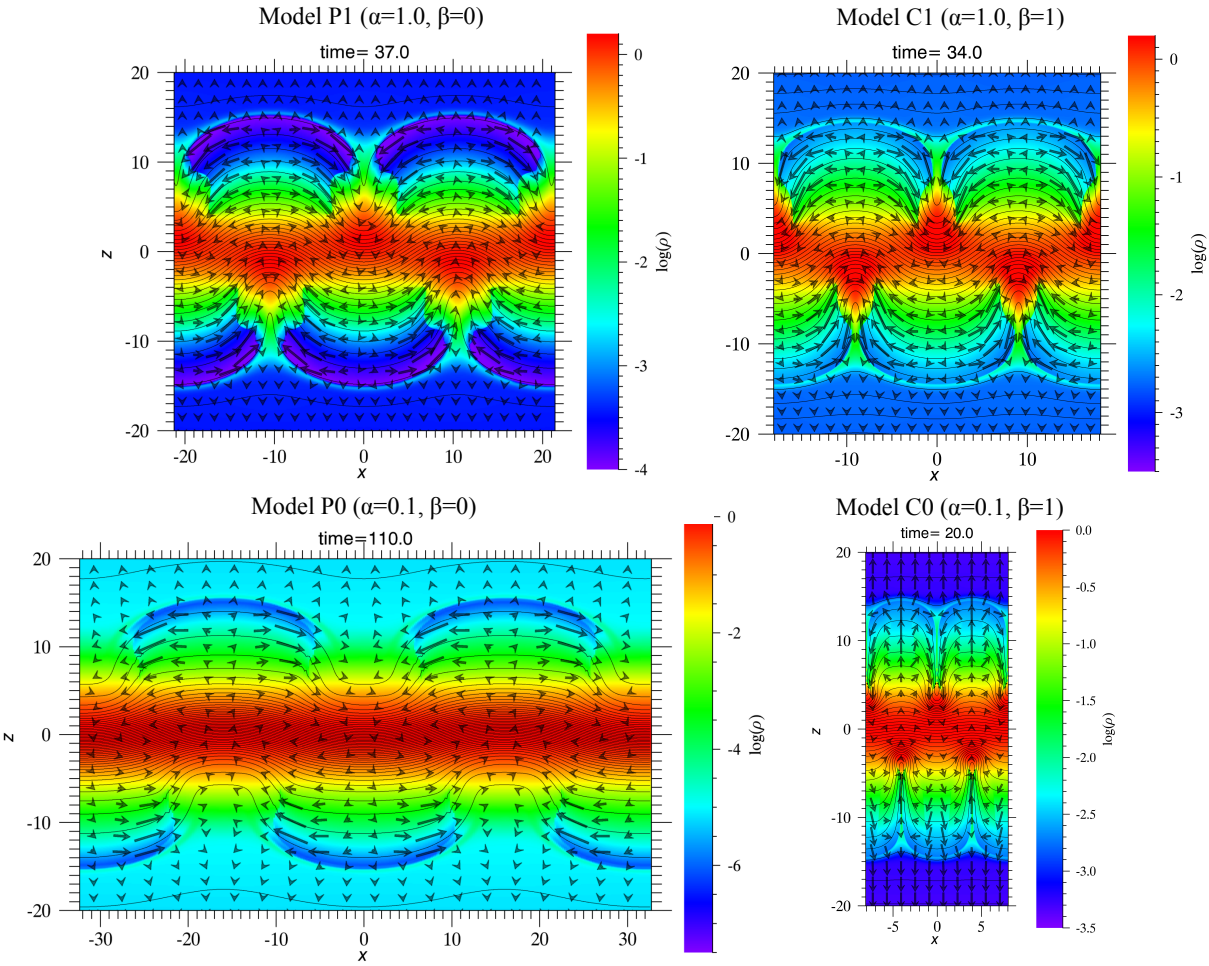

Fig.3.9 Spatial distributions of the density. Left panels show the results for models P0 and P1 without CRs. Top panels show models P1 and C1 with moderate magnetic pressure ($\alpha = 1$), and the bottom panels show P0 and C0 with $\alpha = 0.1$.

into components perpendicular and parallel to the magnetic field,

$$\boldsymbol{v} = \boldsymbol{v}_{\parallel} + \boldsymbol{v}_{\perp}, \tag{3.24}$$

$$\boldsymbol{v}_{\parallel} = \frac{\boldsymbol{v} \cdot \boldsymbol{B}}{|\boldsymbol{B}|^2}\boldsymbol{B}. \tag{3.25}$$

We adopted this analysis according to Isobe et al. (2006) and Takahashi et al. (2009). In Fig. 3.11, red and blue show positive and negative value of $\nabla \cdot \boldsymbol{v}$, $\nabla \cdot \boldsymbol{v}_{\parallel}$, and $\nabla \cdot \boldsymbol{v}_{\perp}$. Left panels are for model P1 at $t = 37$, and right panels are for models C0 at $t = 20$. Without CR pressure, the velocity field is dominated by parallel component $\boldsymbol{v}_{\parallel}$. The compression region (blue color) appears around the foot points of the loop. Expanding region where

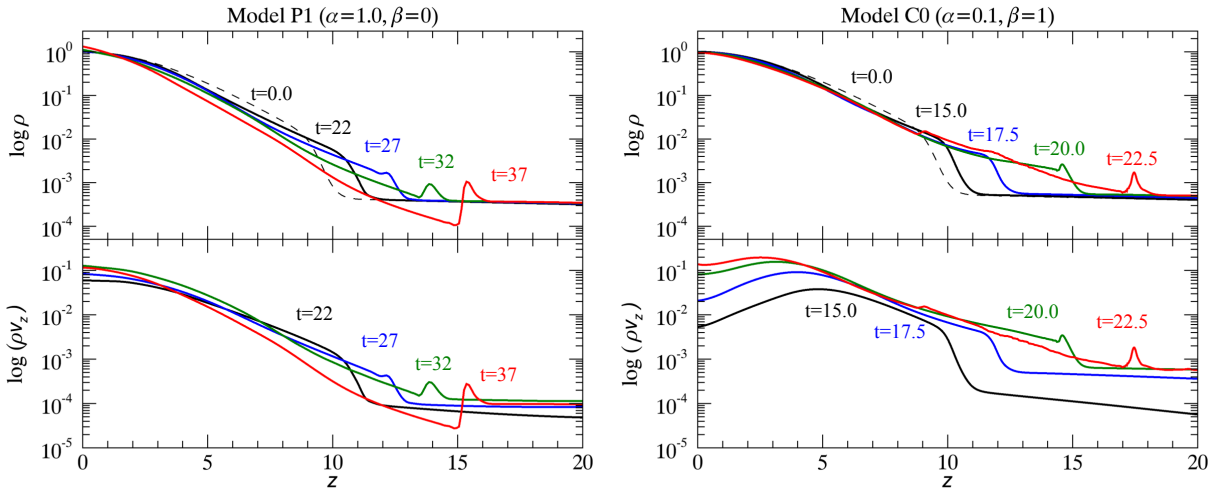

Fig.3.10 Distribution of the density and the vertical mass flux ρv_z at $x = \lambda/2$. Left panel shows those for model P1 without CRs at $t = 22, 27, 32$, and 37. Right panel shows results for the model C0 at $t = 15.0, 17.5, 20.0$, and 22.5. Dashed lines in the density show the initial distribution.

$\nabla \cdot \boldsymbol{v}_{\parallel} > 0$ appears around the loop top. For model C0, perpendicular component $\boldsymbol{v}_{\perp}$ dominates except for the compression region. The result of panel (f) agrees with the vertical mass flux shown in the right panel of Fig. 3.10.

Fig. 3.12 shows the distribution of α and β for model C0. Strongly magnetized CR pressure dominant regions are formed around the loop top. Nonlinear expansion of these regions form dense outflows from the disk. Shock waves are formed inside the magnetic loops where the supersonically expanding region collide.

3.4.3 Dependence of the mass outflow rate on the CR diffusion

We carried out local two dimensional CR magnetohydrodynamic simulations including CR diffusion to study how much mass is ejected from the disk by this instability. Fig. 3.13 shows the density distribution for models with $\kappa_{\parallel} = 0.2(blue), 2(red), and 200(black)$. It should be noted that the density distribution is almost independent of $\kappa_{\parallel}$ except that the time scale for the formation of the outflow strongly depends on $\kappa_{\parallel}$.

Fig. 3.14 shows the distribution of the vertical velocity v_z. The vertical velocity strongly depends on $\kappa_{\parallel}$. When the diffusion coefficient is small ($\kappa_{\parallel} \leq 2$), the vertical speed dose not exceed the sound speed of the disk gas and decreases in the non-linear stage. When

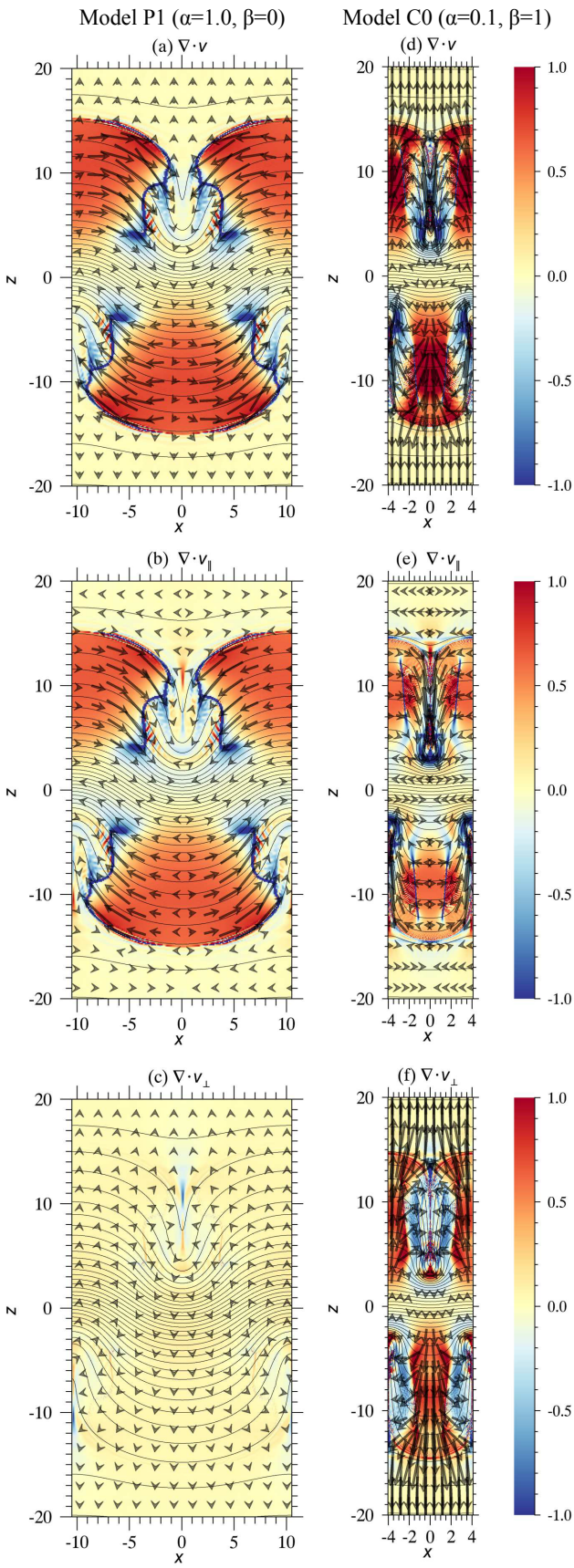

Fig.3.11 Divergence of velocities for the model P1(left panels) and model C0 (right panels). Color shows the divergence of velocity and arrows show the velocity field.

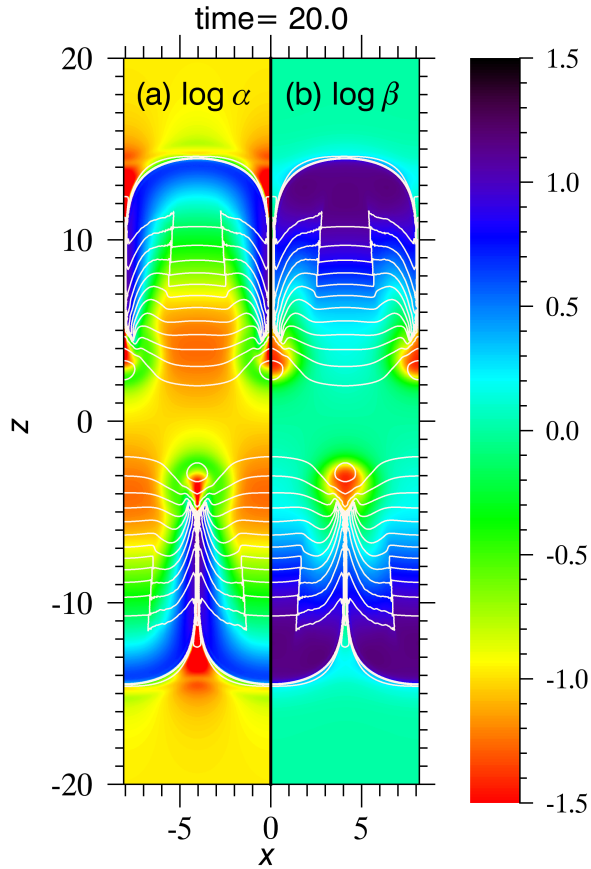

Fig.3.12 Distribution of the pressure ratio in the model C0. White contours show the isocontours of the gas pressure.

CR diffusion is large ($\kappa_{\|} = 200$), the vertical velocity exceeds the sound speed. This supersonic outflow transports the disk gas from the disk to the corona. When $\kappa_{\|}$ is large, the disk gas is expeled from the disk in time scale of $20H/a \sim 2 \times 10^7$ yr. Since this time scale is shorter than the rotation time of the disk, the CR diffusion driven outflow can affect the magnetic field amplification by magneto-rotational instability (MRI) which grows in time scale of rotation of the disk.

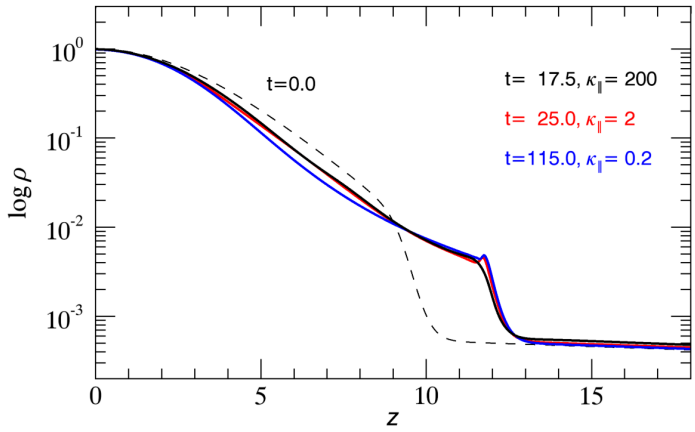

Fig.3.13 Density distribution in the nonlinear stage of the instability when the expanding flow is formed. Solid curves show the vertical distribution of density for models with $\kappa_\parallel$ 0.2 (blue), 2 (red), and 200 (black).

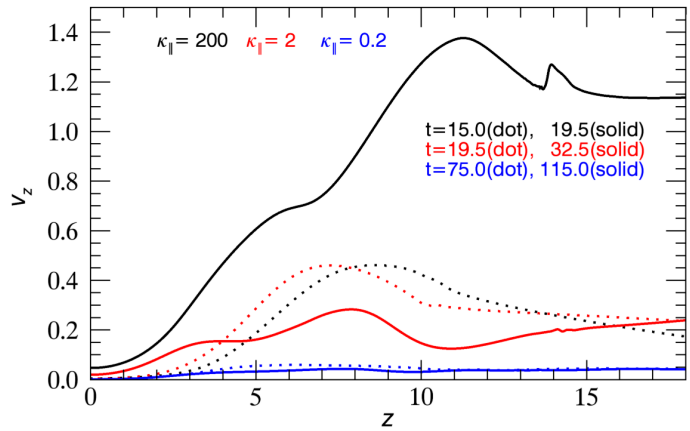

Fig.3.14 Dependence of the vertical velocity distribution on CR diffusion in weakly magnetized disk. Blue, red, and black show results when $\kappa_\parallel$ = 0.2, 2, and 200, respectively.

Chapter 4

Summary and Discussion

4.1 New scheme of CR MHD solver

We have succeeded in rewriting the CR MHD equations in the fully conservation form as shown in Chapter 2. We discuss the advantages of the fully conservation form in this section.

First the Rankine-Hugoniot relation is automatically fulfilled when the CR MHD equations are integrated in the fully conservation form. Thus, the jumps in the density and pressure at MHD shocks are evaluated correctly in the solutions. When we integrate the CR MHD equations in the original form, the numerical solution may violate the Rankine-Hugoniot relation as shown in Section 2.3.3 of Chapter 2.

One might think that any shock tube problems could be solved without using the fully conservation form. Dubois & Commerçon (2016) have succeeded in solving a CR shock tube problem posed by Pfrommer et al. (2006) by evaluating Pdv as the source term. However, the success is in part due to the fact that CR pressure is smaller than the gas pressure in the post-shocked gas. Table 4.2 summarizes the pressure and density distributions in the test problem. The number in the first column specifies the intervals where the density and pressure are constant in the Riemann solution (see Fig. 2.2). The values in regions 2 and 3 are given by the Riemann solution. The CR pressure is dominant in regions 3 and 5 while it is not in region 2, i.e., in the post-shocked gas. Therefore the source term has a minor contribution at the shock front. See Appendix B for more details on these test problems.

Table. 4.1 The shock tube problem of Dubois & Commerçon (2016). The adiabatic indexes are taken to be $\gamma_{\rm g} = \gamma_{\rm cr} = 1.4$ in this test problem.

Region	ρ	$P_{\rm g}$	$P_{\rm cr}$
1	0.100	0.066	0.034
2	0.204	0.192	0.093
3	0.408	0.097	0.187
5	1.000	0.340	0.660

Table. 4.2 The shock tube problem of Pfrommer et al. (2006).

Region	ρ	$P_{\rm g}$ ($\times 10^4$)	$P_{\rm cr}$ ($\times 10^4$)
1	0.200	0.024	0.024
2	0.796	5.141	0.147
3	0.400	1.455	3.832
5	1.000	6.700	13.000

Pfrommer et al. (2006) also succeeded in solving a shock tube problem with their smoothed particle hydrodynamics (SPH) code, although their solution shows small oscillations around shock front and contact discontinuity. Table 4.2 shows the solution of the shock tube problem in Fig. 1 of Pfrommer et al. (2006). Note that the CR pressure is much smaller than the gas pressure in the post-shocked gas (region 2).

The violation of the Rankine-Hugoniot relation is serious when the CR pressure dominates in the post-shocked gas. A clear example is shown in Section 2.3.3 of Chapter 2.

Another advantage of the fully conservation form is that we can easily implement higher order scheme. Various standard higher order schemes are available, when differential equations are written in the fully conservation form (see e.g. Toro (2009) for the methods to achieve higher order accuracy). Remember that the source terms and numerical fluxes have been evaluated separately. Thus the source term can be another source of numerical oscillation when it is evaluated to be of higher order accuracy in space.

The fully conservation form may be useful when we take account of injection of CRs. CRs can be generated from supernova explosions and diffusive shock acceleration. The generation can be taken into account in the CR MHD equations, if it is modeled successfully (see e.g. Zank, Webb & Donohue (1993); Jubelgas et al. (2008); Vazza et al. (2012)). Thus far, only the energy injection rate of cosmic ray number density is taken into account

in the literature. However, we can take account of both the energy injection rate, S_E, and the injection rate in number, S_ρ, in the fully conservation form. In the following we assume that $E_{\rm cr}$ and $\rho_{\rm cr}$ are related by

$$E_{\rm cr} = \frac{K\rho_{\rm cr}^{\gamma_{\rm cr}}}{\gamma_{\rm cr}-1}, \tag{4.1}$$

where K denotes the CR *entropy* and has been assumed to be $K = 1$ thus far. If the injection is taken into account, the change in K should be described as

$$\frac{1}{K}\frac{dK}{dt} = \frac{S_E}{E_{\rm cr}} - \gamma_{\rm cr}\frac{S_\rho}{\rho_{\rm cr}} \tag{4.2}$$

$$= \frac{S_\rho}{E_{\rm cr}}\left(\frac{S_E}{S_\rho} - \gamma_{\rm cr}\frac{E_{\rm cr}}{\rho_{\rm cr}}\right), \tag{4.3}$$

where dK/dt denotes the Lagrangian derivative. Equation (4.3) follows the change in the average energy of CRs, $E_{\rm cr}/\rho_{\rm cr}$. The average CR energy gives us important information to estimate the diffusion coefficient.

This paper has proved the usefulness of CR number conservation, equation (2.11). It is derived from and equivalent to the CR energy equation, equation (2.7). However, the former is written in the fully conserved form, while the latter is not. The former is more suitable for numerical analysis than the latter, since the approximate Riemann solutions are given explicitly and hence shock waves are reproduced without numerical oscillations. The derived approximate Riemann solutions are only slightly different from those for the ideal MHD equations: the sound speed is modified by inclusion of the CR pressure and a new mode, the pressure balance mode, is added. Thus we can construct higher order scheme by applying the methods developed for the ideal MHD equations. We have also suggested to extend the CR MHD equations by introducing the CR entropy. This extension enables us to evaluate the average CR energy. It should be useful to estimate the diffusion and emission from CRs.

4.2 Magneto CR instability

We have studied the magnetic buoyancy instability taking into account CRs by the linear analysis and numerical simulations in Chapter 3.

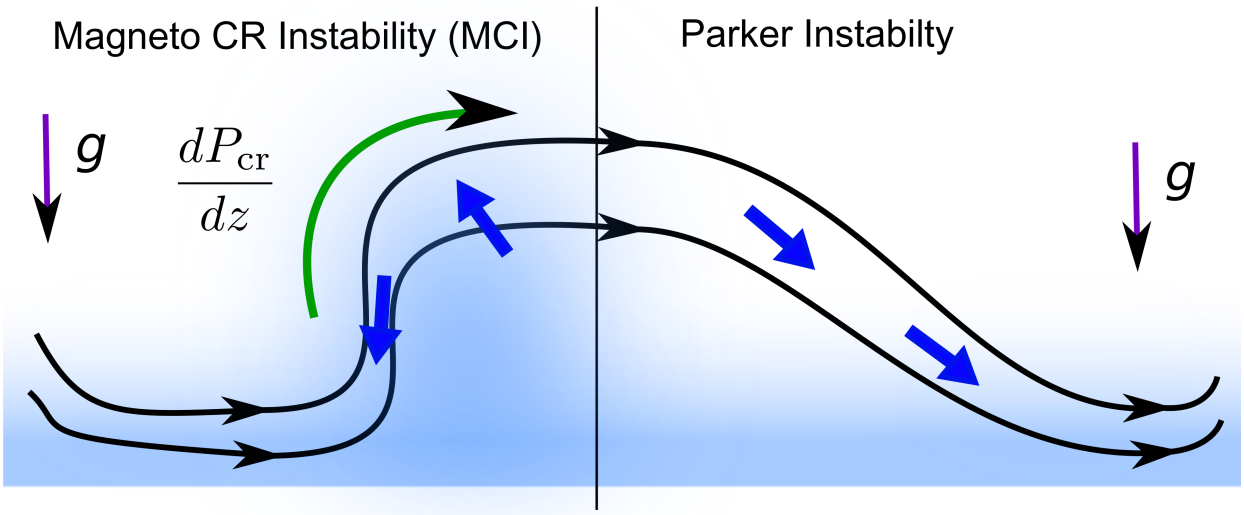

Fig.4.1 Illustration of Magneto Cosmic-ray Instability (MCI) and Parker instability.

We showed the dependence of the growth rate and eigenfunctions on the magnetic field strength α by solving the eigenvalue problem of the linearized equations. We showed that the most unstable mode has the glide-reflection symmetry with respect to the equatorial plane. In weakly magnetized disks ($\alpha < 1$), when the cosmic ray pressure is comparable to the gas pressure, the eigen function of the linearized equations approach to zero around $z = 0$, and the height where the amplitude of the eigenfunction becomes maximum shift to higher z region where $g_z(z)/T(z)$ is largest. We found that the growth rate of the magnetic buoyancy instability with CR diffusion ($\beta > 0$) increases as the magnetic pressure decreases. This is in contrast to the Parker instability when $\beta = 0$, in which the growth rate decreases as α decreases. The critical wavenumber for the instability increases as α decreases, and becomes larger than that without CRs. We also showed that the difference of the growth rate and the eigenfunction between the fundamental mode (with

glide-reflection symmetry) and the 1st harmonic mode (with equatorial mirror symmetry) becomes smaller.

CR diffusion along the magnetic field lines enhances the growth of the undular mode of the magnetic buoyancy instability even when the magnetic field is weak. This instability is driven by the buoyancy force by CRs as shown in Fig. 4.1. We call this instability as Magneto Cosmic-ray Instability (MCI). The mechanism of MCI is similar to the magneto-thermal instability (MTI) driven by thermal conduction along the magnetic field lines (Parrish & Stone, 2005). In MCI, cosmic ray diffusion along the magnetic field lines drives the buoyant rise of the magnetic loop.

The critical wavelength for MCI can be derived as follows; We assume an isothermal disk in the uniform gravity in which alpha and beta are constant in unperturbed state. When the undular perturbation Δ z is imposed, the total pressure inside the undulating magnetic field should be in the pressure equilibrium with the surrounding medium,

$$P_{\mathrm{g,in}}(z+\Delta z)+P_{B,\mathrm{in}}(z+\Delta z)+P_{\mathrm{cr,in}}(z+\Delta z)=(1+\alpha+\beta)\,P_{\mathrm{g}}(z)\exp\left(-\frac{\Delta z}{H}\right), \tag{4.4}$$

where subscript (-in) denotes the quantity inside the magnetic loop. Let us assume that CR pressure diffuses along the magnetic field lines instantly,

$$P_{\mathrm{cr,in}}(z+\Delta z)\sim P_{\mathrm{cr}}(z)=\beta P_{\mathrm{g}}(z). \tag{4.5}$$

By denoting the scale height of the magnetic pressure inside the magnetic loop as H_B, the magnetic pressure inside is,

$$P_{\mathrm{B,in}}(z+\Delta z)\sim P_B(z)\exp\left(-\frac{\Delta z}{H_B}\right)=\alpha P_{\mathrm{g}}(z)\exp\left(-\frac{\Delta z}{H_B}\right). \tag{4.6}$$

We assume that the gas pressure changes adiabatically,

$$P_{\mathrm{g,in}}(z+\Delta z)=P_{\mathrm{g}}(z)\left(\frac{\rho_{\mathrm{in}}(z+\Delta z)}{\rho(z)}\right)^{\gamma_{\mathrm{g}}}. \tag{4.7}$$

We introduce the density perturbation $\delta(<0)$ defined by,

$$1+\delta = \frac{\rho_{\rm in}(z+\Delta z)}{\rho(z)}. \tag{4.8}$$

Hence, the pressure balance equation (4.4) can be written as

$$(1+\delta)^{\gamma_{\rm g}} + \alpha \exp\left(-\frac{\Delta z}{H_B}\right) + \beta = (1+\alpha+\beta)\exp\left(-\frac{\Delta z}{H}\right). \tag{4.9}$$

Using the Taylor series for $|\delta| \ll 1$, $\Delta z/H_B \ll 1$, and $\Delta z/H \ll 1$, we obtain

$$\delta = \frac{\Delta z}{\gamma_{\rm g}}\left(\frac{\alpha}{H_B} - \frac{1+\alpha+\beta}{H}\right) \tag{4.10}$$

The buoyancy force $F_{\rm buoyancy}$ can be evaluated as,

$$F_{\rm buoyancy} = (\rho_{\rm in}(z+\Delta z) - \rho(z+\Delta z))g \tag{4.11}$$

$$\sim -\left(\delta + \frac{\Delta z}{H}\right)\rho(z)g \tag{4.12}$$

$$= \frac{\Delta z}{\gamma_{\rm g}}\rho(z)g\left[\frac{1+\alpha+\beta-\gamma_{\rm g}}{H} - \frac{\alpha}{H_B}\right]. \tag{4.13}$$

By estimating the the magnetic tension force using equation (1.15), the critical wavenumber for the instability is,

$$H^2k_x^2 < \frac{\pi^2}{8}\left[\frac{(1+\alpha+\beta)(1+\alpha+\beta-\gamma_{\rm g})}{2\alpha\gamma_{\rm g}} - \frac{(1+\alpha+\beta)}{2\gamma_{\rm g}}\frac{H}{H_B}\right] \tag{4.14}$$

This equation coincides with equatoin (3.2) if we replace $\pi^2/8$ with 1, and the last term in the right hand as 1/4.

On the other hand when CR diffusion is neglected ($\kappa_{\|} = 0$), we can evaluate the CR pressure inside the magnetic loop as,

$$P_{\rm cr,in}(z+\Delta z) = P_{\rm cr}(z)\left(\frac{\rho_{\rm in}(z+\Delta z)}{\rho(z)}\right)^{\gamma_{\rm cr}}. \tag{4.15}$$

By using the pressure balance equation (2.4), the density fluctuation δ can be estimated

as,

$$\delta = \frac{\Delta z}{\gamma_{\rm g} + \beta\gamma_{\rm cr}} \left(\frac{\alpha}{H_B} - \frac{1+\alpha+\beta}{H} \right). \tag{4.16}$$

The critical wave number can be evaluated as

$$H^2 k_x^2 < \frac{\pi^2}{8} \left[\frac{(1+\alpha+\beta)(1+\alpha+\beta-\gamma_{\rm g}-\beta\gamma_{\rm cr})}{2\alpha(\gamma_{\rm g}+\beta\gamma_{\rm cr})} - \frac{1+\alpha+\beta}{2(\gamma_{\rm g}+\beta\gamma_{\rm cr})} \frac{H}{H_B} \right] \tag{4.17}$$

We presented the results of two-dimensional CR+MHD simulations of the magnetic buoyancy instability in magnetized galactic gas disks. We showed that the MCI enables the buoyant rise of the magnetic loops from weakly magnetized disk with CRs. The growth rate of MCI is larger than that of the Parker instability in weakly magnetized disks, and the most unstable wavelength of MCI is smaller than the Parker instability. Since the disk gas is frozen to the magnetic field, the disk gas is uplifted as the magnetic loops rise.

Let us discuss the influence of MCI on galactic dynamo. Magnetic fields in disk galaxies can be amplified and maintained by MRI driven dynamo. When CRs are negligible, the buoyant escape of the magnetic flux by Parker instability limits the strength of disk magnetic fields and drives cyclic dynamo whose period is about 10 rotation period of the disk (e.g., Nishikori, Machida & Matsumoto 2006; Machida et al. 2013). We can compere time scale with $\tau_{\rm dynamo}$ in which magnetic field is amplified by MRI,

$$\tau_{\rm dynamo} = 10 \times 2.7 \times 10^7 \left[\frac{r}{1{\rm kpc}} \right] \left[\frac{v_{\rm rot}}{220{\rm km/s}} \right]^{-1} \quad {\rm yr}, \tag{4.18}$$

where r is the radius and $v_{\rm rot}$ is the rotation speed, respectively. Our results of linear analysis show $\tau_{\rm Parker} \sim 5.8 \times 10^7$ yr in the pure Parker instability. Obviously, time scale for Parker instability is shorter than that for MRI in strong magnetic field $\alpha = 1$. However, when the magnetic field is weak (e.g. $\alpha < 0.1$) in early stage of galactic evolution, since the growth rate decreases, the magnitude of these two time scales is reversed. When the magnetic field is weak and the CR diffusion is taken into account, the growth time of MCI is $\tau_{\rm MCI} \sim 1.9 \times 10^7$yr for $\kappa_\parallel = 200$ and $\tau_{\rm MCI} \sim 8.4 \times 10^7$ yr for $\kappa_\parallel = 0.2$. The CR diffusion time scale is small enough to drive the buoyant rise of magnetic flux in time scale

shorter than the growth time of magnetic field by MRI. Therefore, the CR diffusion and MCI should affect the MRI driven dynamo in galactic gas disks. Linear analysis of MRI with CRs have been carried out by Khajenabi (2012) and Kuwabara & Ko (2015). They showed that the effects of CRs on MRI is not large. However, since MCI enhances the escape of magnetic flux from the disk, it will affect the saturation level of the MRI driven dynamo. For example, when the magnetic field is weak, the nonlinear growth of the Parker instability without CRs leads to oscillation rather than the continuous escape of magnetic flux from the disk (Matsumoto et al. 1990). However, MCI will drive buoyant escape of magnetic flux even in weakly magnetized disks. It will be our future work to study the nonlinear growth of the MRI-MCI driven dynamo in galactic gas disks. We found that in weakly magnetize disks, cosmic ray diffusion drives outflows when the diffusion coefficient $\kappa_{\parallel}$ is large. The mass outflow rate can be 5.1×10^3 $M_{\odot}$/Myr at $z = 1.5$ kpc estimated by the right panel of Fig. 3.10. It is also our future work to study the effect of this outflow on the evolution of galaxy and galactic halo.

Appendix A

Analytic Solution of Riemann Problem in CRHD System

We describe the algorithm to obtain analytic Riemann solutions of the 1D CR HD shock-tube problem. The solutions have four patterns depending on the initial state (see, e.g., Toro 2009). Here, we restrict ourselves to case (a) of Toro (2009) in which a shock wave propagates rightward and rarefaction wave does leftward as illustrated Figure 2.1.

All the variables depend on x/t in a Riemann solution. According to Toro (2009) we consider five regions numbered from right to left. The state vector $\boldsymbol{U}$ is expressed as

$$\boldsymbol{U} = \begin{cases} \boldsymbol{U}_1 = \boldsymbol{U}_{\mathrm{R}} & x/t < S_{\mathrm{HR}} \\ \boldsymbol{U}_2 & S_{\mathrm{HR}} \leq x/t < S_{\mathrm{TR}} \\ \boldsymbol{U}_3 & S_{\mathrm{TR}} \leq x/t < S_* \\ \boldsymbol{U}_4 & S_* \leq x/t < S_{\mathrm{R}} \\ \boldsymbol{U}_5 = \boldsymbol{U}_{\mathrm{L}} & x/t \geq S_{\mathrm{R}}, \end{cases} \tag{A.1}$$

where S_{HR} and S_{TR} denote the speeds for the head and tail of rarefaction wave, respectively. The symbols, S_* and S_{R}, denote the velocity at the contact discontinuity and the wave speed of the shock traveling rightward, respectively.

First we consider the Rankine-Hugniot relation for the shock wave at $x/t = S_{\mathrm{R}}$. They

are expressed as

$$\rho_2 \hat{v}_{x2} = \rho_1 \hat{v}_{x1} \equiv \hat{Q}, \tag{A.2}$$

$$\rho_2 \hat{v}_{x2}^2 + P_{\mathrm{T}2} = \rho_1 \hat{v}_{\mathrm{x}1}^2 + P_{\mathrm{T}1}, \tag{A.3}$$

$$\rho_2 H_2 \hat{v}_{x2} = \rho_1 H_1 \hat{v}_{x1}, \tag{A.4}$$

$$\rho_2 \chi_2 \hat{v}_{x2} = \rho_1 \chi_1 \hat{v}_{x1}, \tag{A.5}$$

in the comoving frame, where the symbols with hat denote the values in the comoving frame. They are expressed as

$$\hat{v}_{x2} = v_{x2} - S_R, \tag{A.6}$$

$$\hat{v}_{x1} = -S_R, \tag{A.7}$$

since $v_{x1} = 0$.

We obtain

$$\hat{Q} = -\rho_1 \rho_2 \frac{\hat{v}_1 - \hat{v}_2}{\rho_1 - \rho_2}, \tag{A.8}$$

$$\hat{Q}^2 = -\rho_1 \rho_2 \frac{P_{\mathrm{T}1} - P_{\mathrm{T}2}}{\rho_1 - \rho_2}, \tag{A.9}$$

from equations (A.2) and (A.3). We obtain

$$\hat{v}_{x2}^2 = \frac{\rho_1}{\rho_2} \frac{P_{\mathrm{T}1} - P_{\mathrm{T}2}}{\rho_1 - \rho_2}, \tag{A.10}$$

$$\hat{v}_{x1}^2 = \frac{\rho_2}{\rho_1} \frac{P_{\mathrm{T}1} - P_{\mathrm{T}2}}{\rho_1 - \rho_2}, \tag{A.11}$$

$$v_{x2} = v_{x1} - \sqrt{(P_{\mathrm{T}1} - P_{\mathrm{T}2}) \left(\frac{1}{\rho_2} - \frac{1}{\rho_1} \right)}, \tag{A.12}$$

by eliminating $\hat{Q}$ from equations (A.8) and (A.9). We obtain

$$P_{\mathrm{cr}2} = P_{\mathrm{cr}1} \left(\frac{\rho_2}{\rho_1} \right)^{\gamma_{\mathrm{cr}}}, \tag{A.13}$$

from equation (A.5). We also obtain

$$\frac{\hat{v}_{x1}^2}{2} + \frac{P_{\mathrm{g1}}}{\rho_1\left(\gamma_{\mathrm{g}}-1\right)} + \frac{P_{\mathrm{cr1}}}{\rho_1\left(\gamma_{\mathrm{cr}-1}\right)} = \frac{\hat{v}_{x2}^2}{2} + \frac{P_{\mathrm{g2}}}{\rho_2\left(\gamma_{\mathrm{g}}-1\right)} + \frac{P_{\mathrm{cr2}}}{\rho_1\left(\gamma_{\mathrm{cr}-1}\right)}, \tag{A.14}$$

from equation (A.4). By solving equation (A.14) for P_{g2} we obtain

$$\begin{aligned} P_{\mathrm{g2}} = & \frac{r+1+\gamma_{\mathrm{g}}(r-1)}{r+1-\gamma_{\mathrm{g}}(r-1)} P_{\mathrm{g1}} \\ & - \left[\frac{r+1-\gamma_{\mathrm{cr}}(r-1)}{r+1-\gamma_{\mathrm{cr}}(r-1)} r^{\gamma_{\mathrm{cr}-1}} - \frac{r+1+\gamma_{\mathrm{cr}}(r-1)}{r+1-\gamma_{\mathrm{g}}(r-1)}\right] \frac{\gamma_{\mathrm{g}}-1}{\gamma_{cr}-1} P_{\mathrm{cr1}}, \end{aligned} \tag{A.15}$$

$$r = \frac{\rho_1}{\rho_2}. \tag{A.16}$$

Equation (A.15) shows that the gas pressure in region 2, P_{g2}, can be expressed as a function of ρ_2 since ρ_1, P_{g1}, and P_{cr1} are given. Similarly the CR pressure in region 2, P_{cr2}, is expressed as a function of ρ_2 in equation (A.13). Then equation (A.12) evaluate v_{x2} as a function of ρ_2.

Since the velocity and the total pressure are constant across the contact discontinuity, we obtain

$$v_{x2} = v_{x3} = S_*, \tag{A.17}$$

$$P_{\mathrm{T2}} = P_{\mathrm{T3}}. \tag{A.18}$$

In the following we show that v_{x3} and P_{T3} can be expressed as a function of ρ_3, $\rho_5 = \rho_{\mathrm{L}}$, $P_{\mathrm{g5}} = P_{\mathrm{gL}}$, and $P_{\mathrm{cr5}} = P_{\mathrm{crL}}$. Regions 3 through 5 are connected by the Riemann invariants for the rarefaction. The gas and CR pressure distributions are expressed

$$P_{\mathrm{g3}} = P_{\mathrm{g5}} \left(\frac{\rho_3}{\rho_1}\right)^{\gamma_{\mathrm{g}}}, \tag{A.19}$$

$$P_{\mathrm{cr3}} = P_{\mathrm{cr5}} \left(\frac{\rho_3}{\rho_1}\right)^{\gamma_{\mathrm{cr}}}, \tag{A.20}$$

since the entropy and CR concentration are constant. Equation (2.39) provides us

$$v_{x3} = v_{x5} - \int_{\rho_1}^{\rho_3} \frac{a}{\rho} d\rho = S_{\mathrm{TR}}, \tag{A.21}$$

$$a^2 \equiv \frac{\gamma_{\mathrm{g}} P_{\mathrm{g}5}}{\rho_5} \left[\left(\frac{\rho}{\rho_5} \right)^{\gamma_{\mathrm{g}}-1} + \frac{\gamma_{\mathrm{cr}} P_{\mathrm{cr}5}}{\gamma_{\mathrm{g}} P_{\mathrm{g}5}} \left(\frac{\rho}{\rho_5} \right)^{\gamma_{\mathrm{cr}}-1} \right]. \tag{A.22}$$

The integral in equation (A.21) has an analytic expression when $\gamma_{\mathrm{cr}} = 4/3$. It is transformed into

$$\begin{aligned} I(\rho) &\equiv \int_{\rho_5}^{\rho_3} \frac{a}{\rho} d\rho \\ &= \sqrt{15 \frac{P_{\mathrm{g}5}}{\rho_5}} \int_0^{\frac{1}{3} ln(\frac{\rho_3}{\rho_5})} \sqrt{e^{2t} + \frac{4P_{\mathrm{cr}5}}{5P_{\mathrm{g}5}} e^t} \; dt, \end{aligned} \tag{A.23}$$

by the variable transformation $t = \ln (\rho/\rho_1)^{1/3}$. The integral in equation (A.23) is evaluated by the mathematical formula,

$$\int^x \sqrt{e^t(e^t + C)} \; dt = \sqrt{e^t(e^t + C)} + C ln \left[(e^{t/2} + \sqrt{e^x + C}) \right], \tag{A.24}$$

where C denotes a constant.

By try and error, we search for ρ_2 and ρ_3 which satisfy equation (A.17) and (A.18) simultaneously. Then the Riemann solution is obtained.

Appendix B

CR HD shock tube problem

We reexamine the shock tube problems examined in earlier works.

Fig. B.1 shows the solutions of the shock tube problem of Dubois & Commerçon (2016) of which initial state is summarized in Table 4.1. We have solved the problem on the uniform cell width of $\Delta x = 1/128$ with the time step, $\Delta t = 2.45 \times 10^{-3}$. The blue and red curves denote the solutions at $t = 0.245$ obtained with Pdv scheme and ours, respectively. The exact solution is denoted by the black. The upper panels denote ρ, v_x and s as a function of x from left to right, while the lower panels do $P_{\rm g}$, $P_{\rm cr}$, and χ. Only the region of $-0.05 \leq x \leq 0.50$ is shown. The Pdv scheme gives an apparently good approximation for ρ, v_x, s, $P_{\rm g}$, and $P_{\rm cr}$ but not for χ. Our scheme provides a better approximation.

The spurious sound wave emission is not observed in this test problem since $\gamma_{\rm g} = \gamma_{\rm cr} = 1.4$. This is because the spurious increase in the pressure is proportional to $\gamma_{\rm g} - \gamma_{\rm cr}$ as shown in equation (2.82).

Fig. B.2 shows the solutions of the shock tube problem Pfrommer et al. (2006) of which initial state is given in Table 4.2. Also this problem has been solved on the uniform cell width of $\Delta x = 1/128$ with the time step, $\Delta t = 8.0 \times 10^{-6}$. The solution at $t = 4.4 \times 10^{-4}$ obtained with the Pdv scheme is denoted by the blue curves, while that obtained with our scheme is by the red ones. The black curves denote the exact solution. Each panel shows ρ, v_x, s, $\log P_{\rm g}$, $\log P_{\rm cr}$, and $\log \chi$. In this example, both the schemes provide a good approximation. This is mainly because the CR pressure is by a factor of 10 lower than the gas pressure between the contact discontinuity and the shock front ($0.1942 \leq x \leq 0.2612$).

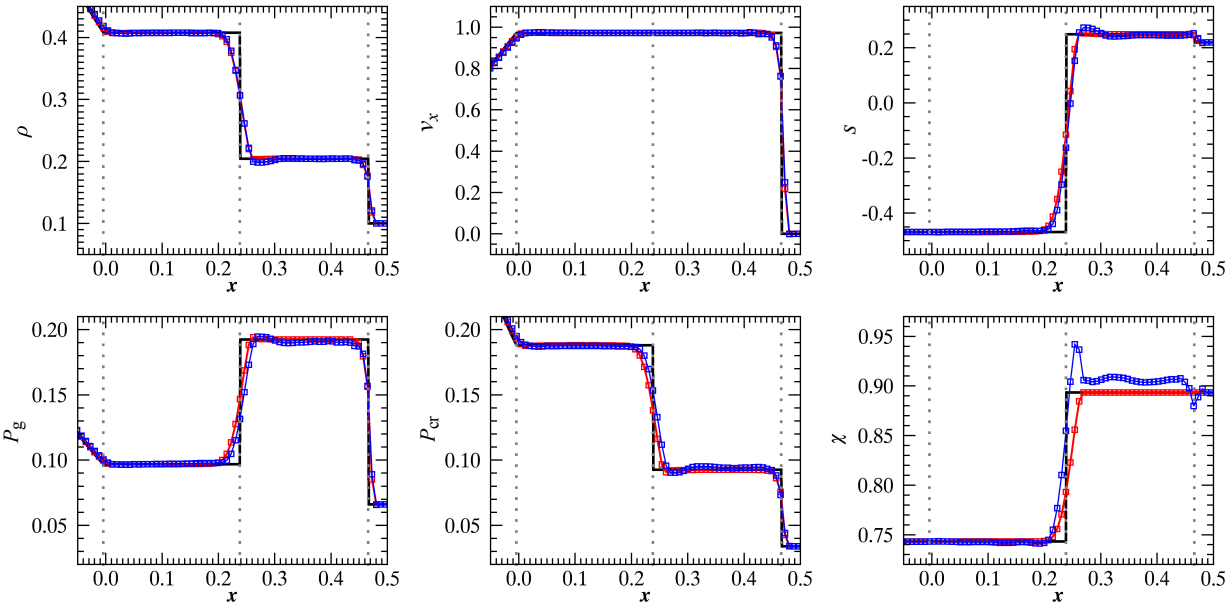

Fig.B.1 The CRHD shock tube problem of Dubois & Commerçon (2016). The grey dotted lines denote the tail of rarefaction ($x = 4.218 \times 10^{-3}$), contact discontinuity ($x = 0.2380$), and shock ($x = 0.4660$) at $t = 0.245$ from left to right. The CFL number is taken to be 0.743.

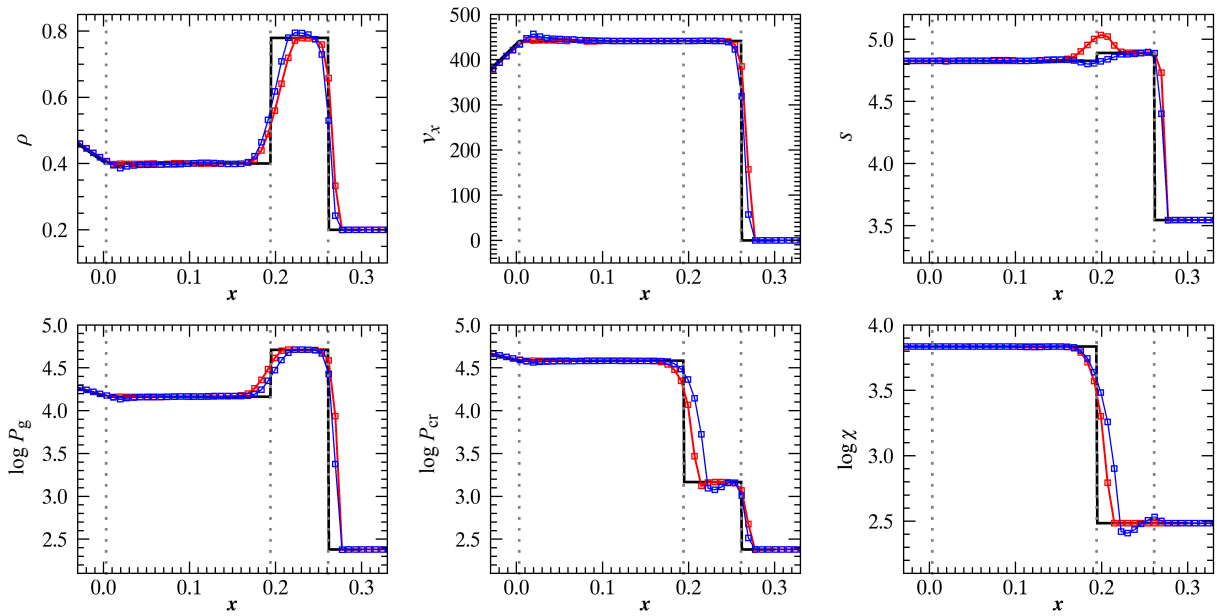

Fig.B.2 The CRHD shock tube problem of Pfrommer et al. (2006). The grey dotted lines denote the tail of rarefaction ($x = 3.232 \times 10^{-3}$), contact discontinuity ($x = 0.1942$), and the shock ($x = 0.2612$) at $t = 4.4 \times 10^{-4}$ from left to right. The CFL number is taken to be 0.794.

Bibliography

Armstrong J. W., Rickett B. J., Spangler S. R., 1995, ApJ, 443, 209

Balbus S. A., Hawley J. F., 1991, ApJ, 376, 214

Berezinskii V. S., Bulanov S. V., Dogiel V. A., Ptuskin V. S., 1990, Astrophysics of cosmic rays

Brio M., Wu C. C., 1988, Journal of Computational Physics, 75, 400

Butsky I., Zrake J., Kim J.-h., Yang H.-I., Abel T., 2016, ArXiv e-prints

Chepurnov A., Lazarian A., 2010, ApJ, 710, 853

Cowling T. G., 1934, MNRAS, 94, 768

Dedner A., Kemm F., Kröner D., Munz C.-D., Schnitzer T., Wesenberg M., 2002, Journal of Computational Physics, 175, 645

Draine B. T., 2011, Physics of the Interstellar and Intergalactic Medium

Dubois Y., Commerçon B., 2016, A&A, 585, A138

Fahr H. J., Kausch T., Scherer H., 2000, A&A, 357, 268

Giardino G., Banday A. J., Górski K. M., Bennett K., Jonas J. L., Tauber J., 2002, A&A, 387, 82

Gissinger C., Fromang S., Dormy E., 2009, MNRAS, 394, L84

Giz A. T., Shu F. H., 1993, ApJ, 404, 185

Gottlieb S., Shu C. W., 1998, Mathematics of Computation, 67, 73

Gressel O., Elstner D., Ziegler U., 2013, A&A, 560, A93

Guzmán A. E., May J., Alvarez H., Maeda K., 2011, A&A, 525, A138

Hanasz M., Lesch H., 2000, ApJ, 543, 235

Hanasz M., Lesch H., 2003, A&A, 412, 331

Hanasz M., Lesch H., Naab T., Gawryszczak A., Kowalik K., Wóltański D., 2013, ApJ, 777, L38

Hanasz M., Wóltański D., Kowalik K., 2009, ApJ, 706, L155

Haslam C. G. T., Salter C. J., Stoffel H., Wilson W. E., 1982, A&AS, 47, 1

Hillas A. M., 2006, ArXiv Astrophysics e-prints

Horiuchi T., Matsumoto R., Hanawa T., Shibata K., 1988, PASJ, 40, 147

Isobe H., Miyagoshi T., Shibata K., Yokoyama T., 2006, PASJ, 58, 423

Jubelgas M., Springel V., Enßlin T., Pfrommer C., 2008, A&A, 481, 33

Kamaya H., Horiuchi T., Matsumoto R., Hanawa T., Shibata K., Mineshige S., 1997, ApJ, 486, 307

Khajenabi F., 2012, Ap&SS, 337, 247

Kim J., Hong S. S., 1998, ApJ, 507, 254

Kim J., Hong S. S., Ryu D., 1997, ApJ, 485, 228

Kudoh Y., Hanawa T., 2016a, Journal of Physics Conference Series, 719, 012021

Kudoh Y., Hanawa T., 2016b, MNRAS, 462, 4517

Kulsrud R., 2005, Plasma Physics for Astrophysics, Plasma Physics for Astrophysics. Princeton University Press

Kuwabara T., Ko C.-M., 2015, ApJ, 798, 79

Kuwabara T., Nakamura K., Ko C. M., 2004, ApJ, 607, 828

La Porta L., Burigana C., Reich W., Reich P., 2008, A&A, 479, 641

Machida M., Nakamura K. E., Kudoh T., Akahori T., Sofue Y., Matsumoto R., 2013, ApJ, 764, 81

Matsumoto R., Hanawa T., Shibata K., Horiuchi T., 1990, ApJ, 356, 259

Nishikori H., Machida M., Matsumoto R., 2006, ApJ, 641, 862

Oppermann N. et al., 2012, A&A, 542, A93

Parker E. N., 1966, ApJ, 145, 811

Parker E. N., 1967, ApJ, 149, 535

Parker E. N., 1979, Cosmical magnetic fields: Their origin and their activity

Parrish I. J., Stone J. M., 2005, ApJ, 633, 334

Pfrommer C., Springel V., Enßlin T. A., Jubelgas M., 2006, MNRAS, 367, 113

Platania P., Burigana C., Maino D., Caserini E., Bersanelli M., Cappellini B., Mennella A., 2003, A&A, 410, 847

Rasera Y., Chandran B., 2008, ApJ, 685, 105

Remazeilles M., Dickinson C., Banday A. J., Bigot-Sazy M.-A., Ghosh T., 2015, MNRAS, 451, 4311

Rodrigues L. F. S., Sarson G. R., Shukurov A., Bushby P. J., Fletcher A., 2016, ApJ, 816, 2

Roe P. L., 1981, Journal of Computational Physics, 43, 357

Rudnick L., Brown S., 2009, AJ, 137, 145

Rudnick L., Owen F. N., 2014, ApJ, 785, 45

Rybicki G. B., Lightman A. P., 1985, Radiative processes in astrophysics.

Ryu D., Jones T. W., 1995, ApJ, 442, 228

Ryu D., Kang H., Hallman E., Jones T. W., 2003, ApJ, 593, 599

Salem M., Bryan G. L., 2014, MNRAS, 437, 3312

Santillán A., Kim J., Franco J., Martos M., Hong S. S., Ryu D., 2000, ApJ, 545, 353

Schlickeiser R., 2002, Cosmic Ray Astrophysics

Schlickeiser R., Lerche I., 1985, A&A, 151, 151

Shibata K., Tajima T., Matsumoto R., Horiuchi T., Hanawa T., Rosner R., Uchida Y., 1989, ApJ, 338, 471

Simard-Normandin M., Kronberg P. P., 1980, ApJ, 242, 74

Skilling J., 1975, MNRAS, 173, 245

Strong A. W., Moskalenko I. V., 1998, ApJ, 509, 212

Suresh A., Huynh H. T., 1997, Journal of Computational Physics, 136, 83

Takahashi K. et al., 2009, PASJ, 61, 957

Taylor A. R., Stil J. M., Sunstrum C., 2009, ApJ, 702, 1230

Testori J. C., Reich P., Reich W., 2008, A&A, 484, 733

Toro E., 2009, Riemann Solvers and Numerical Methods for Fluid Dynamics: A Practical Introduction. Springer Berlin Heidelberg

van Leer B., 1979, Journal of Computational Physics, 32, 101

Vazza F., Brüggen M., Gheller C., Brunetti G., 2012, MNRAS, 421, 3375

Vazza F., Ferrari C., Brüggen M., Bonafede A., Gheller C., Wang P., 2015, A&A, 580, A119

Vidal M., Dickinson C., Davies R. D., Leahy J. P., 2015, MNRAS, 452, 656

Webb G. M., Brio M., Zank G. P., Story T., 1995, ApJ, 442, 822

Wolleben M., Landecker T. L., Reich W., Wielebinski R., 2006, A&A, 448, 411

Yang H.-Y. K., Ruszkowski M., Ricker P. M., Zweibel E., Lee D., 2012, ApJ, 761, 185

Yokoyama T., Shibata K., 2001, ApJ, 549, 1160

Zank G. P., Webb G. M., Donohue D. J., 1993, ApJ, 406, 67

Zweibel E. G., 2013, Physics of Plasmas, 20, 055501